Alma Mater Studiorum – Università di Bologna
Facoltà di Scienze Matematiche Fisiche e Naturali

Dottorato di Ricerca in

Geofisica

Ciclo XXIII

Settore scientifico disciplinare: GEO/10

DETAILED STUDY OF THE SEISMOTECTONIC SETTING IN THE LUCANIAN APENNINES AND SURROUNDING AREAS (SOUTHERN ITALY)

Ph.D Thesis of: Cosmiana Maggi

Coordinator	**Tutor**
Prof. Michele Dragoni	Dr. Massimo Chiappini

year 2011

"Science is a wonderful thing if one
does not have to earn one's living at it"

(Albert Einstein)

Abstract

In this research work I analyzed the instrumental seismicity of Southern Italy in the area including the Lucanian Apennines and Bradano foredeep, making use of the most recent seismological database available so far. I examined the seismicity occurred during the period between 2001 and 2006, considering 514 events with magnitudes M ≥ 2.0. In the first part of the work, P- and S-wave arrival times, recorded by the Italian National Seismic Network (RSNC) operated by the Istituto Nazionale di Geofisica e Vulcanologia (INGV), were re-picked along with those of the SAPTEX temporary array (2001–2004). For some events located in the Upper Val d'Agri, I also used data from the Eni-Agip oil company seismic network. I computed the V_P/V_S ratio obtaining a value of 1.83 and I carried out an analysis for the one-dimensional (1D) velocity model that approximates the seismic structure of the study area. After this preliminary analysis, making use of the records obtained in the SeSCAL experiment, I incremented the database by handpicking new arrival times. My final dataset consists of 15,666 P- and 9228 S-arrival times associated to 1047 earthquakes with magnitude $M_L \geq 1.5$. I computed 162 fault-plane solutions and composite focal mechanisms for closely located events. I investigated stress field orientation inverting focal mechanism belonging to the Lucanian Apennine and the Pollino Range, both areas characterized by more concentrated background seismicity. Moreover, I applied the double difference technique (DD) to improve the earthquake locations. Considering these results and different datasets available in the literature, I carried out a detailed analysis of single sub-areas and of a swarm (November 2008) recorded by SeSCAL array. The relocated seismicity appears more concentrated within the upper crust and it is mostly clustered along the Lucanian Apennine chain. In particular, two well-defined clusters were located in the Potentino and in the Abriola-Pietrapertosa sector (central Lucanian region). Their hypocentral depths are slightly deeper than those observed beneath the chain. I suggest that these two seismic features are representative of the transition from the inner portion of the chain with NE-SW extension to the external margin

characterized by dextral strike-slip kinematics. In the easternmost part of the study area, below the Bradano foredeep and the Apulia foreland, the seismicity is generally deeper and more scattered and is associated to the Murge uplift and to the small structures present in the area. I also observed a small structure NE-SW oriented in the Abriola-Pietrapertosa area (activated with a swarm in November 2008) that could be considered to act as a barrier to the propagation of a potential rupture of an active NW-SE striking faults system. Focal mechanisms computed in this study are in large part normal and strike-slip solutions and their tensional axes (T-axes) have a generalized NE-SW orientation.

Thanks to denser coverage of seismic stations and the detailed analysis, this study is a further contribution to the comprehension of the seismogenesis and state of stress of the Southern Apennines region, giving important contributions to seismotectonic zoning and seismic hazard assessment.

Acknowledgments

First of all I would like to thank Prof. Rodolfo Console for having followed me in these years and for his invaluable advices. He is a person with an insatiable thirst for knowledge, which he imparts to his students.

I'm grateful to my tutor Dr. Massimo Chiappini for his availability and advices.

Special thanks are given to Dr. Giovanni Battista Cimini and Dr. Alberto Frepoli. They have installed the SeSCAL array and they have supported me with their knowledge and contributions in data analysis.

I would also like to thank Istituto Nazionale di Geofisica e Vulcanologia (INGV) and Centro di Geomorfologia Integrata per l'Area del Mediterraneo (CGIAM) which have financially supported the project of this work.

Finally, I wish to express my profound gratitude to my family and all my long friends who make my life unforgettable. Thank you for your advices and encouragement.

Table of contents

Introduction

Several studies on the seismicity of the Lucanian Apennines and surrounding areas have identified regions with different crustal domains, characterized by different spatial distribution, magnitude and mechanisms of local seismicity (Cucci et al., 2004; Chiarabba et al., 2005; Frepoli et al., 2005). Of particular importance is the result indicating an increase of hypocentral depth for the events below Bradanic Foredeep with respect to those located below the Apenninic chain. This deepening of the seismogenic layer in the SW-NE direction has also been reported in studies of seismic tomography and geothermal gradient, and it has significant implications on the brittle/ductile transition, tectonics and more generally, on the complex geodynamics of the lithosphere-asthenosphere system in the Southern Apennines (Scrocca et al., 2005).

The SeSCAL project was launched in the context described above and born from a scientific collaboration between the Istituto Nazionale di Geofisica e Vulcanologia (INGV) in Rome and the Centro di Geomorfologia Integrata per l'Area del Mediterraneo (CGIAM) in Potenza. The principal aim of this project was to increase the knowledge about the complex crustal structure beneath the area of the southern range of Basilicata, Campania and Puglia, through the exploitation of multidisciplinary studies based on the acquisition and interpretation of seismic data and potential fields.

The work carried out in the present research thesis deals with the analysis and interpretation of seismological data recorded by a temporary array implemented during this project described in Chapter 3.

The manuscript includes an introductory part where the geodynamic and tectonic settings are described in order to give an overview of the complexity of the analyzed area (Chapter 1), along with the main methodologies (Chapter 2) and the observational data used in this study (Chapter 3). The data processing has been divided into four main steps: the computation of the V_P/V_S ratio and a reference *P*-wave one dimensional (1D) velocity model close to the true Earth model together with station corrections important to obtain accurate locations (Chapter 4); I made a seismotectonic analysis using classical approaches (Chapter 5); the

application of a recent methodology called double difference technique (DD) to further improve the earthquake locations and to carry out a detailed analysis of single groups of events using the composite focal mechanisms technique (Chapter 6). Finally, a detailed study of a significant swarm recorded in the Abriola-Pietrapertosa area during November 2008 applying the waveform cross-correlation technique has been described(Chapter 7).

Chapter 1

Geodynamics and Seismotectonics of Southern Italy

The Southern Apennines belong to the complex geodynamic setting characterizing the Central Mediterranean region, which is dominated by the NNW–SSE convergence between the European and African plates. This mountain chain was hit by several destructive historical earthquakes and is characterized by a background seismicity (scattered events and earthquakes with $M_L \leq 3$) concentrated along the belt.

In this chapter I shortly describe the geodynamics, the tectonic evolution, the historical and the instrumental seismicity of the Lucanian Apennines and surrounding areas to understand the complexity and the importance to improve our knowledge of this zone. This general setting is important for the comprehension of difficulties met and results gained by this study.

1.1 Geodynamic and tectonic evolution

The axial zone of the Southern Apenninic belt constitutes the backbone of the southern part of the Italian peninsula. Since the Early Pleistocene (Fig.1.1), active extension produced a broad and complex system of normal faults within the Apenninic chain. The area was previously affected by compression (Middle-Late Miocene) and characterized by an eastward migration of the Apenninic compressional front (Patacca et al., 1990; Hippolyte et al., 1994; Doglioni et al., 1996). The eastward migration of the extension–compression system of the Apenninic belt is related with the subduction process of old oceanic lithosphere beneath the Southern Apennines and Calabrian Arc and with the Tortonian opening and oceanisation of the Tyrrhenian basin (Patacca et al., 1990; Doglioni et al., 1996; Barberi et al., 2004). The Apenninic orogen is bordered to the east and northeast by the thick continental Apulian

platform which is clearly distinct, from a tectonic point of view, from the remaining of the peninsula. It represents an emerged portion of the relatively more rigid structure named Adriatic microplate, a promontory of Africa towards Eurasia, which is extending beneath the Adriatic Sea (Channell et al., 1979; Anderson and Jackson, 1987).

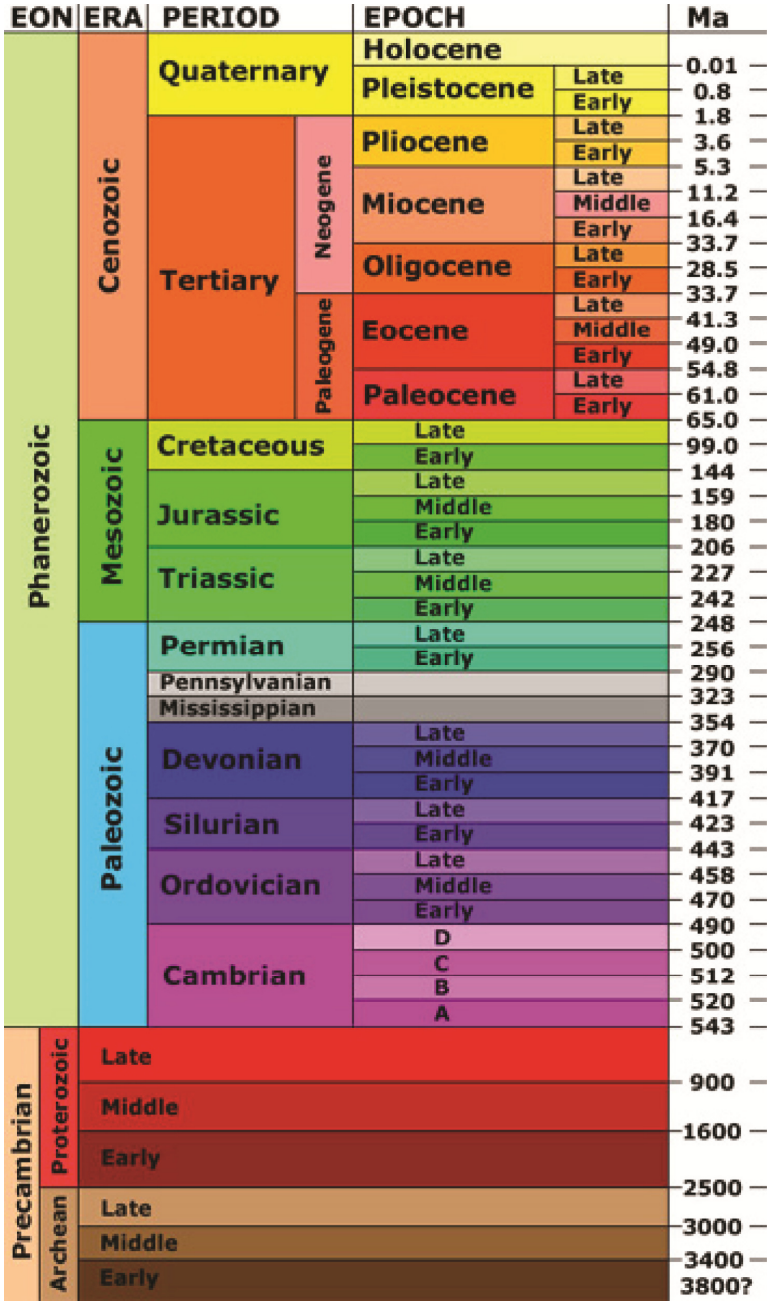

Figure 1.1: Geological time scale; millions of years (Ma) (from Stoffer, 2006).

The Adriatic microplate is bordered by an almost continuous belt of orogenic chains (Apennines, Alps, Dinarides, Hellenides) and plays the role of foreland for the more deformable bordering regions. In fact, these areas are affected by a diffuse seismic activity correlated to a general counter-clockwise motion of the microplate itself (Meletti et al., 2000). The east-southeastward migration of the Tyrrhenian-Apennine subduction system (Malinverno and Ryan, 1986; Royden et al., 1987; Gueguen et al., 1998; Rosenbaum and Lister, 2004), followed by the asthenospheric wedging at the retreating subduction hinge beneath the Southern Apennines and the southern Tyrrhenian Sea (Doglioni et al., 1996), appears to have slowed and buckled during the Late Pleistocene after the collision with the thick continental lithosphere of the Apulia foreland at the front of the belt (Doglioni et al., 1994). Three different types of extensional environments may be observed in a section E-W of the subduction system (see Fig. 1.2):

- Type 1: the extension generated by horizontal stretching during back-arc opening with the basal decollement at stretched lithosphere-asthenosphere boundary.
- Type 2: the extension coeval with the uplift that may be interpreted as due to the bending of the subducted lithosphere and to the upward push generated by the asthenospheric wedging at the subduction hinge.
- Type 3: the Apulia foreland extension generated by bending of the subducting lithosphere. It has normal faults terminating in the neutral crustal zone of folding where flexural slip may form (Doglioni, 1996).

Deep structures beneath the Southern Apennines can be generally explained with a thick-skinned tectonic model (Menardi Noguera and Rea, 2000). These Plio-Pleistocene contractional structures, related to a basement-involved thrust tectonics (Apulian Platform deformation), are evident from structural profiles. A further evidence of this basement-involved thrust tectonics is given by the Monte Alpi structure which actually represents remnants of a mélange zone originally interposed between the Apulian Platform carbonates and the overlying far-travelled detachment sheet (Corrado et al., 2002). The complex geodynamic setting of this area is dominated by the NNW–SSE convergence between the African and the Eurasian plates, which are currently converging at a rate of 10 mm/year (Argus et al., 1989; De Mets et al., 1990). Geodetic observations, together with seismological studies, reveal that the Apenninic chain is undergoing a NE-trending extension, with seismic

deformation rates higher in the southern portion (Di Luccio et al., 2005; D'Agostino et al., 2008).

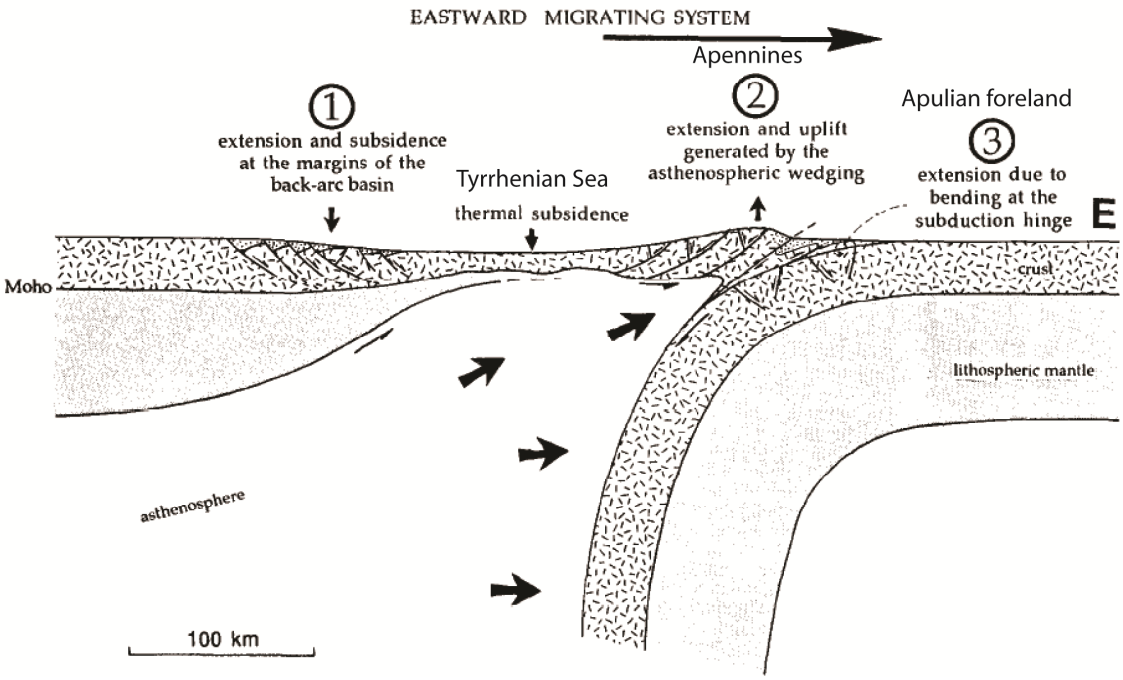

Figure 1.2: Representation of subduction system in Southern Italy (W-E section) and of the three different types of extensional environments (modified from Doglioni, 1996).

1.2 Historical and instrumental seismicity

Southern Apennines is one of the main seismically active regions of Italy (Fig. 1.3).The historical seismic catalogue shows a completeness for the Italian highly energetic events occurred in the last four centuries (CPTI Working Group, 2004). Among the strongest earthquakes of the southern Apenninic belt, the 1694 Irpinia (Me = 6.9; Serva, 1985) and the 1857 Basilicata events (Me = 6.9; Branno et al., 1983; Branno et al., 1985) recorded both an epicentral intensity of XI degree on the Mercalli-Cancani-Sieberg (MCS) scale.

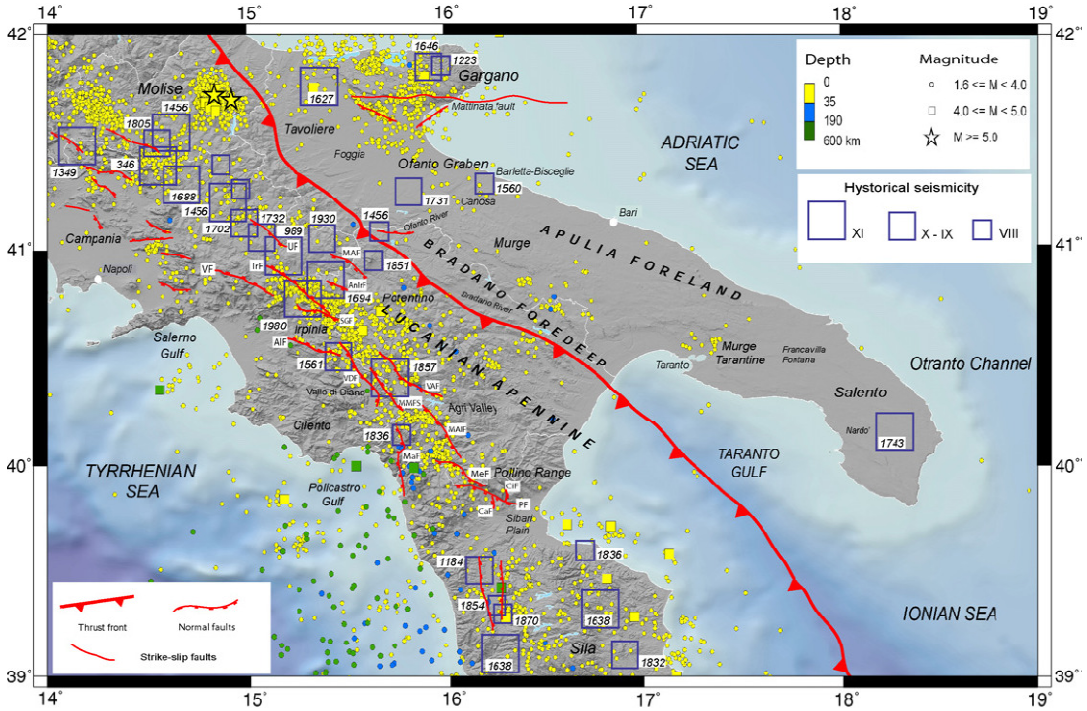

Figure 1.3: Map of historical and instrumental seismicity in Southern Italy (CPTI Working Group, 2004; Seismicity map of Italy, 2000–2007, INGV-CNT, Roma, Castello et al., 2008). Active faults from Galadini et al. (2000), Maschio et al. (2005) and Papanikolaou and Roberts (2007). Lucanian Apennine active faults: UF, Ufita fault; MAF, Mount Mattinata–Atella fault; VF, Volturara fault; IrF, Irpinia fault; AnIrF, Antithetic Irpinia fault; SGF, San Gregorio fault; ALF, Alburni fault; VDF, Vallo di Diano fault; VAF, Val d'Agri fault; MMFS, Monti della Maddalena fault system; MALF, Monte Alpi fault; MAF, Maratea fault; MeF, Mercure fault; PF, Pollino fault; CaF, Castrovillari fault; CiF, Civita fault (from Frepoli et al., 2011).

The September 8, 1694 earthquake affected a wide area between Campania and Basilicata, producing serious damage in 120 municipalities distributed among the Irpinia and Salerno district and the Basilicata (6,000 people died). The seismic sequence was characterized by a mainshock, followed immediately after by a second quake and then by a suite of strong aftershocks, which lasted until the first days of January 1695. The macroseismic surface faulting of this shock is of 38 km length (Serva et al., 1997) and is approximately superimposed on the macroseismical area of maximum intensity of the 1980 Irpinia event (Fracassi and Valensise, 2007). Moreover, it did not cause slip on the fault responsible of the 1980 earthquakes but it was located in the proximity of the antithetic fault (not observed on the surface) of the 1980 Irpinia event.

The November 23, 1980 Irpinia mainshock had a X MCS macroseismic intensity (Ms = 6.9). It is the largest earthquake that occur in Italy in the last 90 years, and it provides the first well-documented example of surface faulting related with certainty to the coseismic displacement (Pantosti and Valensise, 1990). Westaway (1993) suggested the following fault ruptures sequence (see Fig.1.4):

1. The initial fault rupture nucleated at or near the SE end of the Carpineta fault and propagated to the NW.
2. Rupture continued apparently without interruption onto the adjoining Marzano fault.
3. Rupture then paused for ~0.5 s, before continuing to the NW along the Picentini fault.
4. ~14 s after the mainshock, this sequence started a SE-propagating rupture on the San Gregorio fault. Each of these ruptures was associated with surface faulting and intense aftershock activity.
5. The existence of another aftershock cluster NW of the Picentini scarp suggest a fifth fault rupture at Castelfranci. Faulting at this locality began ~12 s after the initial rupture.
6. ~20 s after the mainshock a subevent started on the surface dipping NE at ~20°, at the base of the brittle upper crust beneath the steep antithetic fault (see Fig.1.5).
7. ~40 s after the initial rupture an additional rupture started on a fault with different orientation. This subevent involved a steep normal fault that dips at ~70° and reaches the surface at ~11km to the NE of the Marzano fault (antithetic fault).

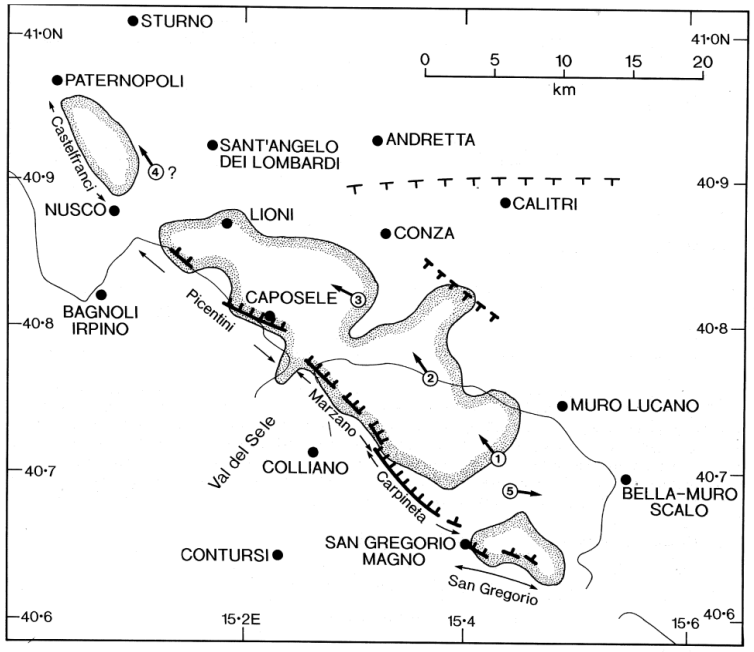

Figure 1.4: Summary map of the epicentral area of the Irpinia 1980 event. Numbered arrows indicate the nucleation points and rupture directions for the four or five subevents that ruptured the steep NE-dipping faults (from Westaway, 1993).

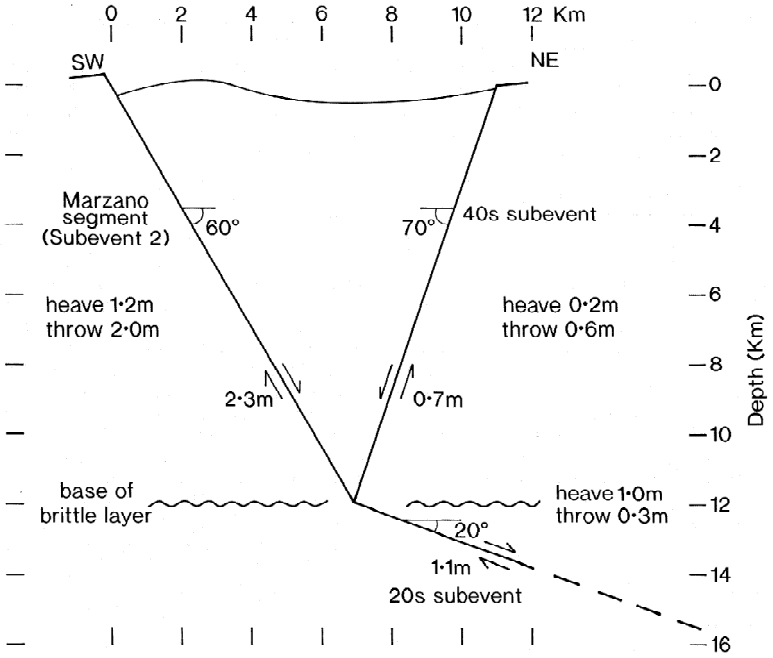

Figure 1.5: Schematic cross-section across the Marzano fault and the associated antithetic fault at 11 km NE obtained by Westaway, 1993 for the 1980 Irpinia earthquakes.

The Potentino area (Basilicata) was hit by the two seismic sequences occurred 10–11 years (1990–1991) after the devastating 1980 Irpinia event. They were approximately located 40 km SE of the 1980 earthquake. The May 05, 1990 mainshock (Mw=5.7) (Ekstrom, 1994) damaged the town of Potenza and surrounding villages (Io=VII MCS). On May 26, 1991 another earthquake (Mw=5.2) struck the same area causing additional damage. The depth of the 1990–1991 seismicity is concentrated mostly between 15 and 23 km. Both mainshocks of these sequences are characterized by a right-lateral strike slip tectonics considering the E-W nodal plain of the two fault plain solutions. This tectonics is similar, in hypocentral depth and mechanical behaviour, to that of Molise 2002 and it is unusual with respect to those characterizing the overall seismicity of Southern Apennines within the chain (Di Luccio et al., 2005). This depth range corresponds to the upper part of the middle crust underlying the Apulian sedimentary cover, within the footwall of the easternmost Apennine thrust system. Moreover, these seismic sequences can be interpreted to be produced by a crustal E–W fault zone within the Apulian crust (Boncio et al., 2007).

It is noteworthy to mention the 1561 complex seismic sequence located to the north of the Vallo di Diano, which is reappraised by Castelli et al. 2008. This sequence was characterized by two large earthquakes occurred within 20 days (31 July and 19 August) with maximum intensities of X MCS (M_e= 6.4).

One of the strongest historical earthquake of the Italian seismic history is the December 16, 1857 (M_W 7.0) earthquake killing over 11,000 people. It struck a large portion of the Southern Apennines about 150 km to the SE of Naples. This earthquake caused extensive damage over an exceptionally large area with intensity of X and larger (MSC scale). Most of damages were suffered in the Upper Val d'Agri. This event was thoroughly investigated by the Irish engineer Robert Mallet, who wrote an extensive report that is still regarded as a landmark in observational seismology. For the 1857 earthquake there is no evidence of surface faulting as for the 1980 Irpinia earthquake.

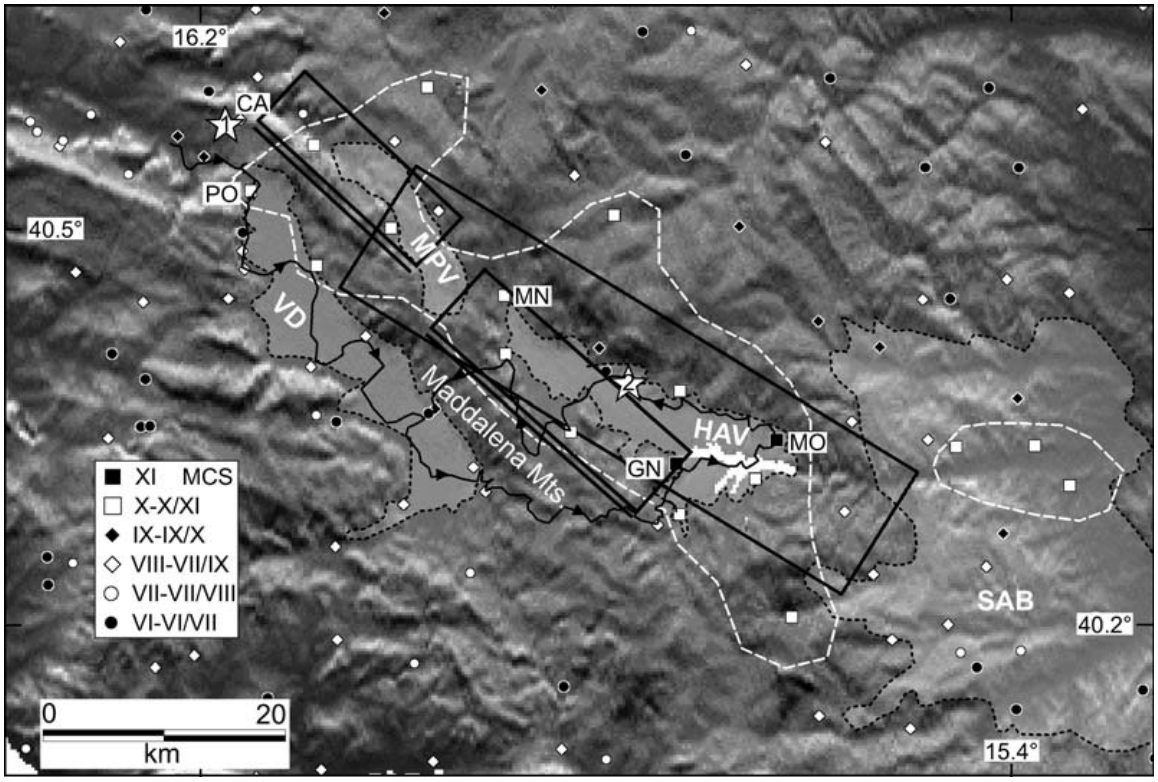

Figure 1.6: Map of intensities available for the December 16, 1857 earthquake (MCS scale) (Boschi et al., 2000), plotted over the Melandro–Pergola valley (MPV) (to the NW) and the Upper Val d'Agri (HAV). Seismogenic sources are from the DISS database (DISS Working Group, 2009). White dashed line contours are intensities X and higher. Black rectangles are the macroseismic sources derived from the analysis of the intensity data distribution (Gasperini et al., 1999). The stars numbered 1 and 2 show the epicenters proposed by Mallet and obtained by automatic analysis (Gasperini et al., 1999; Boschi et al., 2000), respectively. Sant'Arcangelo basin (SAB); Vallo di Diano (VD). Caggiano (CA); Grumento Nova (GN); Marsico Nuovo (MN); Montemurro (MO); Polla (PO) (from Burrato &Valensise, 2008).

Numerous studies concerning this area suggest that the earthquake was caused by normal fault NW-SE oriented with a rupture length of ~50 km (Burrato and Valensise, 2007). A recent study of Burrato and Valensise, (2008) contends that this earthquake involved two adjacent and relatively well known faults. This finding may indeed have significant implications for the local seismic hazard (Fig. 1.6):

1. The smaller Melandro-Pergola valley faults (MPV) where there was a shock of magnitude 6.0 or greater 2-3 minutes before the mainshock. This area was commonly believed as a seismic gap between the 1857 fault and the 1980 Irpinia earthquakes.
2. The larger Upper Val d'Agri fault (HAV) where was located the stronger shock.

If the MPV and HAV faults both ruptured in 1857, the MPV fault should no longer be considered a seismic gap, suggesting that a ~100 km long section of the Apennines seismogenic backbone has ruptured entirely over the past 150 years.

Moving further to the south along the Apenninic chain, we find a complex region characterized by two important borders:

1. One on the surface: the boundary between the Apenninic Chain and the Calabrian Arc.
2. And one in depth: the border between the Adriatic and the African plates.

This area was hit by the September 9, 1998 Mercure earthquake (M_W=5.6) and the associated aftershocks (lasted about 14 months) that caused some damage in several towns and villages located within a mesoseismal area attaining a maximum intensity of VII MCS (Guerra et al., 2005). A singularity of this event was that no seismic activity was observed in the surrounding area in the two previous months before the mainshock. The mainshock occurred at the NW edge of the seismic sequence at a depth of 10.5 ± 1.5 km. Its peculiarity consisted in a sudden change of the seismic activity from a series of normal NW-SE faults and to strike slip faults with NE-SW and E-W trend. This complex behaviour and the different orientations suggest that the area acts as a hinge between the NW-SE trending Southern Apennines and the locally N-S trending Calabrian Arc (Guerra et al., 2005). Brozzetti et al. (2009) identified the structure responsible of the 1998 earthquake (CSPT fault in Figure 1.7). Based on field data, they have defined for this fault a maximum extent of 18 km, and using the hypocentral information of the Mercure sequence, they have reconstructed the depth geometry. The CSPT fault is characterized by an along-strike length about 19 km and a down-dip width of about 12 km respectively. It fits well with the mainshock and the aftershocks hypocentral locations and with the distribution of the damages (see Fig. 1.7). The CSPT plane dips SSW-ward with an average dip of 60°. Considering this reconstruction, they have evaluated that the 1998 mainshock would have only activated a small portion of such a plane (~55 km^2) presupposing that the entire plane might have undergone with a seismogenic rupture in the course of a single event. In such a case a magnitude 6.3 would be attended. In conclusion, this setting suggests that the Mercure area must be considered comparable, in terms of seismic hazard, to the neighbouring Pollino-Castrovillari areas where there is knowledge of strong paleoseismological events associated with the Castrovillari fault (Cinti at al., 1997).

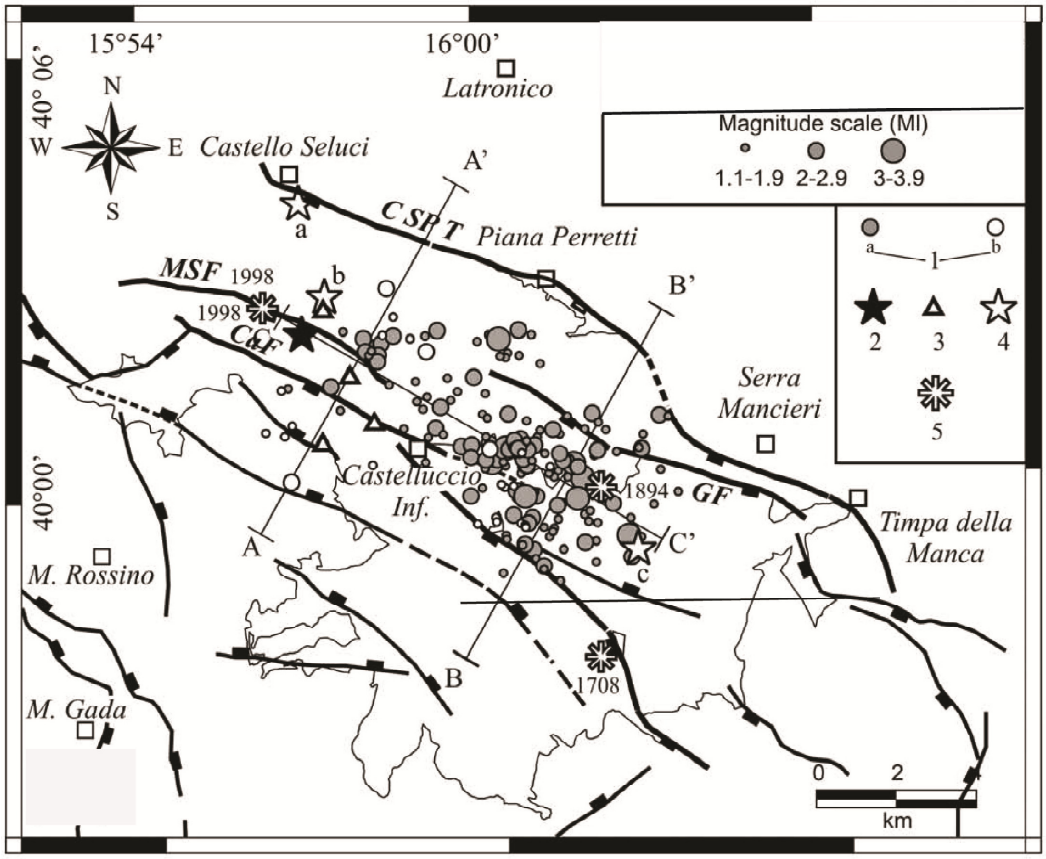

Figure 1.7: Map of the faults refers to the CSPT fault, the Madonna del Soccorso F. (MSF), the Gallizzi F. (GF), and The Castelluccio F. (CaF). Moreover, the 1998 Mercure sequence epicentral distribution relocated by Brozzetti et al., 2009: 1= epicentres; 2= epicenter of the Mercure main event (Mw 5.6) ; 3= foreshocks. 4=Mercure 1998 instrumental epicenter in the other literature (a=CSI epicenter in Castello et al., 2006; b=Euro-Med bulletin epicenter; c= epicenter relocated by Guerra et al., 2005); 5=macroseismic epicenters of major historical events occurred in the Mercure area: the 1998 and 1894 epicenters are from the CPTI04 catalogue. Figure modified from Brozzetti et al., 2009.

The northern part of Apulia (Gargano, Tavoliere and Ofanto Graben) is a remarkably seismogenic area (Piccardi, 2005; Tondi et al., 2005; Del Gaudio et al., 2005, 2007). Highly energetic events are historically documented as the 1627 earthquakes (M_e = 6.8; X degree MCS) that hit the northern Foggia province (Molin and Margottini, 1985). In the Ofanto Graben, the quite well-documented 1560 earthquake (M_e=5.7) which hit the Barletta and Bisceglie towns (macroseismic intensity differently estimated between VII-VIII and IX MCS, according to different catalogues), has been often considered an over-estimated event because of site amplification (Del Gaudio et al., 2005). On March 20, 1731, an earthquake (M_e=5.2),

with macroseismic intensity estimated between IX and X MCS, hit the southern part of the Foggia province, followed by several strong aftershocks (Molin, 1985). Another important seismic sequence, occurred on August 14, 1851. It had its focus in the area of the extinct Vulture volcanic apparatus, located directly to the East of the front of the Apenninic chain front. The mainshock (M_e = 6.3; X MCS) was followed by numerous aftershocks, some of which appear to have felt more strongly in Apulia at Canosa (Magri and Molin, 1979; Del Gaudio et al., 2005). The Bradano foredeep and Apulia foreland areas, both to the South of the Ofanto river, do not show considerable historical seismicity, with the exception of the 1743 Salento earthquakes (M_e=7.1) whose epicentral area was probably located offshore within the Otranto Channel (Margottini, 1981; Mastronuzzi et al., 2007). This event induced high amplification mainly in the villages of Nardò and Francavilla Fontana (IX-X MCS) founded on thin Pleistocene basins filled with soft sediments (Galli and Naso, 2008). It is also interesting to note the seismic activity characterized by sequences of moderate magnitude (strongest event with M_L=5.1) occurred in the years 1974, 1977 and 1991 in the offshore foreland region southeast of the Salento peninsula (D'Ingeo et al., 1980; Favali et al., 1990; Argnani et al., 2001).

Chapter 2

Description of methodologies used

Our knowledge of the velocity structure of the Earth and of the seismic hypocenters is the result of interpreting seismograms. One of the most important tasks in observational seismology is locating seismic sources. This involves determining both the hypocentral coordinates and the source origin time. Generally, determining the source location requires identification of seismic phases and measuring their arrival times, as well as knowing the velocity structure between the hypocenter and the seismic station. Given the location of a seismic source, one can be compute the travel-time for any particular phase to a seismic station anywhere in an arbitrarily complex velocity model (Lay and Wallace, 1995).

This chapter describes synthetically the methodologies used in our analysis to compute V_S/V_P (necessary to calculate the V_S velocity model by an initial computed V_P model) and to locate earthquakes.

2.1 Wadati modified method

This method is used to compute an average V_S/V_P ratio for the studied area. The modified Wadati method (Chatelain, 1978) is shortly described below. The V_S/V_P ratio is useful for improving the accuracy of hypocentral depths in the location algorithm.

If we consider an event k that is recorded by two stations (i, j) at hypocentral distances x_i and x_j, the time difference between phases $P_i - P_j$ and $S_i - S_j$ can be expressed as:

$$P_i - P_j = \frac{(x_i - x_j)}{V_P} \qquad (2.1)$$

and

$$S_i - S_j = \frac{(x_i - x_j)}{V_S} \qquad (2.2)$$

where V_P and V_S are the P- and S-wave velocity values, respectively.

Dividing (2.2) by (2.1) we obtain:

$$\frac{DT_S}{DT_P} = \frac{S_i - S_j}{P_i - P_j} = \frac{V_P}{V_S} \qquad (2.3)$$

Fitting DT_S versus DT_P for all available pairs of stations gives the value of the slope V_P/V_S.

2.2 Earthquake location

Location of earthquakes is one of the most important tasks in observational seismology. Generally, a 1D velocity model, of plain and parallel layers with a constant velocity in each layer, is used to simplify the calculations for regional distance ($\Delta \leq 1400km$).

If we know the location of a seismic source, we can compute the travel-time for any particular phase at a seismic station anywhere considering an arbitrary complex velocity model. This is known as a *forward problem*: arrival times are computed based on parameterized model. Moreover, an *inverse problem* consists in finding the earthquake location, where we know the observation data (arrival times) but the problem must be solved for a source location and origin time that are consistent with the data (Lay and Wallace, 1995).

2.2.1 Single event location

When we find a forward problem that closely approximates the observations, we declare that the model sufficiently describes the earthquake location for given model assumptions. We regard an earthquake with hypocentral location $\mathbf{x} = (x, y, z)$ and origin time t unknown. If we have i stations located in the point (x_i, y_i, z_i), at which we have actually measured arrival time $d_i^{'}$, we can write:

$$d_i^{'} = t + T(\mathbf{x}, \mathbf{x}_i) \qquad (2.4)$$

where $T(x, x_i)$ is the travel-time equation.

If we know the velocity structure we can solve the direct problem:

$$\mathbf{d} = \mathbf{A}(\mathbf{m}) \text{ or } d_i = A(m_j) \qquad (2.5)$$

j=1,…,4 indicate the hypocentral parameters and $\mathbf{m} = (x, y, z, t)$ is the model vector with the hypocentral coordinates and the origin time t.

Generally, to solve an inverse problem (earthquake location), we guess a solution for the model $m^0 = (x_0, y_0, z_0, t_0)$ for which the predicted times, $d^0 = A(m^0)$, can be calculated and investigate the behaviour of d^0 in the neighbourhood of m^0. We approximate changes in m^0 with a Taylor series approximation:

$$m_j = m_j^0 + \delta m_j \qquad (2.6)$$

where δm_j^0 is an incremental variation of the jth model parameter that moves the model toward a better fit to the data. The corresponding change in the predicted data vector can be found by expanding of (2.5) in a Taylor series about $m^0 + \delta m^0$:

$$d_i \approx d_i^0 + \sum_j \left.\frac{\partial d_i}{\partial m_j}\right|_{m^0} \delta m_j^0 \qquad (2.7)$$

then

$$\Delta d_i^0 = d_i - d_i^0 = \sum_j \left.\frac{\partial d_i}{\partial m_j}\right|_{m^0} \delta m_j^0 \qquad (2.8)$$

Equation (2.8) shows that the difference in the observed and predicted travel times (right-hand) is now linearly related to changes in the model parameters. We look for changes in the hypocentral coordinates to make the model better predict the data. Using only the first term of a truncated Taylor series provides the linearization, but this also precludes the perturbations from immediately converging to the true **m**. We can write la (2.8) in vector form:

$$\Delta\mathbf{d} = \mathbf{G}\Delta\mathbf{m} \qquad (2.9)$$

where $G_{ij} = \dfrac{\partial d_i}{\partial m_j}$.

If there are four observed arrival times, we have four equations and can solve the system by Gaussian elimination, giving either no solution or an exact result for δm_j^i.

Any errors in the data will lead to an incorrect solution, or inconsistent equations.

The matrix **G** will result square, then we can calculate the inverse matrix $\mathbf{G}^{-1}$, multiplying both sides of the (2.9) for this matrix and by definition $\mathbf{G}^{-1}\mathbf{G} = \mathbf{I}$ we obtain:

$$\mathbf{G}^{-1}\Delta\mathbf{d} = \mathbf{G}^{-1}\mathbf{G}\Delta\mathbf{m} \text{ from which } \Delta\mathbf{m} = \mathbf{G}^{-1}\Delta\mathbf{d} \qquad (2.10)$$

Once $\Delta\mathbf{m} = (\delta x, \delta y, \delta z, \delta t)$ are calculated, we can "correct" the source parameter guesses:

$$x_1 = x_0 + \delta x_{0,}\ , y_1 = y_0 + \delta y_{0,}\ ,\ z_1 = z_0 + \delta z_{0,} \text{ and } t_1 = t_0 + \delta t_{0,} \qquad (2.11)$$

This new values are now used to repeat the entire process. This interactive process is continued until $\Delta\mathbf{d}$ becomes acceptably small (Geiger's method). Eq. (2.10) assumes that we can perfectly predict the data. In case of travel-times, this means that we must know the velocity structure between hypocenter and station extremely well. Unfortunately, the rate at which it converges depends strongly on the accuracy of the starting model. Further, this process does not guarantee convergence.

In general, most hypocenter location problems are *overdetermined* (there are more observations than the four source parameters) and the solution is the best model fit to an "average" of the data. Together there is no unique solution of the system that identically satisfies all the equations. This is related to the inevitable experimental errors in the arrival times readings and even with the imperfections that regulate the laws of travel times. The velocity model simplifies a complex reality, there is no exact model that perfectly describes the data. The best fit is usually defined as the model with the smallest residual, or difference between observed and predicted data.

Considering the Eq. (2.9), we can write an equation that describes the misfit of the model:

$$\mathbf{E} = \left[\mathbf{d} - \mathbf{G}\mathbf{m}\right] \qquad (2.12)$$

The inverse problem is designed to find a model that minimizes **E** using the *minimum square error method*:

$$E^2 = \sum_{i=1}^{n}\left(d_i - \sum_{j}^{m} G_{ij} m_j\right)^2 \qquad (2.13)$$

and force E^2 to be a minimum computing the derivative of the Eq. (2.13) with respect to the model parameters:

$$\frac{\partial E^2}{\partial m_k} = 2E\ \frac{\partial E}{\partial m_k} = -2\sum_{i=1}^{n}\left(d_i - \sum_{j=1}^{m} G_{ij} m_j\right) G_{ik} = 0 \qquad (2.14)$$

if we rewrite this equation in matrix form, we obtain:

$$\mathbf{G}^T\Delta\mathbf{d} = \mathbf{G}^T\mathbf{G}\Delta\mathbf{m} \qquad (2.15)$$

We observe that $\mathbf{G}^T\mathbf{G}$ is a square matrix that we can invert even if we have an overdetermined problem.

The solution of the inverse problem will be:

$$\Delta\mathbf{m} = (\mathbf{G}^T\mathbf{G})^{-1}\mathbf{G}^T\Delta\mathbf{d} = \mathbf{G}^{-g}\Delta\mathbf{d} \qquad (2.16)$$

where $\mathbf{G}^{-g} = (\mathbf{G}^T\mathbf{G})^{-1}\mathbf{G}^T$ is the *generalized inverse matrix*.

Moreover, we solve $\mathbf{G}^T\mathbf{G}$ in terms of eigenvector matrices *V*:

$$\mathbf{G}^T\mathbf{G} = \mathbf{V}\Lambda\mathbf{V}^T \qquad (2.17)$$

The matrix $\mathbf{V}$ contains the eigenvectors of $\mathbf{G}^T\mathbf{G}$ and Λ is a diagonal matrix with eigenvalues along the principal diagonal and all other values equal to zero.

If we suppose that the eigenvectors are orthonormal that is:

$$\mathbf{V}\mathbf{V}^T = \mathbf{V}^T\mathbf{V} = \mathbf{I} \text{ and } \mathbf{V}^T = \mathbf{V}^{-1} \qquad (2.18)$$

we obtain

$$(\mathbf{G}^T\mathbf{G})^{-1} = (\mathbf{V}\Lambda\mathbf{V}^T)^{-1} = \mathbf{V}\Lambda^{-1}\mathbf{V}^T \qquad (2.19)$$

$\mathbf{G}\mathbf{G}^T$ can be written:

$$\mathbf{G}\mathbf{G}^T = \mathbf{U}\Lambda\mathbf{U}^T \qquad (2.20)$$

where $\mathbf{U}$ is the eigenvector matrix of $\mathbf{G}\mathbf{G}^T$.

By (2.17) and (2.20) the eigenvector matrix with eigenvalues different from zero $\mathbf{V}_P$ and $\mathbf{U}_p$ is obtained using the Lanczos decomposition:

$$\mathbf{G} = \mathbf{U}\Lambda\mathbf{V}^T = \mathbf{U}_p\Lambda\mathbf{V}_{\mathrm{p}}^{\mathrm{T}} \qquad (2.21)$$

$$\mathbf{G}_p^{-1} = \mathbf{V}_p\Lambda_p^{-1}\mathbf{U}_p^T \qquad (2.22)$$

$$\mathbf{m}_p = \mathbf{G}_p^{-1}\mathbf{d} \text{ (}\textit{singular value decomposition}\text{ SVD)} \qquad (2.23)$$

the (2.22) is important because allows to solve the inverse problem also when $\mathbf{G}$ is a singular matrix. We can write the model derived from (2.22 and 2.23)

$$\mathbf{m}_p = \mathbf{G}_p^{-1}\mathbf{G}\mathbf{m} = \mathbf{V}_p\Lambda_p^{-1}\mathbf{U}_p^T\mathbf{U}_p\Lambda_p\mathbf{V}_p^T\mathbf{m} = \mathbf{V}_p\mathbf{V}_p^T\mathbf{m} \qquad (2.24)$$

The resolution matrix $\mathbf{R} = \mathbf{V}_p\mathbf{V}_p^T$ indicates how much the true model is smeared into the various parameters of inversion model. Calculation of this matrix is important for assessing an inversion result.

We make another definition: the *covariance matrix*:

$$c = \mathbf{V}_p \mathbf{\Lambda}_p^{-2} \mathbf{V}_p^T \qquad (2.25)$$

where the element of $\mathbf{\Lambda}_p^{-2}$ are $\left(1/\lambda_1^2, 1/\lambda_2^2, ..., 1/\lambda_p^2\right)$. We observe that small singular values cause a greater variance in the solution. Thus small eigenvalues lower the stability of the inverse and the resolution decreases.

Finally, the arrival time data used to locate earthquakes have errors that produce uncertainties in the resulting locations. It is usually assumed that the errors associated with the data at the *i*th station, d_i are random values with a *Gaussian distribution* with mean $\bar{d}_i$ and standard deviation σ_i. For a large number of measurements from this distribution, the mean is the average:

$$\bar{d}_i = \lim_{K\to\infty} \frac{1}{K} \sum_{K=1}^{K} d_i^{(k)} \qquad (2.26)$$

and the "spread" of the measurements is given by the variance:

$$\sigma_d{}^2 = \lim_{K\to\infty} \left(\frac{1}{K} \sum_{K=1}^{K} \left(d_i^{(k)} - \bar{d}_i\right)\left(d_j^{(k)} - \bar{d}_j\right) \right) \qquad (2.27)$$

therefore, a given data point d_i has a 95% probability of falling within $\pm 2\sigma_i$ of the true value.

The covariance of the model parameters in terms of those for the data are:

$$\sigma_m{}^2 = \lim_{K\to\infty} \frac{1}{K} \sum_{K=1}^{K} \left(m_j^{(k)} - \bar{m}_j\right)\left(m_i^{(k)} - \bar{m}_i\right) \qquad (2.28)$$

We often assume that the data errors are uncorrelated and equal, so that the data variance-matrix is a constant times identity matrix (Stein and Wysession, 2003). By means of equations (2.23) and (2.27) we can write:

$$\sigma_m^2 = \mathbf{G}^{-1} \boldsymbol{\sigma}_d^2 \left(\mathbf{G}^{-1}\right)^T \qquad (2.29)$$

2.2.2 Joint-Hypocenter-Determination (JHD)

The hypocenter determination requires the use of an Earth model that approximates the seismic structure of the study area. So, errors are introduced into the earthquake location process. In general we divide the errors into three groups:

1) Deviations from the velocity structure near the source;

2) Deviations near the station;
3) Deviations along the deep travel path.

For a single event-station pair it is not possible to isolate the effects of these errors. However, if a group of earthquakes with approximately the same location (*cluster*) occur, we can determine something about the errors in the used model. Exactly, we can compute a "station correction" that accounts for the inaccuracies of the model structure along the travel path and beneath the station. In this case we can recast the problem determining *n* station corrections and *m* hypocenter locations. We can rewrite equation (2.7) with:

$$r_{ij} = dT_j + \frac{\partial t}{\partial x} dx_j + \frac{\partial t}{\partial y} dy_j + \frac{\partial t}{\partial z} dz_j + \frac{\partial t}{\partial s} ds_{i,} \qquad (2.30)$$

where r_{ij} is the residual or error, at the *i*th station for the *j*th earthquake. Moreover, $r_{ij} = \hat{t}_{ij} - t_{ij}$, where $\hat{t}_{ij}$ is the observed arrival time and t_{ij} is the computed travel time and station correction. dT_j is the perturbation of the origin time for the *j*th event. In matrix form:

$$\mathbf{r}_j = A_j d\mathbf{x}_j + S_j d\mathbf{s} \qquad (2.31)$$

where $\mathbf{r}_j$ is the data change vector, S_j are station corrections that contain the travel–times bias as well as the station effect, and $d\mathbf{x}$ and $d\mathbf{s}$ are separate model change vectors. The solution of this system of equations is known as *joint hypocentral determination* (JHD) and was first proposed by Douglas (1967). The relative locations obtained by JHD are better than those computed by inversion of more complete and complex velocity models (Lay and Wallace, 1995).

2.2.3 Double-Difference method

The double-difference (DD) algorithm minimizes errors due to unmodelled velocity structure without the use of station corrections (Waldhauser and Ellsworth, 2000). The effects of errors in structure can also be effectively minimized by using relative earthquake location methods. If the hypocentral separation between two earthquakes is small compared to the event-station distance and to the scale length of the velocity heterogeneity, then the ray paths between the source region and a common station are similar along almost the entire ray path. In this case, the difference in travel times for two events observed at one station can be attributed to the

spatial offset between the events with high accuracy. This is because the absolute errors are of common origin except in the small region where the ray paths differ at the sources. This technique carries out a simultaneous relocation of events with large distance from stations. It is possible to further improve the location precision using waveform cross-correlation methods. Two earthquakes produce similar waveforms at a common station if their source mechanisms are virtually identical and their sources are co-located so that the signal scattering due to velocity heterogeneities along the ray paths is small.

If we consider the arrival time *T*, for an *i* earthquake recorded by *k* seismic station, it is defined by:

$$T_k^i = \tau^i + \int_i^k u ds \qquad (2.32)$$

where τ is the origin time of event *i*, *u(s)* is the slowness field ($u(s) = 1/v(s)$, *v(s)* is wave velocity) and ds is an element of path length. Eq. (2.32) is not a linear equation. A truncated Taylor series expansion is generally used to linearize this equation. The resulting problem then is one in which the travel-time residuals, *r*, for an event *i* are linearly related to perturbations, $\Delta\mathbf{m}$, to the four current hypocentral parameters for each observation *k*:

$$\frac{\partial t_k^i}{\partial \mathbf{m}} \Delta\mathbf{m}^i = r_k^i \qquad (2.33)$$

where $r_k^i = (t^{obs} - t^{cal})_k^i$, t^{obs} and t^{cal} are the observed and theoretical travel time, respectively, and $\Delta\mathbf{m}^i = (\Delta x_i, \Delta y_i, \Delta z_i, \Delta\tau_i)$ (see Fig. 2.1).

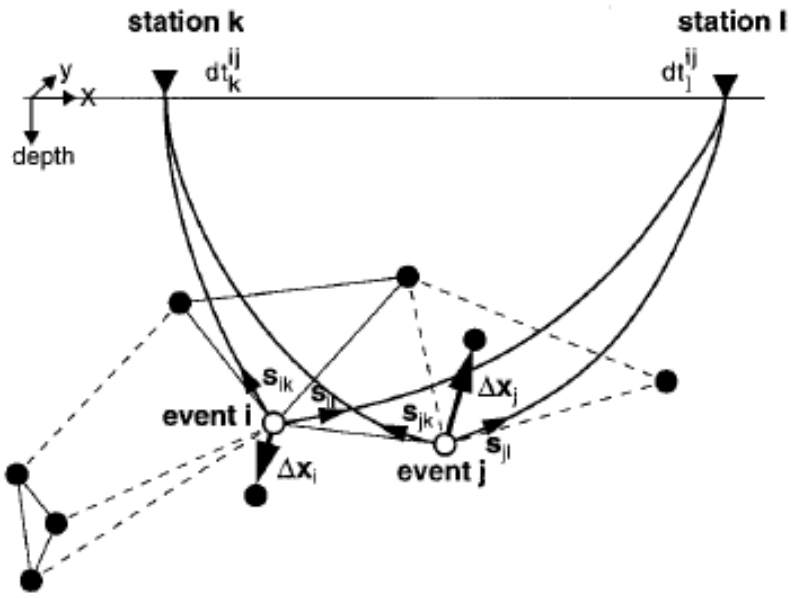

Figure 2.1: DD earthquake relocation algorithm illustration. Black and white circles show trial hypocenters that are linked to neighboring events by cross-correlation (solid line) or catalogue (dashed line) data. The black triangles are the *k* and *l* stations that record the *i* and *j* events (from Waldhauser and Ellsworth, 2000).

If we consider travel-time differences between two events *i* and *j*, $\left(t_k^i - t_k^j\right)^{obs}$, an equation for the relative hypocentral parameters between this events, considering Eq. (2.33), is:

$$\frac{\partial t_k^{ij}}{\partial \mathbf{m}} \Delta \mathbf{m}^{ij} = d\mathbf{r}^{ij} \qquad (2.34)$$

where $\Delta \mathbf{m}^{ij} = \left(\Delta dx^{ij}, \Delta dy^{ij}, \Delta dz^{ij}, \Delta d\tau^{ij}\right)$is the change in the relative hypocentral parameters between the two events, and the partial derivatives of *t* with respect to **m** are the components of the slowness vector of the ray connecting the source and receiver measured at the source. In Eq. (2.34) the source is the centroid of the two hypocenters, assuming a constant slowness vector for the two events. dr_k^{ij} is the residual between observed and calculated differential travel time between the two events defined by:

$$dr_k^{ij} = \left(t_k^i - t_k^j\right)^{obs} - \left(t_k^i - t_k^j\right)^{cal} \qquad (2.35)$$

Applying the Eq. (2.33) to each event and subtracting the two equations we obtain:

$$\frac{\partial t_k^i}{\partial \mathbf{m}} \Delta \mathbf{m}^i - \frac{\partial t_k^j}{\partial \mathbf{m}} \Delta \mathbf{m}^j = dr_k^{ij} \qquad (2.36)$$

or written out in full:

$$\frac{\partial t_k^i}{\partial x}\Delta x^i + \frac{\partial t_k^i}{\partial y}\Delta y^i + \frac{\partial t_k^i}{\partial z}\Delta z^i + \Delta\tau^i - \frac{\partial t_k^j}{\partial x}\Delta x^j - \frac{\partial t_k^j}{\partial y}\Delta y^j - \frac{\partial t_k^j}{\partial z}\Delta z^j - \Delta\tau^j = dr_k^{ij} \quad (2.37)$$

$\Delta x, \Delta y, \Delta z,$ and $\Delta\tau$ are the changes required in the hypocentral parameters to make the model better fit the data.

We combine equation (2.37) for all hypocentral pairs for a station, and for all stations to form a system of linear equations of the form:

$$\mathbf{WGm} = \mathbf{Wd} \quad (2.38)$$

where **G** defines a matrix of size $M \times 4N$ (M, number of double-difference observations; N, number of events) containing the partial derivatives, **d** is the data vector containing the double-differences (2.34), **m** is a vector of length $4N$, $[\Delta x.\Delta y, \Delta z, \Delta T]^T$, containing the changes in hypocentral parameters we wish to determine, and **W** is a diagonal matrix to weight each equation. The DD residuals for pairs of earthquakes at each station are minimized by weighted lest squares using the SVD method (see section 2.2.1 Eq.2.23) or the conjugate gradients method (LSQR, Paige and Saunders, 1982). The SVD method is useful for examining the behaviour of small systems (about 100 events depending on available computing capacity). The LSQR method takes advantage of the sparseness of the system of DD-equations and is able solve a large system efficiently. LSQR solves the damped least-squares problem:

$$\left\| \mathbf{W}\begin{bmatrix}\mathbf{G} \\ \lambda\mathbf{I}\end{bmatrix}\mathbf{m} - \mathbf{W}\begin{bmatrix}\mathbf{d} \\ \mathbf{0}\end{bmatrix} \right\|_2 = 0 \quad (2.39)$$

Chapter 3

Data collection

The area of the Lucanian Apennines is one of the main seismically active regions of Southern Italy. The recent improvement of the station coverage and the increased number of three-component broad band sensors of the Italian seismic network, together with two temporary seismic arrays (SAPTEX and SeSCAL) deployed in Southern Apennines in the last decade, allow us to achieve more accurate seismotectonic information about this area. To do this, I created a high quality database.

In a first time, I picked the arrival times of events recorded by the Italian permanent network (RSNC) and those recorded by the SAPTEX temporary array. The ENI-AGIP network data were used only for some events located in the Upper Val d'Agri and neighbouring areas. I used this data to perform the first analysis described in Chapter 4 and 5. After, with the end of SeSCAL experiment I incremented the database handpicking new records. Final dataset consists of 15,666 P- and 9228 S-arrival times associated to 1047 earthquakes with magnitude $M_L \geq 1.5$. I assigned a weighting factor based on the uncertainty estimates to each arrival time. I used weight 1, 2, 3, and 4, respectively, for a picking accuracy of 0.05, 0.10, 0.25 and 0.50 s. Table 3.1 shows the comparison between my final and the initial dataset in order to quantify the improvement achieved in the last two years of the observation period (2007–2008) thanks to the SeSCAL passive experiment. I located also events recorded only by the SeSCAL temporary experiment. As shown in Table 3.1, the number of P- and S-waves arrival times is almost doubled.

In this chapter I shortly describe the RSNC, the SAPTEX and our SeSCAL temporary array.

Dataset	Recording arrays	P-picks	S-picks	Relocated events	Quality A	Quality B	Quality C	Quality D	Focal mechanisms
A	RSNC, SAPTEX	7570	4956	359	226	69	31	33	58
B	RSNC, SAPTEX, SeSCAL	15666	9228	566	319	155	92	111	102

Table 3.1: Local earthquake datasets examined by (A) Maggi et al. (2009) and (B) Frepoli et al. (2011).

3.1 The Italian national seismic network (RSNC)

The RSNC monitors the entire Italian territory through a network of sensors that are connected in real time to the data acquisition system in Rome. It provides the data regarding the location and magnitude of earthquakes to the agencies of civil protection. In addition to monitoring of italian seismicity, the INGV observes the seismicity of the Mediterranean countries through the MedNet network. Moreover, thanks to the connections and data exchange with networks and analysis centers around the world, the staff on duty supervise the seismic activity of the entire earth globe.

Until 1984, data were recorded only on thermal paper in analogical mode. But since 1984 they are recorded both in analogical and digital form. In the latter years the RSNC has achieved a significant increase (305 seismic stations). Given the shape of the Italian peninsula and the distribution of seismicity, INGV has recently worked for the extension of the seismic network offshore with a group of OBS / H (Ocean Bottom Seismometer with Hydrophone) that have been installed on the seabed (D'Anna et al., 2009). Moreover, during the observation period, the permanent RSNC network improved significantly in Southern Italy, increasing both the station coverage and the number of three component extended band (Lennartz 5 s) or broad band (Trillum 40 s) sensors, which replaced the Kinemetrics S-13 short period sensors.

3.2 SAPTEX temporary array

The SAPTEX array was planned with the main goal to better resolve the crustal and upper mantle structure beneath Southern Italy. In this region the paucity of permanent seismic stations is still remarkable, thus preventing high-resolution tomographic studies, precise hypocentral determination, and detailed definition of the lithosphere-asthenosphere structure. Focusing on these objectives a passive tomographic experiment was carried out from 2001 to 2004. Figure 3.1 shows the distribution of the recording sites occupied by the SAPTEX array (circles) and the National Centralized Seismic Network (RSNC, squares) in Southern Italy. The deployment of the portable digital seismographs started at the end of June 2001. The first ten temporary stations (the 2001 array) were placed mostly in the Apulia and Basilicata regions, with the aim of reducing the large spacing (< 70 km) among the permanent existing stations. During 2002, nine new recording sites were added to increase the station coverage. Two stations of the 2002 array, SX15 and SX18, were in the Aeolian volcanic archipelago, on the Stromboli and Alicudi Island, respectively. These locations (Table 3.2), although quite noisy, were chosen to better constrain the hypocentral determination of the intermediate and deep seismicity characterizing the Tyrrhenian slab (Frepoli et al., 1996). The geometry of the passive array has been notably improved by the 2003 and 2004 field programs that included eleven subsequent recording sites mainly located in Calabria, Aeolian Islands, and in the southern part of Apulia (Fig. 3.1). For each station was installed a 24 bit RefTek 72A07 digitizer, a three-components Lennartz 3D-5 s sensor (LE-3D/5s) (Cimini et al., 2006). To avoid losing important seismic data, the stations were set to operate in continuous mode recording. In particular, the SAPTEX data were acquired at 50 sps.

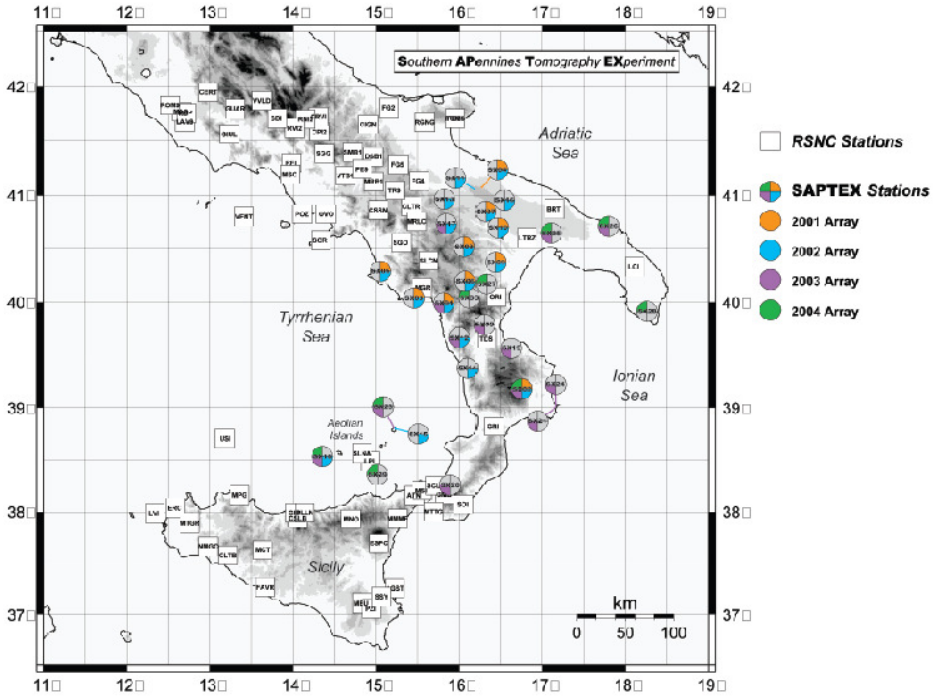

Figure 3.1: The figure reports the station distribution for the SAPTEX temporary array.

Station code	Site	Latitude (N)	Longitude (E)	Elevation (m)
SX01	Castrocucco	39.99380	15.81556	665
SX02	Timpagrande	39.17936	16.75829	810
SX03	S. Giovanni a Piro	40.04109	15.45744	585
SX04	Castel del Monte	41.07758	16.27273	529
SX05	Rocca Cilento	40.29556	15.05511	682
SX06	S. Chirico Raparo	40.19924	16.07590	968
SX07	Barisci	40.84924	16.32098	469
SX08	Pietrapertosa	40.52148	16.06124	1077
SX09	Craco	40.37643	16.44330	367
SX10	Picciano	40.69913	16.47064	481
SX11	Minevino Murge	41.06109	16.19586	598
SX12	S. Sosti	39.66635	16.00190	588
SX13	Venosa	40.96438	15.82344	460
SX14	Montalto Uffugo	39.37976	16.10046	990
SX15	Stromboli-S. Vincenzo	38.80264	15.23423	125
SX16	Quasano	40.95423	16.54832	520
SX17	Pietragalla	40.73605	15.84764	870
SX18	Alicudi	38.53381	14.35637	156
SX19	Rossano	39.57064	16.63017	433
SX20	Celeste	38.26031	15.89393	694
SX21	Isola Capo Rizzuto	38.99696	17.15433	152
SX22	Cassano allo Jonio	39.78891	16.30720	473
SX23	Stromboli-P. Labronzo	38.80988	15.21803	165
SX24	Crotone	39.01600	17.16438	166
SX25	Massafra	40.64908	17.11090	431
SX26	Carovigno	40.71468	17.79966	43
SX27	Senise	40.17409	16.36029	298
SX28	Specchia	39.94845	18.27091	203
SX29	Vulcano	38.39664	14.96412	159
SX30	San Severino Lucano	40.01356	16.14173	924

Table 3.2: Description of the SAPTEX sites by Cimini et al. (2006).

3.3 SeSCAL temporary array

The SeSCAL project was planned specifically for my study of background seismicity (scattered events and earthquakes with $M_L \leq 3$) and crustal structure of the Lucanian Apennines and surrounding areas. The ten temporary stations (Fig. 3.2) have operated in the period between December 2007 and December 2008. They were placed mostly in the Apulia and Basilicata regions, where the RSNC was not very dense (Table 3.3). The RT07 station located in Filiano Atella was later moved to Lagopesole and renamed RT12. Alike the RT05 station located in Marsico Vetere was moved to nearby area and renamed RT11. The ten portable seismographs, installed in this project, were all equipped with high-dynamic digitizers (REFTEK RT130) and three-component extended band sensors (Lennartz 3D/5s). In particular, to avoid losing important seismic data, the stations were set to operate in continuous mode recording with a sampling frequency of 100 Hz to better record low-magnitude, high-frequency local earthquakes. Figure 3.3 shows a seismogram recorded by the SeSCAL stations.

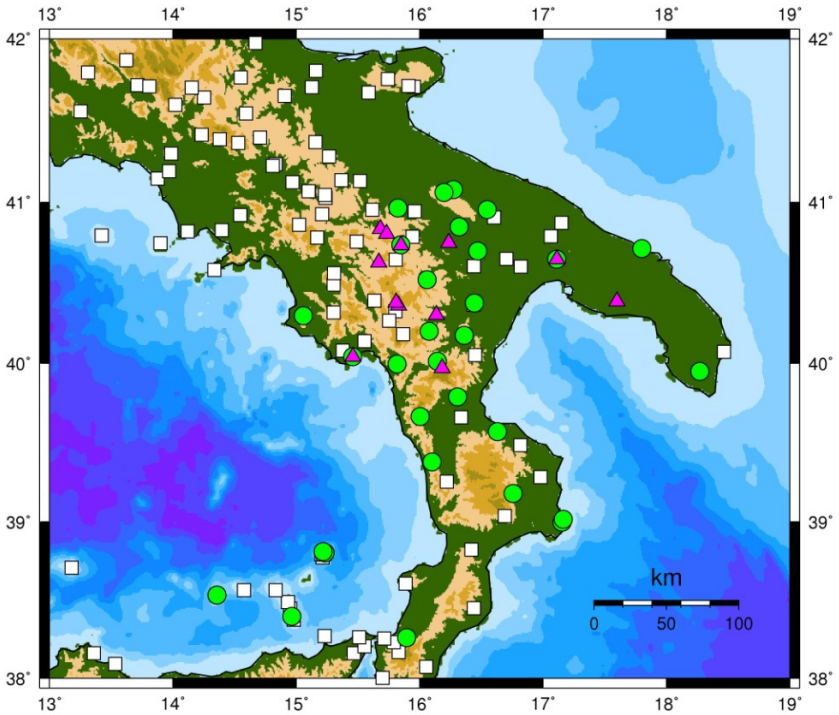

Figure 3.2: SeSCAL temporary array distribution (magenta triangles), SAPTEX temporary stations (green circles) and Italian National Network (white squares).

Station code	Site	Latitude (N)	Longitude (E)	Elevetion (m)
RT01	San Severino Lucano	39.9415	16.1812	1090
RT02	Uggiano Motefusco	40.3868	17.5975	139
RT03	Picerno	40.6292	15.6685	771
RT04	Gallicchio	40.3024	16.1365	801
RT05	Marsico Vetere	40.36	15.8267	694
RT06	San Giovanni a Piro	40.0412	15.4575	545
RT07	Filiano Atella	40.8352	15.68	482
RT08	Massafra	40.649	17.1108	423
RT09	Pietragalla	40.736	15.9815	826
RT10	Irsina	40.7498	16.2348	608
RT11	Marsico Vetere	40.379	15.807	722
RT12	Lagopesole	40.8062	15.7317	481

Table 3.3: Description of the SeSCAL sites.

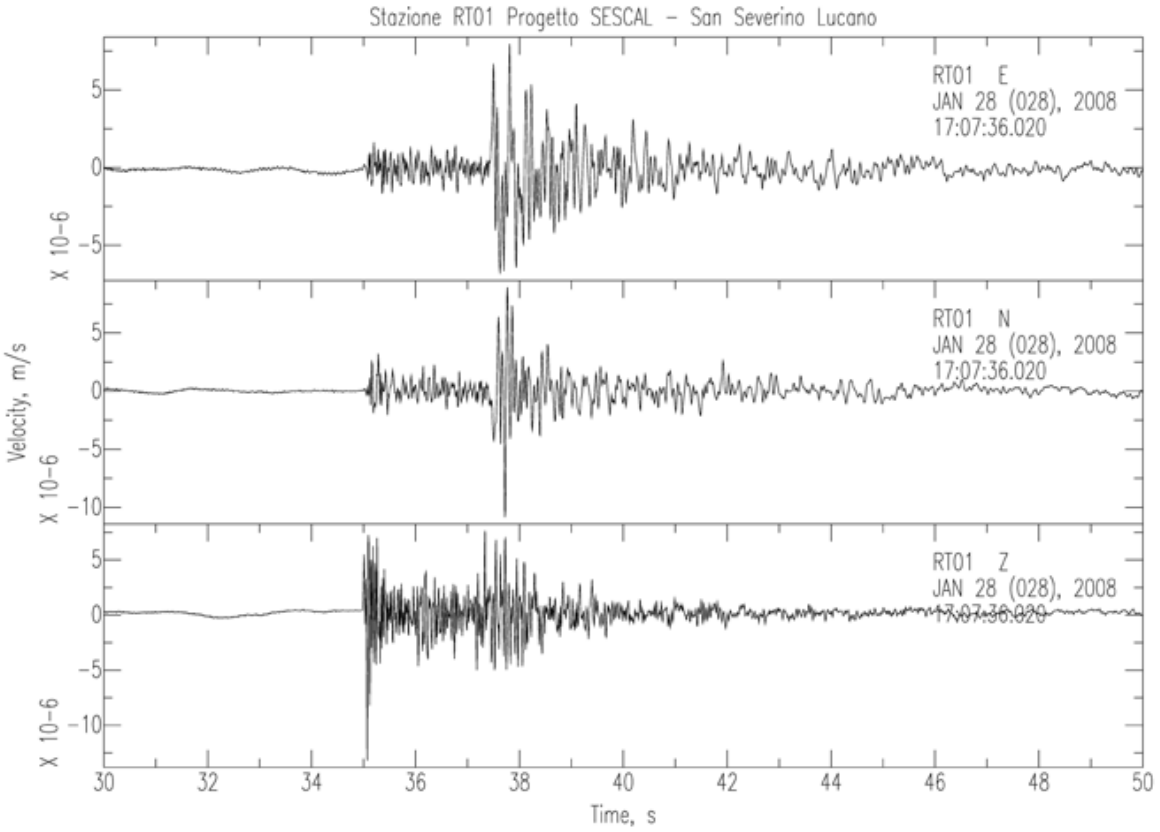

Figure 3.3: Examples of seismograms recorded by the temporary array.

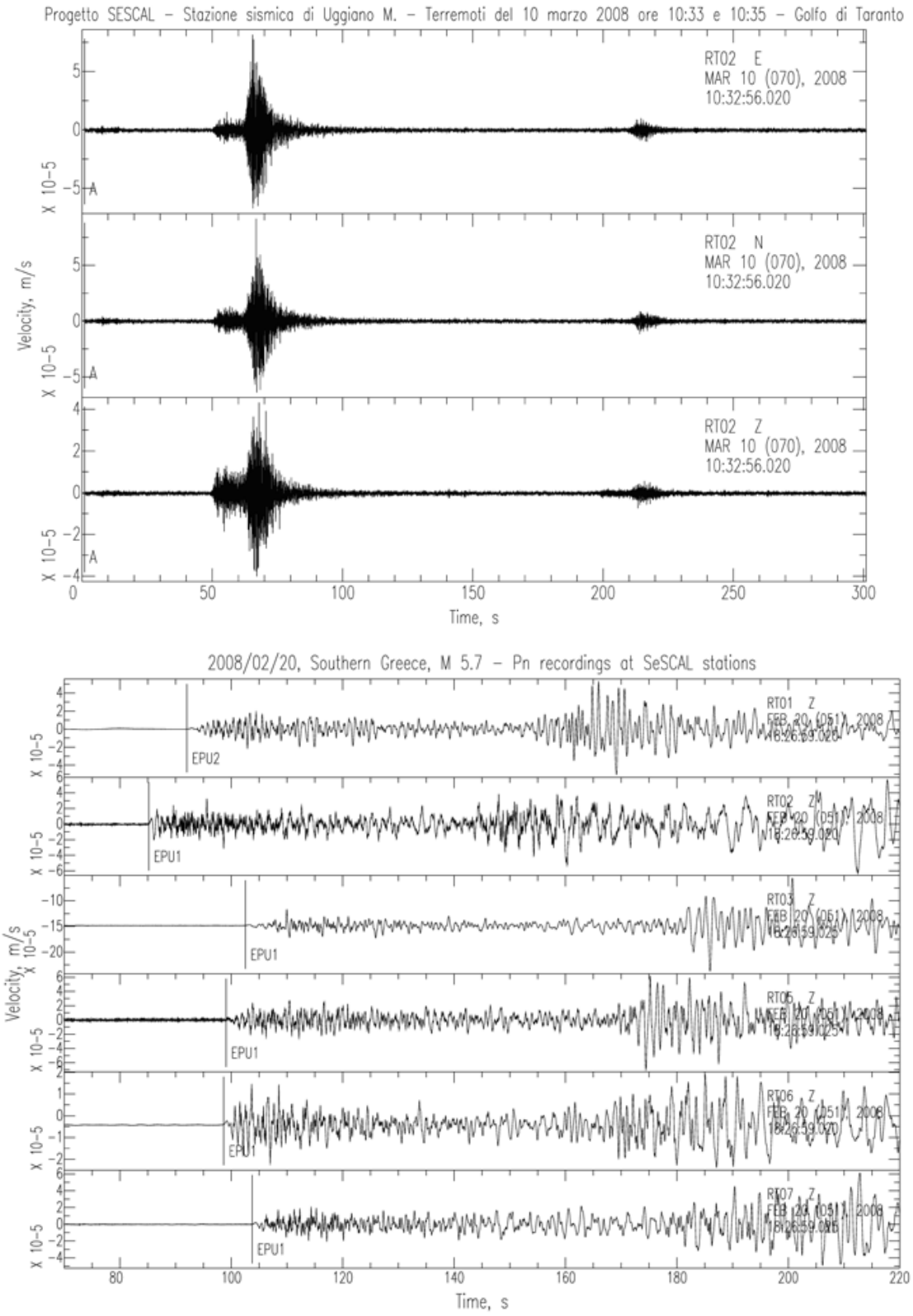

Figure 3.3: (continued).

Chapter 4

1D velocity model for Southern Apennines

A detailed seismicity pattern is very important to obtain a real image of earthquakes distribution essential to reveal or confirm seismogenic structures in the study area. However, this aim is hard because it is related to network geometry, picking accuracy, number of phases and velocity model for P-and S-waves. Moreover, a 1D-velocity model for P-wave and a V_P/V_S ratio were used as input to compute 1D velocity model for S-wave to locate earthquakes. This chapter describes initial analysis important to obtain accurate locations. A V_P/V_S ratio and a reference *P*-wave one dimensional (1D) velocity model close to the true earth model together with station corrections (Kissling, 1988) were computed. The latter mitigates the effects of the deviations from the simple, laterally homogeneous model and of the structure close to the receiver. These results were the first step necessary to improve the hypocentral determinations of the background (scattered events and earthquakes with $M_L \leq 3$) and higher seismicity for the Lucanian Apennines and surrounding area. In this first step I used the initial database. It was created by re-picked arrival times of earthquakes recorded by the RSNC seismic network, by the temporary SAPTEX network (between June 2001 and December 2006) and the ENI-AGIP network only for few events located in the Upper Val-d'Agri and surrounding areas (see Chapter 3). This database was increased in the later time with the SeSCAL experiment data and used for other analysis described in the Chapter 5, 6 and 7.

4.1 VP/VS ratio

I used a modified Wadati method (Chatelain, 1978) to compute an average V_P/V_S ratio shortly described in the Chapter 2.

Fitting DT_S versus DT_P for all available pairs of stations gives the value of the slope V_P/V_S. Weights are defined for pairs of $P_{i,j}$ and $S_{i,j}$ as the highest weight of the four P and S weights. I assigned a weight (*W*) to each *P* or *S* arrival on the basis of picking accuracy (see Chapter 3). Plotting only weights of 0, 1 or 2 (Pontoise and Monfret, 2004), I obtained a V_P/V_S ratio of 1.83 with 95% prediction bounds (1.828, 1.829), root mean square error (rms) of 0.025 and linear correlation coefficient (R) of 0.98 (Fig. 4.1).

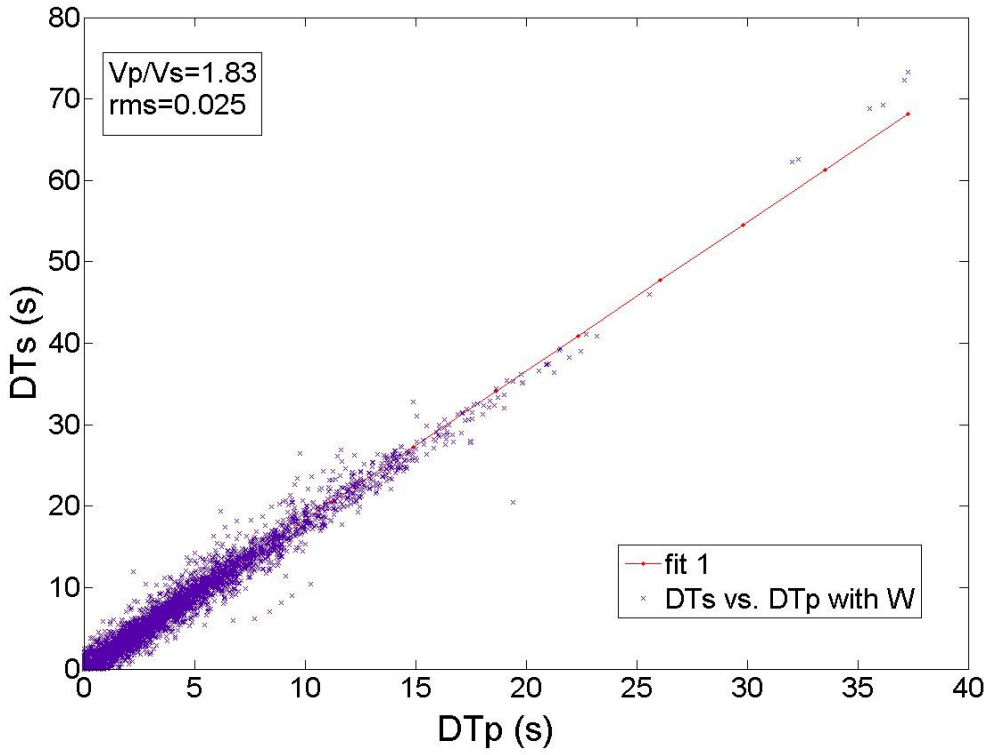

Figure 4.1: V_P/V_S ratio for the Lucanian Apennines considering the weights (*W*). Linear fit of DT_s versus DT_P using the Linear Least Squares Method. The root mean squared error (*rms*) is 0.025, and the linear correlation coefficient (*R*) is 0.98.

4.2 1D velocity model

I used the VELEST algorithm (Kissling et al., 1995) to perform an analysis of the data for the best P-wave one-dimensional (1D) velocity model of the study area and station corrections (for more details see Appendix A). Previous studies do not show a 1D model calculated in the restricted area of the Lucanian Apennines. Through VELEST I searched a 1D velocity model that minimizes the least square solution to the coupled hypocentral–velocity model parameter solution. As this procedure does not invert for changes in layer thickness, I started from several initial models with varying thickness. In this way, I introduced some layers with thickness of 3 or 4 km, up to 30 km depth, and of 5 km for greater depths. To account for the station elevations, I included an approximate additional layer with thickness of 2 km over the sea level and V_P=5 km/s.

I used three different starting models: the first two were taken directly from the seismological literature as Chiarabba and Frepoli (1997) and Chiarabba et al. (2005), respectively. The latter is obtained using data of some Lucanian Apennine seismic studies (Merlini and Cippitelli, 2001; Cassinis et al., 2003; Barberi et al., 2004; Tiberti et al., 2005). In a first step the 514 earthquakes were located using the HYPOELLIPSE code (Lahr, 1989, Appendix B). I used mainly the direct *P*-wave arrivals, recorded by stations with a maximum epicentral distance around 300 km. I selected appropriate control parameters as described in Appendix A.

The first starting model was computed by Chiarabba and Frepoli (1997) for Southern Italy, and it is made of seven layers with a linear increase of velocity with depth. For this model, I increased the number of layers (*Model1*). I performed two tests: the first with the possibility to find low velocity layers and the second without it. However, I didn't observe a low velocity layer. Adjacent layers not resolved by the data are merged into a single layer during VELEST iterations. In this way, I used 308 selected events of my dataset. I chose all well located events with root main square error rms < 1 s, minimal number of 6 P-phases. Initially, I put the maximum iteration number ITTMAX=30 to plot the rms function (Fig. 4.2). I observed that the rms value is stabilized at iteration number 14 and I put this value as ITTMAX to computed 1D- velocity model.

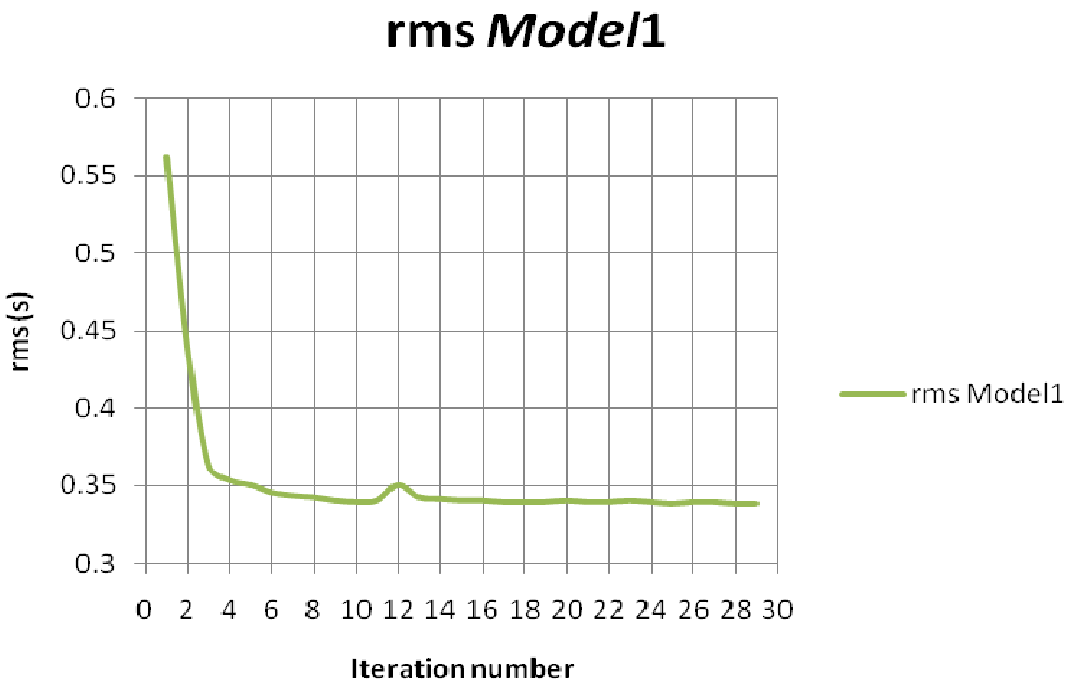

Figure 4.2: Rms distribution for the *Model1* (Chiarabba and Frepoli, 1997stratified).

I computed the 1D velocity model *Vel_9* (Fig. 4.3a) obtaining an average rms equal to 0.34 s whereas the initial value was 0.56 s. The selected earthquakes show an average azimuthal gap of 133°. This model shows a Moho at 40 km depth. Fig. 4.3b shows large amounts of earthquakes in the depth interval 3–14 km, while at greater depth intervals the smaller amount of events does not allow for an improvement of the velocity model within the deeper layers.

The second starting model is a regional model computed by Chiarabba et al. (2005) for the entire Italian region. It consists of seven layers and includes a velocity inversion at 20 km of depth, within the lower crust beneath the Apennine belt. I re-parameterized the layers of the initial model to better estimate the depth of the main discontinuities. Starting from this model (*Model2*) during the test before described, I didn't observe low velocity layers and the rms is stabilized at ITTMAX=20 (see Fig. 4.4).

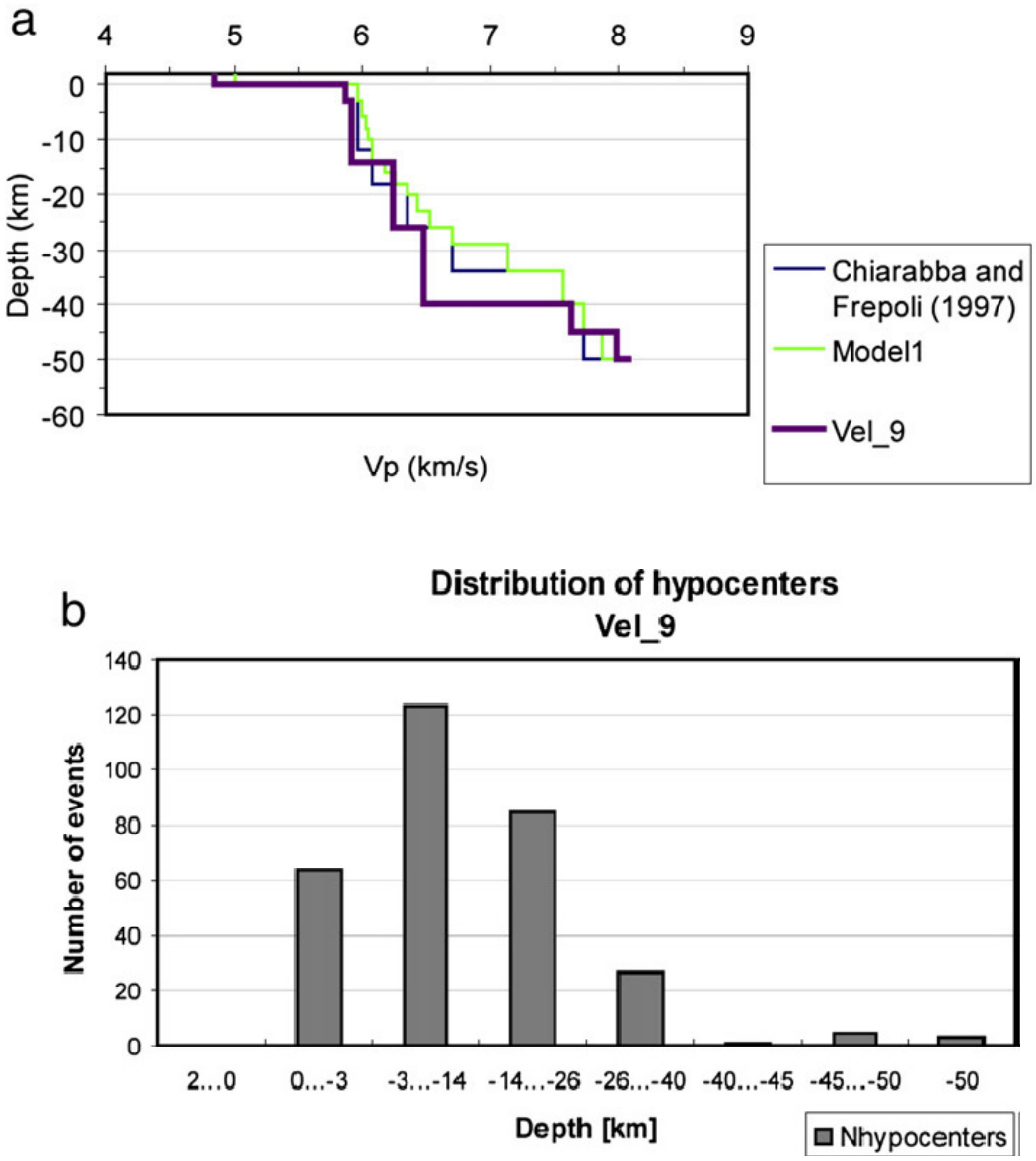

Figure 4.3: a) Starting P-wave velocity model for the Italian region computed by Chiarabba and Frepoli (1997). We increased the number of layers: thickness of 3 or 4 km for each layer, up to 30 km depth, and of 5 km below 30 km depth. I named this model *Model1*. *Vel_9* is the final velocity model obtained with VELEST. b) Hypocentral distribution versus depth for the model *Vel_9* (modified from Maggi et al., 2009).

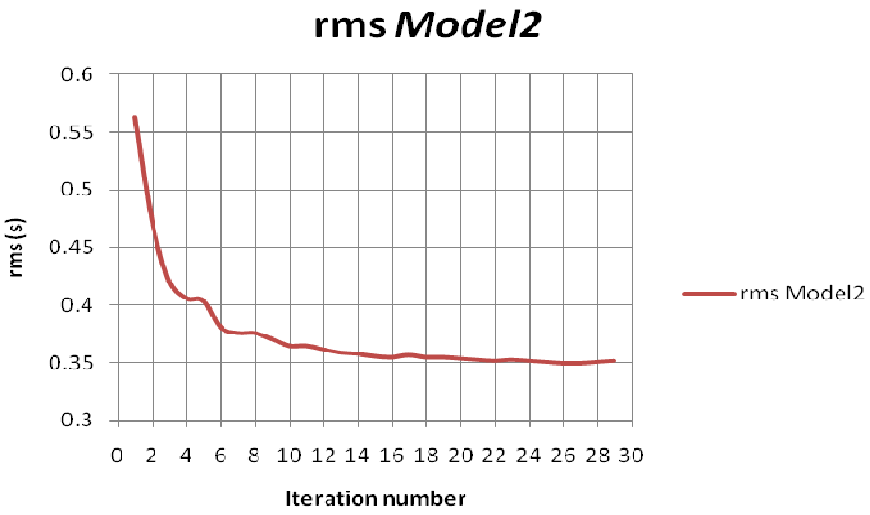

Figure 4.4: Rms distribution for the *Model2* (Chiarabba at al., 2005 stratified).

We applied the VELEST code obtaining the final model *Vel_8* (Fig. 4.5a). For the inversion, I used 315 selected events. The final model shows a Moho at 34 km depth and the average rms is equal to 0.35 s whereas initial average value is 0.56 s. This model yields a larger amount of earthquake hypocenters within the 13–34 km depth interval (Fig. 4.5b).

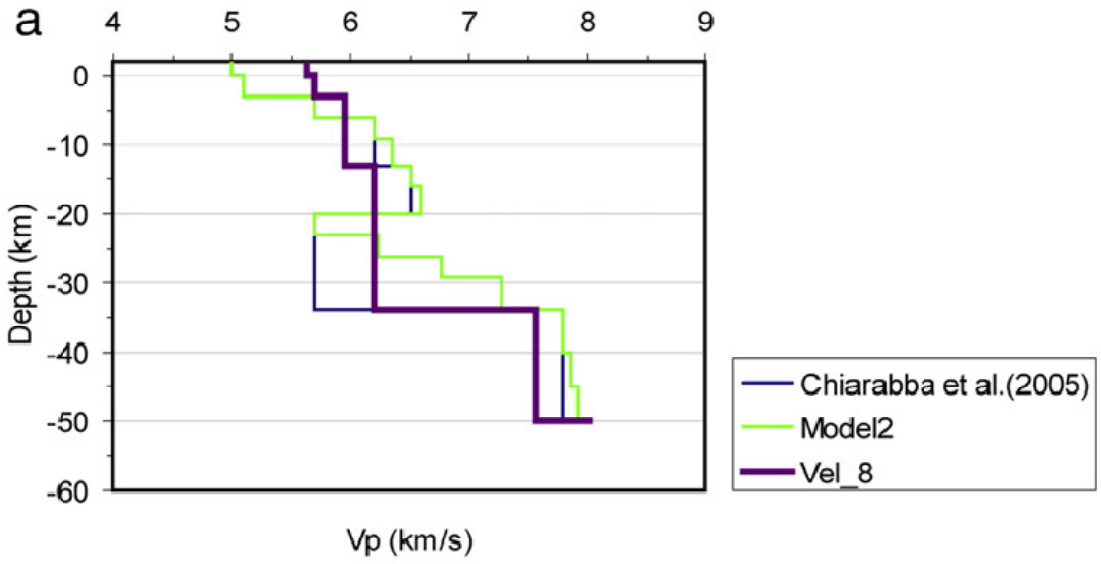

Figure 4.5: a) Starting P-wave velocity model for the Southern Italy computed by Chiarabba et al. (2005). The number of layers is increased (see caption to Fig. 4.2).We named this model *Model2*. *Vel_8* is the final velocity model obtained with VELEST. b) Hypocentral distribution versus depth for the model *Vel_8* (modified from Maggi et al., 2009).

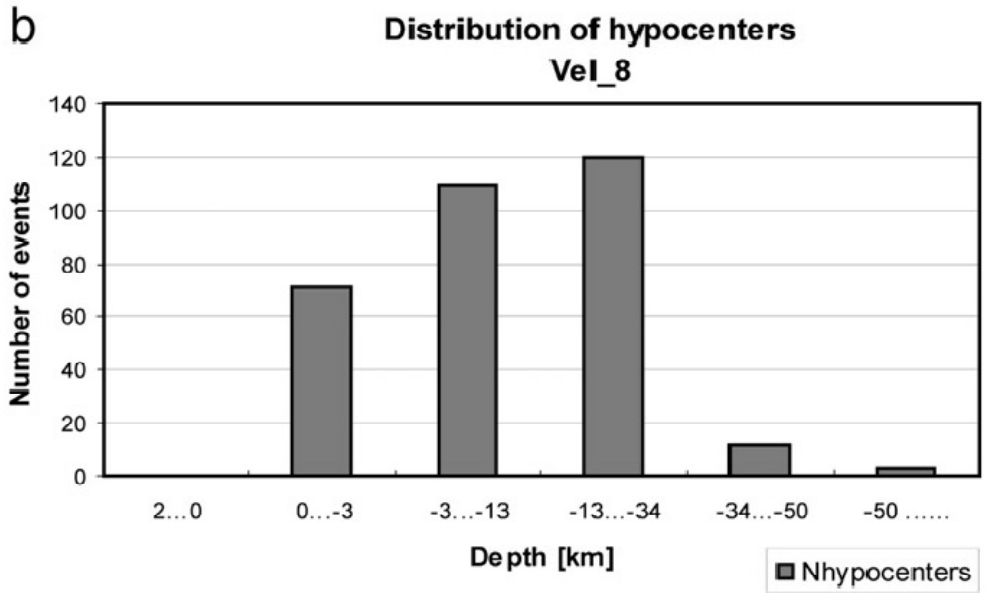

Figure 4.5: (continued).

The third starting model, called *Test*, is obtained from some seismic studies in the Lucanian Apennines (Tiberti et al., 2005; Barberi et al., 2004; Cassinis et al., 2003; Merlini and Cippitelli, 2001). It is made of six layers with an increase of velocity with depth. The correspondent increased layer model is called *Teststra*. I didn't observe low velocity layers and the rms is stabilized at ITTMAX=15 (see Fig. 4.6). With VELEST iterations I merged adjacent layers not resolved by the data and computed the final model *Test_8* (Fig. 4.7a) using the 307 selected events. The Moho depth is at 35 km and the final average rms is 0.34 s whereas initial value is 0.66 s. Fig. 4.7b shows a large amount of earthquake hypocenters within the 11–23 km depth range.

Since the studied area is characterized by few deep events, I cannot well constrain the velocity model beneath the Moho. As shown in Fig. 4.8, the velocity of the three final models is similar especially where there is a larger amount of earthquakes and of number of rays that better constrains the model (see Table 4.1). Topmost layers are mostly subvertically and bottom layers are mostly subhorizontally penetrated. Therefore, the resolution in these layers is generally lower than in the central layers that contain the hypocenters (Kissling, 1995).

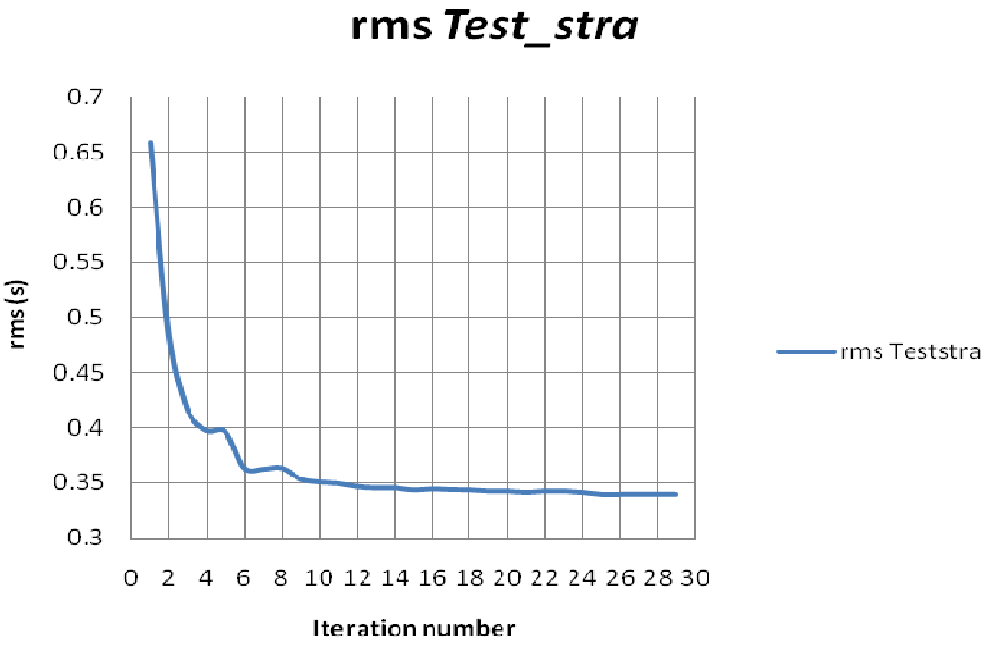

Figure 4.6: Rms distribution for the *Teststra* (*Test* stratified).

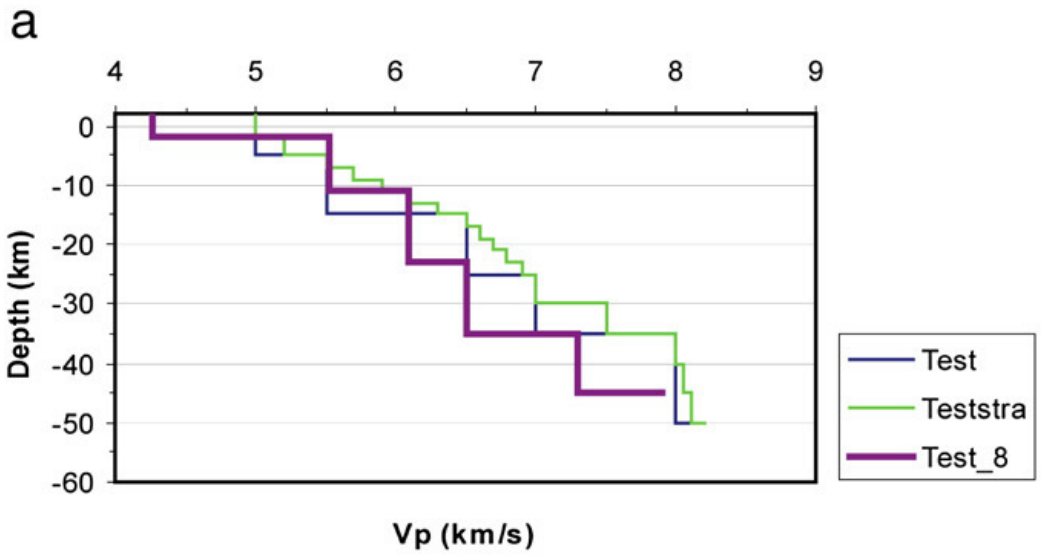

Figure 4.7: a) Starting P-wave velocity model *Test* for the Lucanian Apennines. The number of layers was increased (see caption Fig. 4.3).We named this model *Teststra*. *Test_8* is the final velocity model obtained with VELEST. b) Hypocentral distribution versus depth for the model *Test_8* (modified from Maggi et al., 2009).

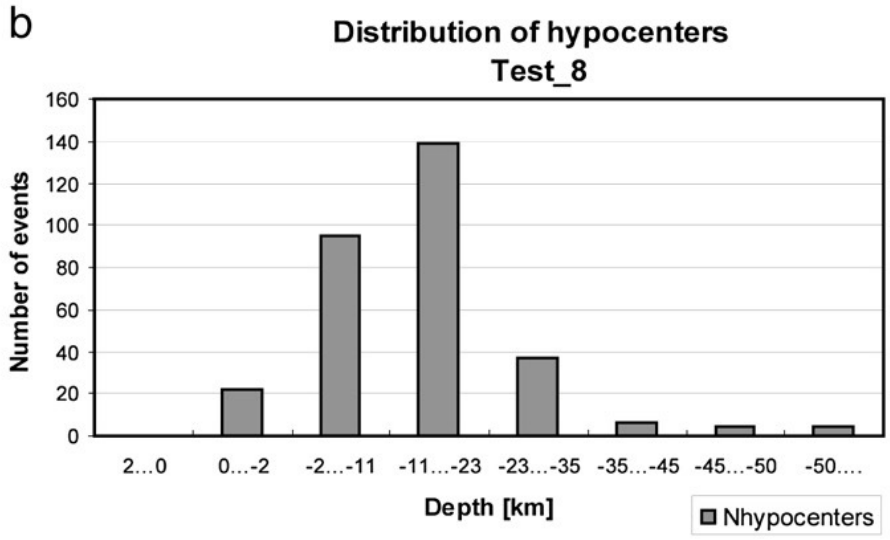

Figure 4.7: (continued).

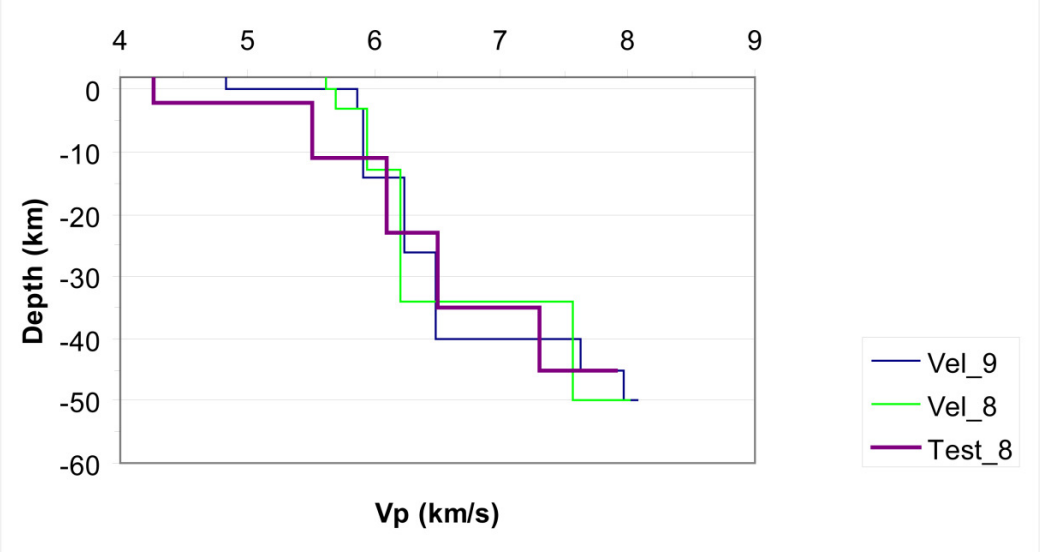

Figure 4.8: P-wave velocity final models obtained by VELEST. *Vel_8* is the model derived from *Model2*, *Vel_9* from *Model1* and *Test_8* from *Teststra* (from Maggi et al., 2009).

Moreover, models *Vel_8* and *Test_8* do not show evident velocity changes within the shallowest layer. The Moho depth (40 km) obtained in the model *Vel_9* is larger than the value estimated by previous studies. The wide-angle reflection–refraction seismic exploration method (DSS) (Tiberti et al., 2005; Cassinis et al., 2003; Merlini and Cippitelli, 2001;

Morelli, 1997) and the global model *Crust2.0* (Bassin et al., 2000) finds a Moho generally around 30–35 km depth.

Layers (km)	*Vel_9* NHIT	Layers (km)	*Vel_8* NHIT	Layers (km)	*Test_8* NHIT
-2...0	0	-2…0	0	-2…0	0
0…3	64	0…3	71	0…2	22
3…14	123	3…13	109	2…11	95
14…26	85	13…34	120	11…23	139
26…40	27	34…50	12	23…35	37
40…45	1	50…	3	35…45	6
45…50	5			45…	8
50…	3				

Table 4.1: Number of rays passed thru a layer (NHIT) for the three final models.

Moreover, the crust beneath the Apenninic chain is characterized by a doubling of the Moho depth: the Tyrrhenian Moho depth increases from 15 to 25 km moving from the Tyrrhenian Sea to the ENE, while the Adriatic Moho deepens from 24 km under the Gargano promontory to 50 km under the Eastern margin of Tyrrhenian Sea (Ventura et al., 2007). The two models named *Vel_8* and *Test_8* show a Moho depth more consistent with that obtained from other studies (34 and 35 km of depth, respectively). The final 1D velocity model computed with VELEST code is strongly depends on the initial model and initial hypocenter locations (Kissling, 1995, see Appendix A). For this reason, in the further steps of this work, I used these models for earthquakes relocation.

Using the database with the seismicity recorded in the period between 2001 and 2006 I relocated all the 514 events of my dataset with the HYPOELLIPSE code using the two models *Vel_8* and *Test_8*. I took into account earthquakes with azimuthal gap < 180° and root mean square of the travel-time residuals rms < 1.0 s. In this way I relocated 337 events using model *Vel_8*, with an average rms=0.29 s and 359 earthquakes using model *Test_8*, with an average rms=0.30 s. Using the model *Vel_8* I obtained 61.1% of events with quality A and 20.2% with quality B computed by HYPOELLIPSE code (see Table 4.2).

Quality	Larger of SEH and SEZ	Model *Test_8*		Model *Vel_8*	
		Number of events	% number of events	Number of events	% number of events
A	≤ 1.34	226	63%	206	61.1%
B	≤ 2.67	69	19.2%	68	20.2%
C	≤ 5.35	31	8.6%	40	11,9%
D	> 5.35	33	9.2%	23	6.8%

Table 4.2: Quality based on the value of the horizontal error SEH (68% confidence limit), and vertical error SEZ (68% confidence limit) (modified from Maggi et al., 2009).

Whereas considering the second model (*Test_8*) I had 63.0% of earthquakes with quality A and 19.2% with quality B. Model *Test_8* is also consistent with the results of DSS studies (Cassinis et al., 2003) and with the recent European Crustal model (EuCRUST-07) (Tesauro et al., 2008), which indicate lower crust V_P velocity around 6.5 km/s and Moho depth of ca 35 km beneath the Apennines. Following these results, I choose the model *Test_8* (Table 4.3) with station corrections shown in Figure 4.9.

Top of layer (km)	Velocity of model *Test8* (km/s)
0	4.27
-2	5.52
-11	6.1
-23	6.5
-35	7.31
-45	7.9

Table 4.3: Velocity values of the best model *Test_8* for Lucanian Apennines computed with VELEST code.

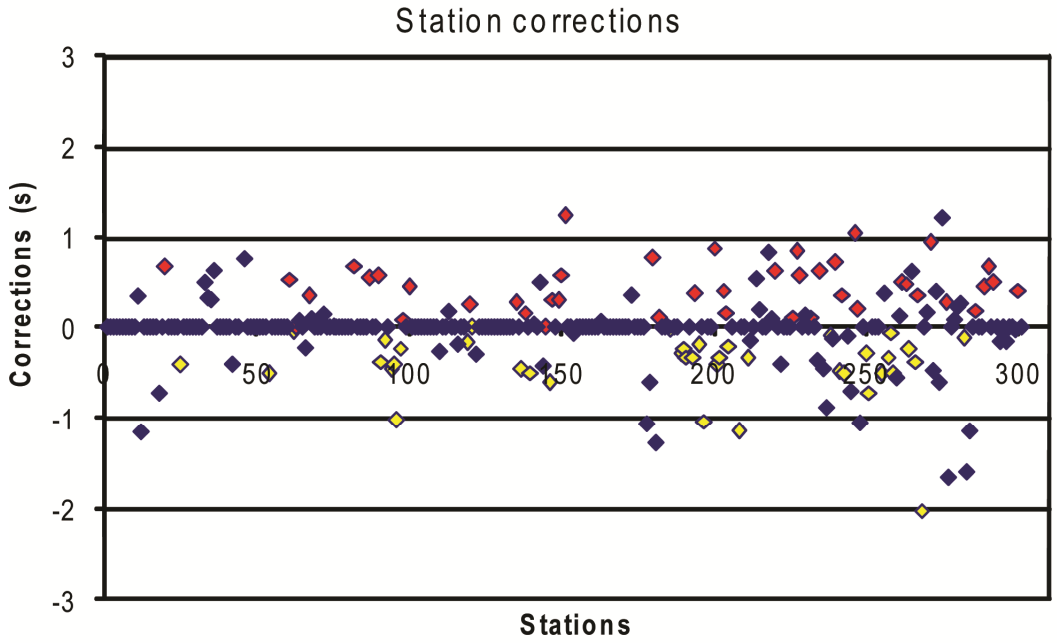

Figure 4.9: Plot of station corrections values obtained by VELEST using the initial model *Test*. The red and yellow rhombus are associated to the stations placed along the Apenninic chain peri-Tyrrhenian area and along the Adriatic area respectively.

4.3 Discussion

The main aim of this first analysis was to compute V_P/V_S, to obtain a model that approximates the real structure within the crust and station corrections for the area of Lucanian Apennines and surrounding zones to better constrain hypocentral locations. The computed value of V_P/V_S ratio is quite similar to that obtained by other studies in the same region (V_P/V_S =1.82, Frepoli et al., 2005). I found a relatively high value probably due at the presence of highly fractured zones related to the main faulting pattern in the study area (Gentile et al., 2000).

The regional gravity anomaly maps and DSS study outlined the existence of a doubling of the Moho beneath the Lucanian Apennines (Morelli, 2000; Tiberti et al., 2005). This area is characterized by a relative gravity low surrounded by areas with gravity high. This is likely related to the overlap of the Tyrrhenian and Adriatic Moho (Speranza and Chiappini, 2002;

Tiberti et al., 2005) beneath the Apenninic chain that would be associated to the subduction process. Through these analysis, I obtained a model in which the average Moho is set at 35 km depth, in agreement with the average depth defined for the Southern Apennines in previous works (Locardi and Nicolich, 1988; Cassinis et al., 2003). The average P-wave velocity (V_P=7.31 km/s) observed at the Moho discontinuity in these analysis is slightly lower than the average value (V_P=7.56 km/s) computed by Chiarabba and Frepoli (1997) for the Southern Italian region. Tomographic and geothermal gradient studies point out a brittle–ductile transition at 28–30 km beneath the foredeep and foreland compared with the 15–18 km of depth of the same limit beneath the chain (Harabaglia et al., 1997; Chiarabba and Amato, 1996). I computed an average limit brittle-ductile transition at 23 km. These data, together with positive Bouger anomalies, are consistent with the presence of an uprising asthenospheric material in the upper mantle below the Tyrrhenian margin of the chain and the adjacent Tyrrhenian Sea (Scrocca et al., 2005). Moreover, the doubling of the Moho beneath the Lucanian Apennines is interpreted as a "soft" asthenospheric wedge intruding between the down going Adriatic plate and the overriding plate (Ventura et al., 2007).

The station corrections computed in this work are positive along the Apennine belt indicating low velocities respect to reference model, while the negative values in the Adriatic area reflect high velocities related to carbonate platform.

Chapter 5

Seismotectonic study of Southern Apennines

The area of the Lucanian Apennines is one of the main seismically active regions of Southern Italy. The main goal of the analysis described in this thesis is to provide new insights on the seismotectonic in this portion of the Apenninic chain through a careful analysis of background seismicity and active stress field information retrieved from fault plane solution inversion. Present-day stress field data are important for the seismotectonic zonation, a basic tool for seismic hazard evaluation, and are helpful to know the behaviour of seismogenic faults. In this chapter, I show how I pursued these aims using standard methodologies.

I located the events with the HYPOELLIPSE code using the computed 1D-velocity model *Test_8*. I obtained a detailed seismicity distribution of earthquakes and I computed focal mechanisms and regional stress field. In the first time I performed these analyses with an initial dataset that is created by re-picked arrival times of earthquakes recorded by the RSNC seismic network, by the temporary SAPTEX network and the ENI-AGIP network only for few events located in the Upper Val-d'Agri and surrounding areas (see Chapter 3). Later, the database was considerately incremented with the SeSCAL passive experiment data (for more details see Chapter 3). I relocated new earthquakes, recomputed focal mechanisms and obtained a regional stress field.

Despite the short time interval of observation, the seismicity examined in this work is representative of the seismic behaviour of the Lucanian Apennines and surrounding regions. In fact, the spatial distribution of the analyzed events closely follows the pattern delineated by the seismicity of the last two decades.

5.1 Earthquakes location (first dataset)

The seismicity studied in this section occurred in the period between 2001 and 2006 and it is located within a ~350×160 km NW–SE elongated region.

Analyzing the hypocentral distribution obtained using the computed velocity model *Test_8* (Fig. 5.1a and b), I observe that most of the earthquakes are located beneath the Apenninic chain. The seismicity distribution enhances three main seismic active zones.

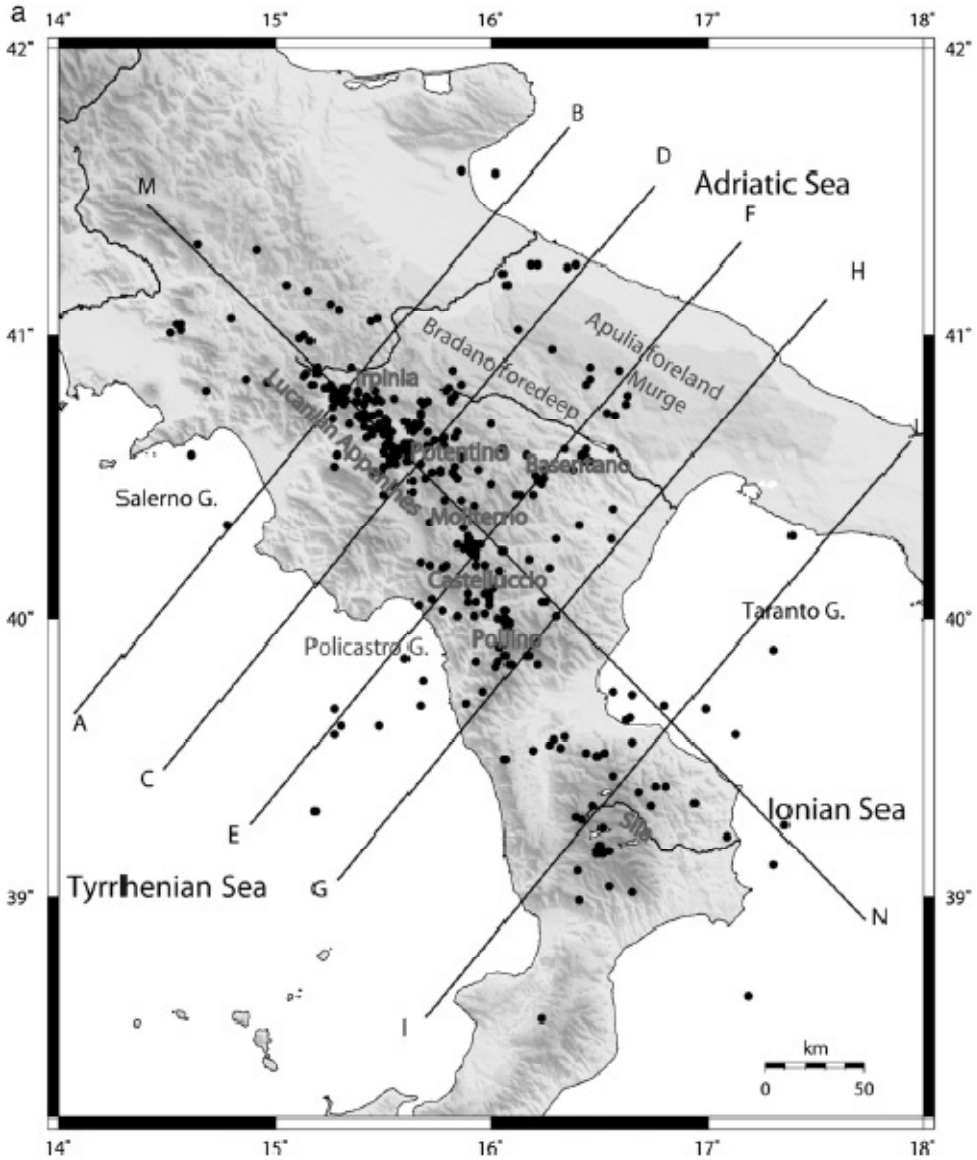

Figure 5.1: a) Epicentral distribution of the 359 earthquakes located using the model *Test_8*. The width of cross-sections AB, CD, EF, GH, and IL is 25 km. The width of cross-section MN is 200 km. b) Cross-sections with depth ≤ 50 km (from Maggi et al., 2009).

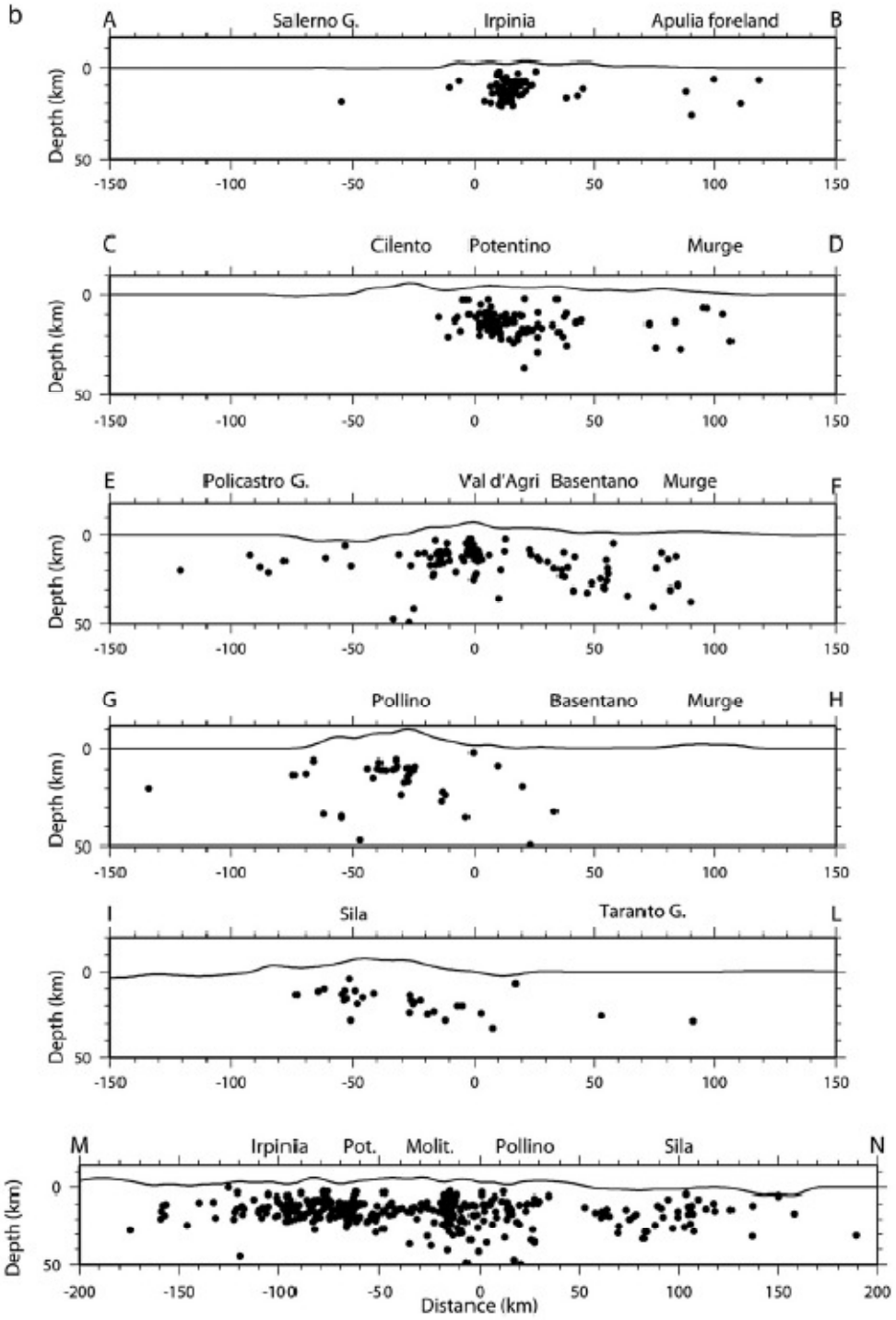

Figure 5.1: (continued).

The westernmost of these is characterized by an earthquake distribution centred mainly along the axis of the Lucanian Apennine with maximum hypocentral depths up to 20 km (see Fig. 5.1b, sections AB, CD, EF and GH). Only few subcrustal events are present within this crustal domain. The second seismic zone is defined by a sparse and deeper seismicity (see Fig. 5.1a, b) located within the eastern and outer margin of the chain and in the foredeep with depths up to 30 km. Finally, the last seismic zone (see Fig. 5.1b, section IL and MN; cross-section MN has a 200 km width) is located within the Sila Range and the offshore northeastern Calabrian coast also characterized by a sparse seismicity and a maximum hypocentral depth around 30 km. Considering section MN in Fig. 5.1b which includes all the relocated earthquakes, the seismicity reaches 40 km beneath the Southern Apennines with an increase of hypocentral depth in the middle portion of the section, beneath the Lucanian region. This section shows two large clusters of hypocenters: one located in the Irpinia–Potentino area, and the other beneath the Moliterno–Pollino area. A seismic gap between the Pollino and the Sila Ranges is clearly observable. Michetti et al. (1997) and Cinti et al. (1997) demonstrated that this area considered as a gap on the basis of historical and instrumental seismological data and hence evaluated of higher hazard. An isolated 88 km deep event belonging to the Southern Tyrrhenian subduction zone is located beneath the Castelluccio area. This earthquake belongs to the sparse seismicity that characterizes the northern edge of the subduction zone. Fig. 5.2 shows the error ellipses with the 99% confidence limits of the relocated earthquakes. Events with D quality (Table 4.2) are excluded from this figure. Error ellipses are larger for events located where the angular distribution of the stations around the epicentre is sparse as in the Sila Range and in the Ionian Calabrian Coast. Locations are characterized by a large number of events with root main square (rms) included in the 0.10–0.40 s range. Most part of these hypocenters show maximum horizontal errors (Max_Err_H) smaller than 2.0 km and vertical errors (Err_Z) smaller than 3.0 km (Fig. 5.3). These results outline the high quality of my database.

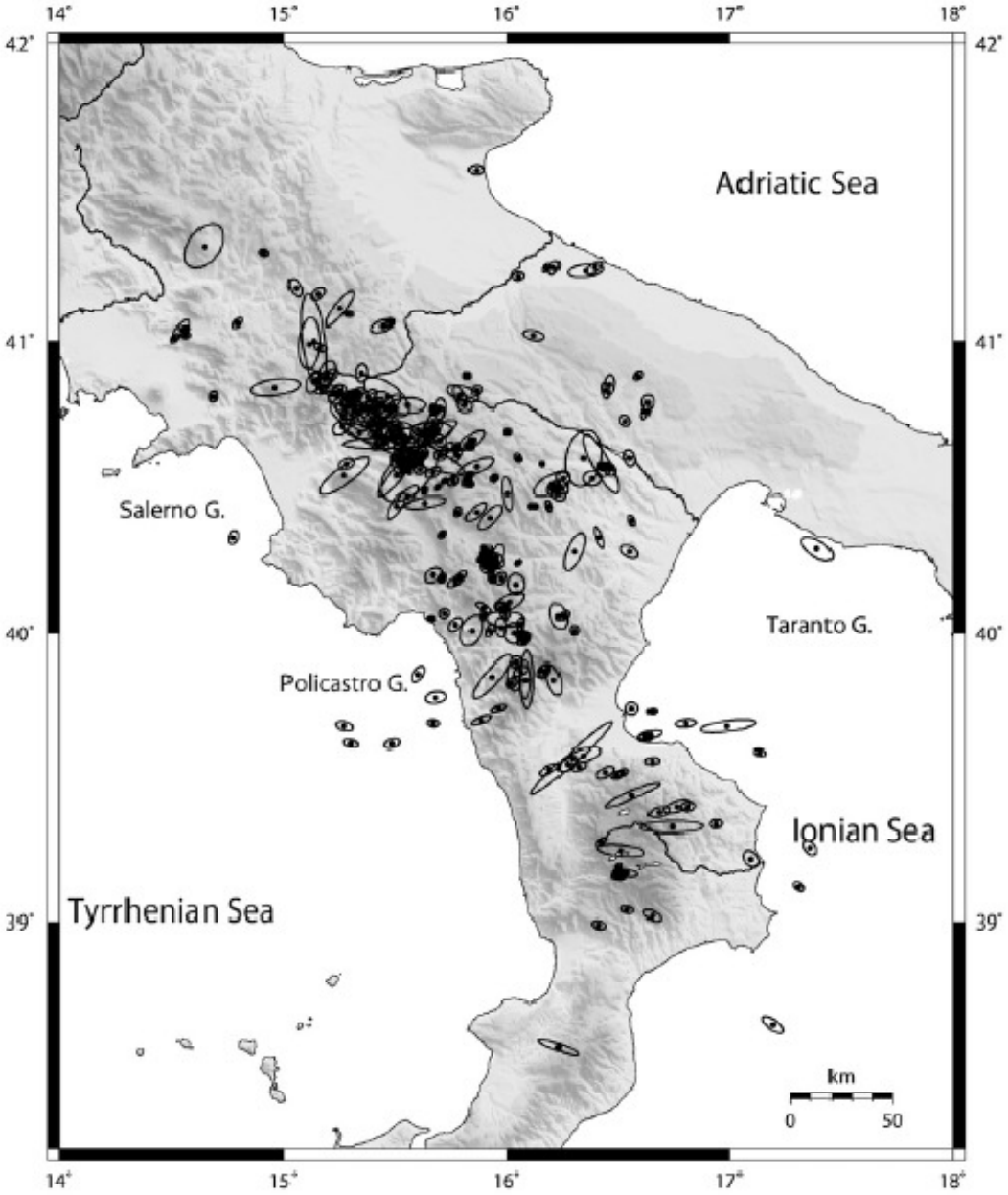

Figure 5.2: Earthquake locations and error ellipses (99% confidence limit): events with quality A, B and C (from Maggi et al., 2009).

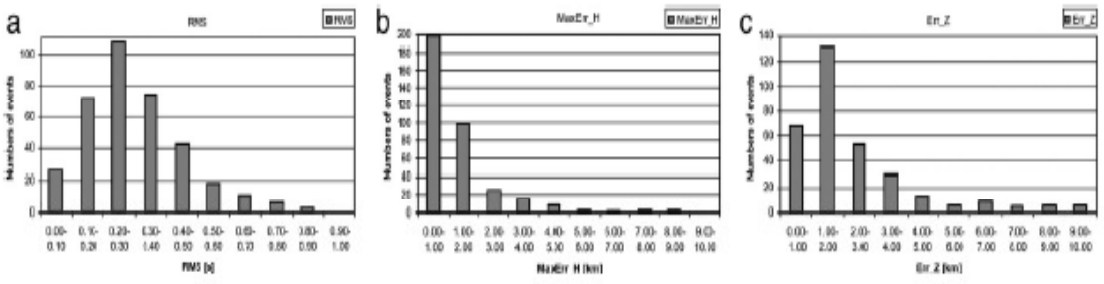

Figure 5.3: Distribution of: a) rms; b) maximum horizontal error (Max_Err_H) and c) vertical error (Err_Z) for relocated events. In b) and c) I considered only events with horizontal and vertical errors less than 10 km (from Maggi et al., 2009).

5.2 Focal mechanisms and stress tensor inversion (first dataset)

I computed 108 first-motion focal mechanisms, for the best located earthquakes (with quality A, B and C see Table 4.2) by using the P-waves first motion polarity method and the FPFIT code (Reasenberg and Oppenheimer, 1985) (for more details, see Appendix C). The dataset consists of fault plain solutions with a minimum number of eight observations. From this database I selected 58 fault plane solutions using with the two output quality factors Q_f and Q_p ranging from A to C for decreasing quality (Table 5.1).

Quality	Q_f	Q_p
A	$F_j \leq 0.025$	$\Delta s, \Delta d, \Delta r \leq 20°$
B	$0.025 < F_j \leq 0.1$	20° to 40°
C	$F_j > 0.1$	> 40°

Table 5.1: Value of quality factor Q_f and Q_p for Fault-plane solution. F_j =0 indicate a perfect fit to the data, while F_j =1 is a perfect misfit. Δs, Δd and Δr are ranges of perturbation of strike, dip and rake, respectively.

Q_f gives information about the solution misfit of the polarity data F_j, while Q_p reflects the solution uniqueness in terms of 90% confidence region on strike, dip and rake. The selected focal mechanisms for which A-A, A-B, B-A and B-B quality factors were obtained are relatively well constrained (Table 5.1, Fig. 5.4a and b). The focal mechanisms with quality A-

A are 31, and those with A-B and B-A are 27 (Table 5.2). All fault plane solutions with quality C for one of the two quality factors were rejected. The average number of polarities per event used in this study is 13. As shown from focal mechanisms of larger events, even from fault plane solutions of background seismicity I observe a widespread NE–SW extension in the Lucanian Apennine. The focal mechanisms computed in this work are in large part normal and strike-slip solutions and their tensional axes (T-axes) have a generalized NE–SW orientation.

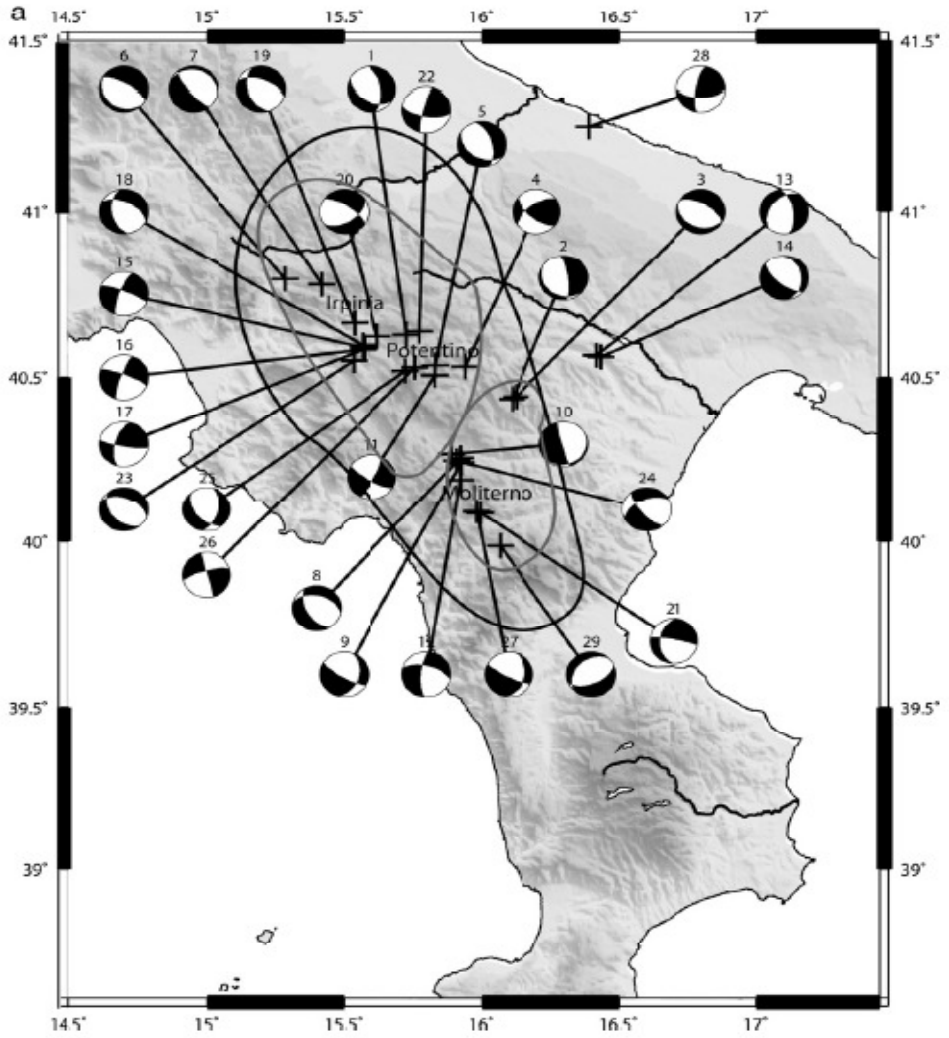

Figure 5.4: a, b. Location of the 58 selected fault plane solutions. Event numbers of Table 5.2 are shown close to each focal mechanism. Coloured lines encircle the crustal volume considered for the stress inversion: black line for the inversion with 49 fault plane solutions; grey lines for the two inversions of the Irpinia–Potentino area to the North (28 events) and the Moliterno-North-western Pollino area to the south (21 events) (from Maggi et al., 2009).

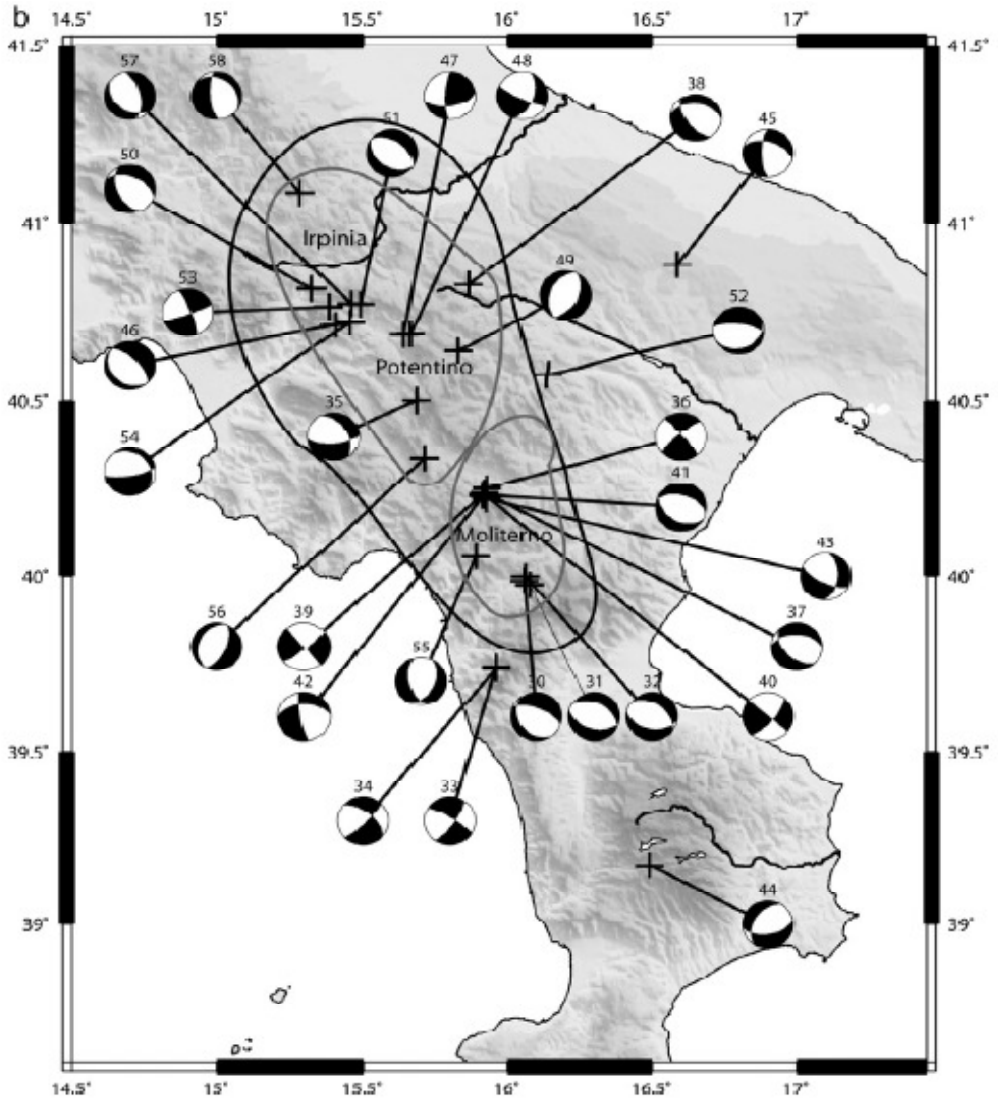

Figure 5.4: (continued)

No.	Date	O.T.	Latitude	Longitude	Depth	M_L	rms	ERH	ERZ	strike	Dip	Rake	Q_f	Q_p	N. P.	Category	Area
1	010914	08:02	40° 37.64	15° 43.67	20.81	2.4	0.38	0.8	0.7	120	45	−130	A	A	11	NF	Potentino
2	011104	10:22	40° 26.10	16° 06.65	12.32	2.1	0.62	0.4	1.0	130	20	−130	A	A	11	NF	Dolomiti Lucane
3	011104	10:28	40° 26.45	16° 07.53	14.19	2.3	0.60	0.3	1.1	110	30	−100	B	A	16	NF	Dolomiti Lucane
4	011113	13:21	40° 31.93	15° 56.46	36.15	1.9	0.79	0.5	0.8	130	65	150	A	A	13	SS	Potentino
5	011121	06:21	40° 32.14	15° 49.99	13.11	2.3	0.26	0.4	1.2	125	40	−120	A	B	12	NF	Potentino
6	011209	12:15	40° 47.72	15° 17.23	16.63	3.3	0.31	0.5	1.0	130	20	−80	B	A	15	NF	Irpinia
7	020102	02:17	40° 46.72	15° 25.04	15.40	2.8	0.23	0.6	1.5	140	75	−80	A	A	9	NF	Irpinia
8	020208	04:38	40° 15.45	15° 55.48	11.24	2.2	0.19	0.5	3.3	150	55	−60	A	A	10	NF	Moliterno
9	020226	17:12	40° 14.52	15° 55.59	5.45	2.1	0.29	0.3	0.8	15	40	−20	A	A	9	U	Moliterno
10	020402	04:22	40° 16.15	15° 53.45	13.70	2.7	0.66	0.4	1.3	165	85	−100	A	A	14	U	Moliterno
11	020413	08:44	40° 30.32	15° 49.80	13.12	2.4	0.30	0.4	1.3	120	75	−170	A	A	13	SS	Potentino
12	020413	10:48	40° 11.39	15° 55.51	12.36	2.1	0.21	0.5	1.1	285	60	−160	A	B	8	SS	Moliterno
13	020413	17:04	40° 33.91	16° 25.11	29.33	3.0	0.40	0.4	0.8	350	60	−120	A	A	32	NF	Basentano
14	020413	20:28	40° 33.60	16° 26.07	28.87	2.1	0.25	0.9	3.4	130	65	−110	A	B	8	NF	Basentano
15	020418	21:00	40° 35.30	15° 34.13	10.28	3.0	0.28	0.4	0.5	200	75	−10	A	B	17	SS	Savoia di Lucania
16	020418	21:36	40° 34.96	15° 34.39	9.60	2.2	0.24	0.6	0.5	200	80	−10	A	B	13	SS	Savoia di Lucania
17	020418	22:58	40° 35.00	15° 34.23	9.47	2.7	0.29	0.4	0.5	100	80	150	A	B	12	SS	Savoia di Lucania
18	020419	18:06	40° 35.72	15° 34.05	6.00	2.5	0.24	0.6	2.9	170	50	−50	A	A	10	NF	Savoia di Lucania
19	020504	09:41	40° 39.65	15° 32.20	15.77	2.3	0.39	0.4	1.1	160	45	−50	B	A	11	NF	Irpinia
20	020505	06:40	40° 37.31	15° 37.32	215.8	1.9	0.24	0.6	0.9	155	50	−150	A	A	8	NS	Irpinia
21	020508	19:29	40° 05.32	15° 59.62	14.50	2.9	0.29	0.4	1.1	280	85	−130	B	A	21	U	Northern Pollino
22	020512	20:20	40° 38.15	15° 46.51	18.47	2.1	0.32	0.4	1.0	100	65	170	A	B	11	SS	Potentino
23	020526	10:19	40° 32.96	15° 32.02	113.8	2.6	0.30	0.5	1.4	140	45	−70	A	A	8	NF	Vallo di Diano
24	020531	16:31	40° 14.93	15° 54.59	10.38	2.5	0.20	0.4	0.5	140	70	−40	B	A	13	NS	Moliterno
25	020611	20:02	40° 31.13	15° 43.45	13.97	2.1	0.45	0.3	0.6	140	50	−130	B	A	19	NF	Potentino
26	020618	23:31	40° 31.73	15° 45.47	10.97	2.3	0.37	0.3	0.5	255	75	0	A	A	19	SS	Potentino
27	020621	19:34	40° 05.56	15° 58.90	10.55	2.4	0.42	0.4	0.6	10	35	−20	B	A	13	U	Northern Pollino
28	020623	21:41	41° 15.02	16° 23.52	22.65	2.8	0.29	0.9	1.0	90	60	160	A	A	10	SS	Murge
29	020712	11:12	39° 59.24	16° 04.04	16.16	3.2	0.31	0.6	2.7	65	55	−80	A	A	13	NF	Northern Pollino
30	020713	05:57	39° 59.24	16° 03.42	9.22	2.1	0.47	0.4	0.7	145	30	−60	A	A	11	NF	Northern Pollino
31	020713	11:49	39° 58.52	16° 04.54	13.65	2.7	0.35	0.6	3.8	105	45	−100	A	A	8	NF	Northern Pollino
32	020718	08:28	39° 59.94	16° 03.61	9.01	2.5	0.46	0.4	0.7	100	45	−110	A	A	9	NF	Northern Pollino
33	020815	12:58	39° 44.47	15° 57.67	35.26	2.1	0.66	0.7	0.8	35	75	−170	A	B	12	SS	Orsomarso
34	020815	14:37	39° 44.16	15° 57.61	34.21	3.0	0.60	0.6	0.7	45	80	−150	B	A	20	SS	Orsomarso
35	020903	01:45	40° 30.11	15° 41.12	14.82	1.9	0.35	0.4	0.5	85	65	−130	B	A	16	NF	Potentino
36	021004	22:58	40° 15.13	15° 55.71	10.83	2.9	0.32	0.5	0.4	320	85	10	A	A	18	SS	Moliterno
37	021006	02:43	40° 14.41	15° 55.23	10.48	1.9	0.21	0.5	0.6	135	50	−60	A	A	12	NF	Moliterno
38	021109	01:53	40° 49.70	15° 51.78	13.52	2.0	0.25	0.6	1.9	145	60	−60	A	A	8	NF	Potentino
39	021119	16:53	40° 14.25	15° 55.05	8.98	1.8	0.19	0.5	1.1	50	80	0	A	A	10	SS	Moliterno
40	021129	10:54	40° 14.12	15° 55.04	10.50	1.9	0.22	0.5	0.9	40	70	0	A	A	9	SS	Moliterno
41	021130	01:19	40° 14.03	15° 54.69	10.57	2.4	0.23	0.4	0.6	120	40	−80	A	A	14	NF	Moliterno
42	021130	17:33	40° 13.84	15° 54.97	11.31	2.2	0.18	0.5	1.1	170	80	−40	B	A	13	SS	Moliterno
43	021201	00:30	40° 13.34	15° 55.54	7.58	2.1	0.28	0.3	0.8	5	50	−30	B	A	11	NS	Moliterno
44	021209	10:38	39° 10.24	16° 29.42	16.55	3.3	0.43	0.5	1.9	80	55	−60	B	A	14	NF	La Sila
45	030311	00:22	40° 53.06	16° 35.14	37.17	2.9	0.40	0.6	1.2	180	70	−40	B	A	16	NS	Murge
46	040224	05:21	40° 42.91	15° 24.39	16.51	3.8	0.26	0.7	1.5	135	25	−90	A	A	13	NF	Irpinia
47	040903	00:04	40° 41.25	15° 38.43	219.1	4.1	0.74	0.6	0.6	80	55	160	B	A	24	SS	Potentino
48	040903	01:22	40° 41.27	15° 39.87	10.75	2.8	0.24	0.7	0.7	20	55	−10	A	A	9	SS	Potentino
49	060107	04:27	40° 38.51	15° 49.77	17.21	2.3	0.23	0.5	2.2	25	50	−90	A	A	10	NF	Potentino
50	060314	03:15	40° 49.07	15° 19.58	10.46	2.7	0.29	0.4	0.6	155	50	−60	A	A	9	NF	Irpinia
51	060717	16:56	40° 46.46	15° 29.41	8.35	2.5	0.36	0.4	0.7	125	40	−90	A	B	9	NF	Irpinia
52	060907	15:31	40° 35.00	16° 09.53	30.70	3.9	0.41	0.3	0.6	65	25	−120	B	A	23	NF	Basentano
53	060915	17:55	40° 45.96	15° 23.03	16.17	2.4	0.17	0.6	1.6	70	85	−170	A	A	10	SS	Irpinia
54	060926	16:29	40° 43.32	15° 27.30	7.84	3.0	0.28	0.3	0.6	80	75	−110	B	A	15	NF	Irpinia
55	061022	00:38	40° 03.57	15° 53.35	16.98	2.4	0.25	0.6	1.1	25	45	−60	A	B	9	NF	Northern Pollino
56	061115	15:08	40° 20.24	15° 42.69	12.59	2.7	0.24	0.5	1.0	25	60	−90	A	A	10	NF	Vallo di Diano
57	061201	15:38	40° 46.48	15° 27.62	15.00	2.7	0.21	0.4	1.3	130	40	−120	A	A	12	NF	Irpinia
58	061205	06:20	41° 05.26	15° 17.29	16.73	2.5	0.41	0.5	1.1	175	70	−70	B	A	10	NF	Northern Irpinia

Table 5.2: Selected Southern Italy fault plane solutions Date in format year-month-day; O.T=origin time (hour and minute); Latitude north and Longitude east; Depth in km; ML=local magnitude of events belonging to the 2001–2002 period from the Italian Seismic Catalogue (CSI) and of 2003–2006 period from INGV Seismic Bulletin; rms=root mean square of residuals of locations; ERH and ERZ=horizontal and vertical location errors; strike, dip and rake of the first nodal plane; Qf and Qp=focal mechanism quality factors based on misfit and confidence regions; N.P.=polarities number; category=fault plane solution type (SS=strike-slip, NS=normal fault with small strike-slip component, NF=normal fault, U=undefined solution category); Area=geographical locality of event epicenter (from Maggi et al., 2009).

I applied the Gephart and Forsyth (1984) procedure, which was further implemented by Gephart (1990) (see Appendix D), to invert the focal mechanisms for the principal stress axes (σ_1, σ_2, σ_3) and the dimensionless parameter R (defined in equation 5.1) that describes the relative magnitudes of the intermediate principal stresses and hence constrains the shape of the deviatoric part of the stress tensor.

$$R = \frac{(\sigma_2 - \sigma_1)}{(\sigma_3 - \sigma_1)} \qquad 5.1$$

The inverse method using focal mechanism data cannot determine the absolute magnitude of the deviatoric and isotropic stresses. It only can identify the best stress tensor model that most closely matches all the fault plane solutions of the source region. The method requires the basic assumptions that the stress is uniform in space and time in the investigated volume. The brittle shallow crust would include small pre-existing faults of any orientation that may have low frictional coefficients. Earthquakes are shear dislocations on these pre-existing faults and slip occurs in the direction of the resolved shear stress on the fault plane. Discrepancy between stress tensor orientation and an observation is defined by a misfit measure which is given by the angular difference between the observed slip direction on a fault plane and the shear stress on that fault plane derived from a given stress tensor. Misfit is computed through an angular rotation about an axis for both nodal planes of each focal mechanism on a grid search of stress tensors. The stress tensor orientation that provides the average minimum misfit is assumed to be the best stress tensor for a given population of focal mechanisms (Maggi et al., 2009). I excluded from the inversion procedure 9 focal mechanisms, out of the 58 best selected fault plane solutions, which do not belong to the shallower crustal seismicity (depth smaller than 30 km) located within the Apenninic chain. This allows me to define the boundary of smaller crustal volumes approaching better the assumption of the uniform spatial stress field. I performed first an inversion with 49 focal mechanisms, all located inside the Apenninic chain from the northern Pollino Range to the northern Irpinia area. The minimum average misfit is 7.7°, corresponding to a stress tensor with a horizontal σ_3 (plunge 4°) NE–SW directed, an NW–SE oriented σ_2 (plunge 43°) and a σ_1 (plunge 47°) (Fig. 5.5a). The 95% confidence intervals of the principal stress axes do not overlap, suggesting that the three axes are well constrained by the data. The stress ratio R near the solution is 0.7 denoting that σ_2 is slightly close in its absolute value to σ_3. Notwithstanding the good results in agreement with

previous studies showing the general extension in a NE–SW direction of this part of the Apennine chain, large misfits suggest an inhomogeneous stress distribution within the considered crustal volume (Wyss et al., 1992). For this reason I performed two further inversions dividing the dataset into two sub-volumes (see Fig. 5.4a and b): one to the north, including the Irpinia and Potentino areas with 28 focal mechanisms, and the other to the South, including the Moliterno–Val d'Agri and the North-western Pollino Range with 21 fault plane solutions. In the Irpinia–Potentino the shape factor parameter R is between 0.4 and 0.5, while the misfit is 7.0°, suggesting a more homogenous stress field in this area. The minimum stress axis (σ_3) is sub-horizontal (plunge 14°) and NE–SW oriented and σ_1 is quite close to the vertical (75° of plunge) (Fig. 5.5b). The inversion results for the Moliterno–Val d'Agri area and the North-western Pollino range show a stress tensor with an orientation very similar to that obtained by using the whole dataset. The σ_3 axis is NE–SW directed with 3° of plunge, while σ_1 is sub-vertical (58° of plunge) and NW–SE oriented (Fig. 5.5c). Also here the R ratio is around 0.5, suggesting that the three principal stress axes are well separated in their absolute values. Moreover, the average misfit (6.0°) shows that the stress heterogeneities, inside the Southern sector, are smaller than in the previous area (Maggi et al., 2009).

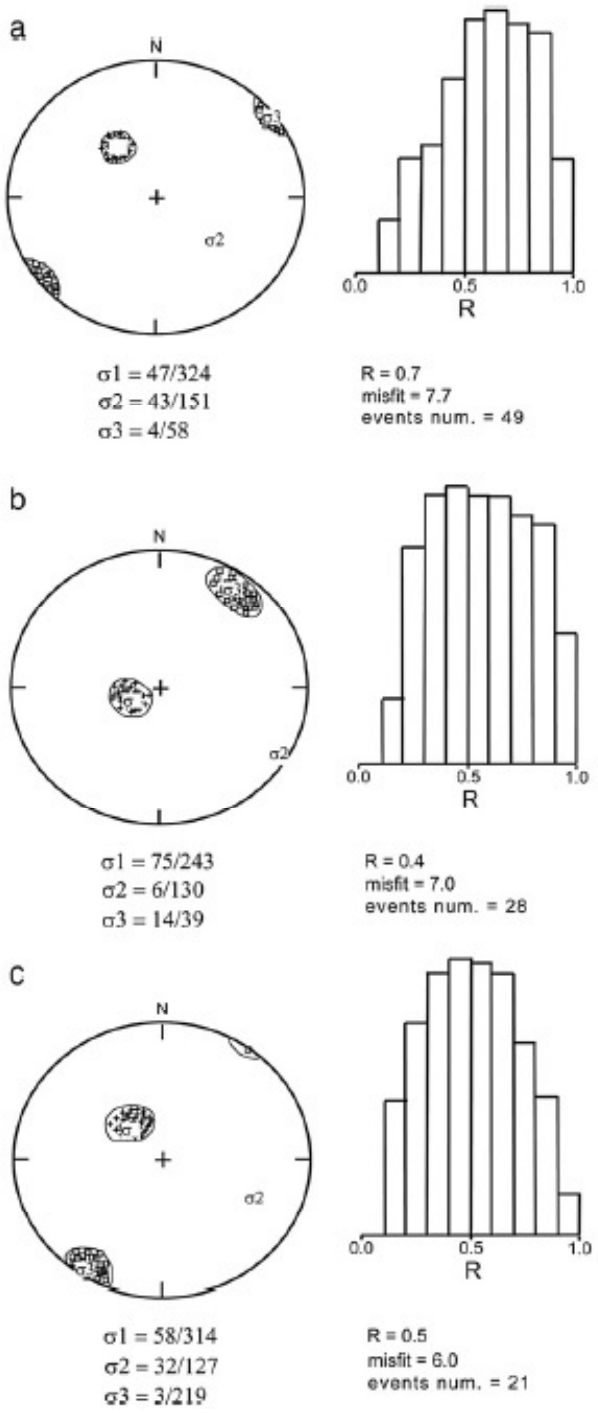

Figure 5.5: Stress inversion results using: a) 49 solutions (Apenninic chain); b) 28 solutions (Irpinia–Potentino); c) 21 solutions (Moliterno–Pollino). For each inversion is shown the stereonet plot with the 95% confidence limits for σ_1 (small crosses) and σ_3 (small squares) and the histogram illustrating the uncertainty in the dimensionless parameter R . Plunge and trend for the three principal stress axes are shown below the stereonets (from Maggi et al., 2009).

5.3 Earthquakes relocation (incremented dataset)

SeSCAL array has operated in the period between December 2007 and December 2008 and I incremented my database with these new data and RSNC data (see Chapter 3). Using this dataset and the 1D velocity model computed for the studied area, I relocated 677 events with the HYPOELLIPSE code. I selected 566 hypocentral solutions removing those with horizontal and vertical errors larger than 5.35 km (quality D; see Table 4.2), azimuthal gap > 180◦ and the rms of the solution travel-time residuals larger than 1.0 s. The average rms results equal to 0.22 s. Most of the relocated earthquakes show rms values between 0.10 and 0.40 s, maximum horizontal errors smaller than 2.0 km and vertical errors smaller than 3.0 km (Fig. 5.6). Figure 5.6d, e show the *P* and *S* residual histograms. P-phase residuals versus frequency are a Gaussian distribution centred on zero and are consistent with P-picking accuracy and the computed 1D velocity model. Instead, the plot of S-phase residuals versus frequency doesn't show a Gaussian distribution centred on zero. Probably it is due to a low S-velocity used in the model, and therefore to a slightly high value of $^{V_P}/_{V_S}$ ratio.

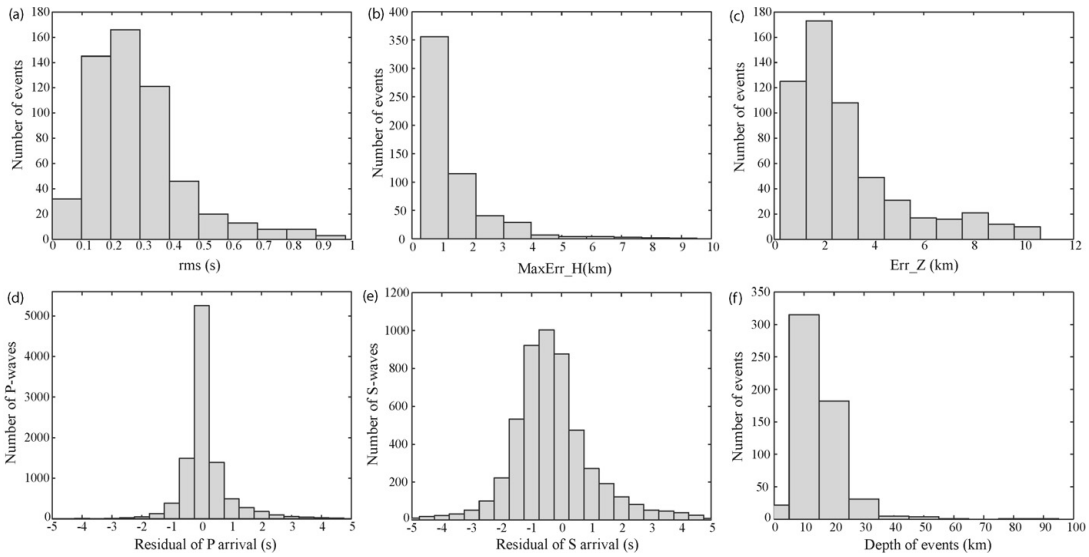

Figure 5.6: Histograms showing the root mean square (rms) of the solution travel-time residuals (a), horizontal (b) and vertical (c) errors, P-phase (d) and S-phase (e) residuals versus frequency obtained from the location procedure. Number of events for different depth ranges (f) (from Frepoli et al., 2011).

Fig. 5.7a shows the distribution of the background seismicity investigated in this study. Hypocentral depths range from 5.0 to 92 km, with the majority of solutions between 5 and 30

km (Fig. 5.7b, c). Fig. 5.8 shows the error ellipses with the 99% confidence limits of the relocated earthquakes. I observed that the seismicity distribution is concentrated in the area of the Southern Apennine belt from the Irpinia region to the Pollino Range (Fig. 5.7a), with foci up to about 25 km depth. Within this region, the seismicity is concentrated in the Irpinia–Potentino area, and, more to the South, in the Moliterno–Castelluccio–Lauria area. Moreover, I observe a rarefaction of events, with only a small cluster close to the locality of Upper Val d'Agri. Moving from the Lucanian Apennines toward the Bradano foredeep, I recognize two seismic clusters that appear elongated in a W–E direction. The first and smaller cluster (15–25 km of hypocentral depth) is located in the Potentino sector at S-W of the two seismic sequences of 1990 and 1991 (Azzara et al., 1993; Alessio et al., 1995). The second one, in the named Abriola–Pietrapertosa sector, is located at Northern Upper Val D'Agri and elongated more to the east reaching the Bradano foredeep with hypocentral depths between 15 and 40 km (Fig. 5.7b, cross-sections EF, GH). This result is very attractive as it shows a seismogenic layer which deepens to more than 30 km, following the flexure of the Adriatic subducting lithosphere. In the area at South of Pollino Range I observe a seismic gap, which separates the Lucanian Apennine seismogenic domain from the NE elongated seismic zone to the sparse seismicity of the Sila Plateau, Crati Valley and Taranto Gulf (Fig. 5.7a). The Taranto Gulf offshore seismicity is characterized by deeper foci (between 15 and 35 km) and appears clustered in the middle of the gulf (Fig. 5.7). The Bradano foredeep and the Apulia foreland are characterized by a more sparse seismicity which shows larger hypocentral depths (Fig. 5.7a). To the north, beneath the Tavoliere, my relocations show hypocentral depths between 5 and 20 km (Fig. 5.7b, cross-section AB; Fig. 5.7c, cross-section OP), as previously observed by Del Gaudio et al. (2007). It is interesting to note the few events with depth between 20 and 35 km below the area hit by the 1560 Barletta-Bisceglie earthquake (Fig. 5.7b, cross-sections CD and OP). The Murge area seems to be aseismic with the exception of the central portion characterized by both shallow (around 5–10 km) and deep lower crust (20–40 km) earthquakes (Fig. 5.7b, cross-section GH; Fig. 5.7c, OP).

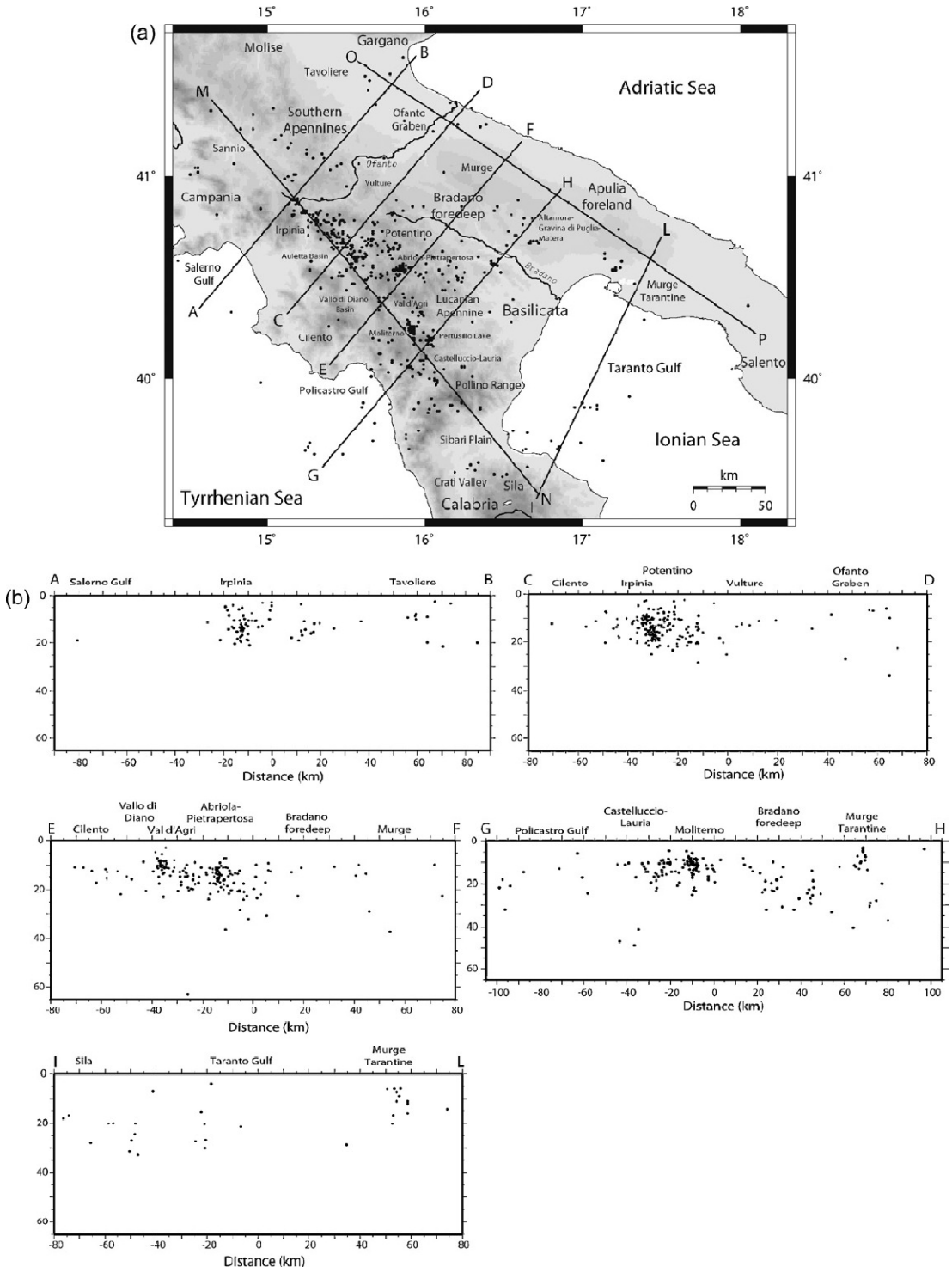

Fig. 5.7: (a) Map distribution of the 566 selected earthquakes (HYPOELLIPSE quality A, B and C); (b) cross-sections AB, CD, EF, GH and IL; (c) cross-sections MN and OP. Width of cross-sections AB, CD, EF, and GH is 25 km, while for cross-sections IL, MN and OP is 30 km (from Frepoli et al., 2011).

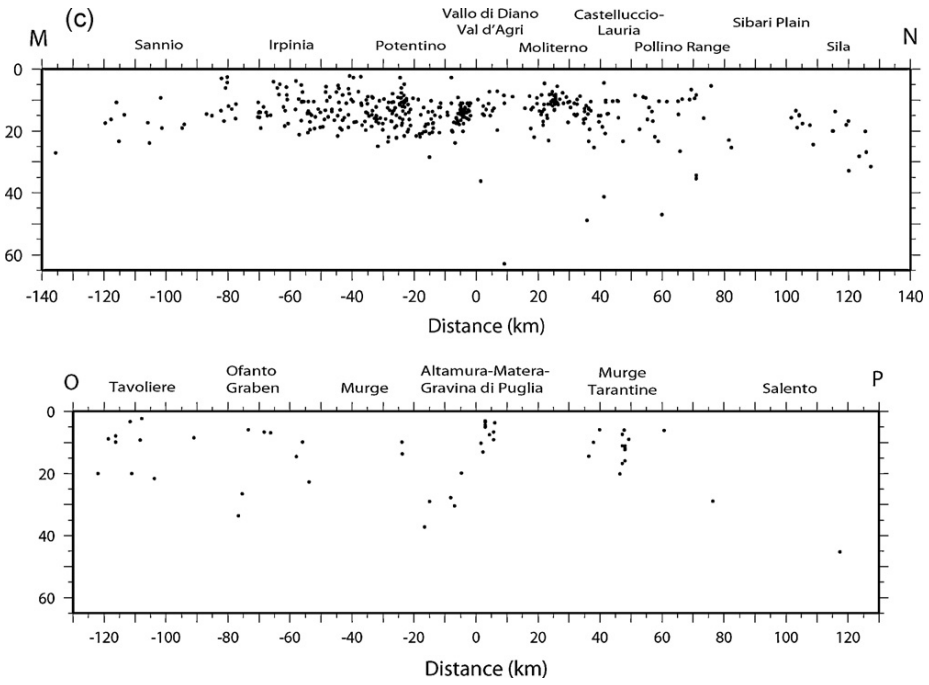

Fig. 5.7 (Continued).

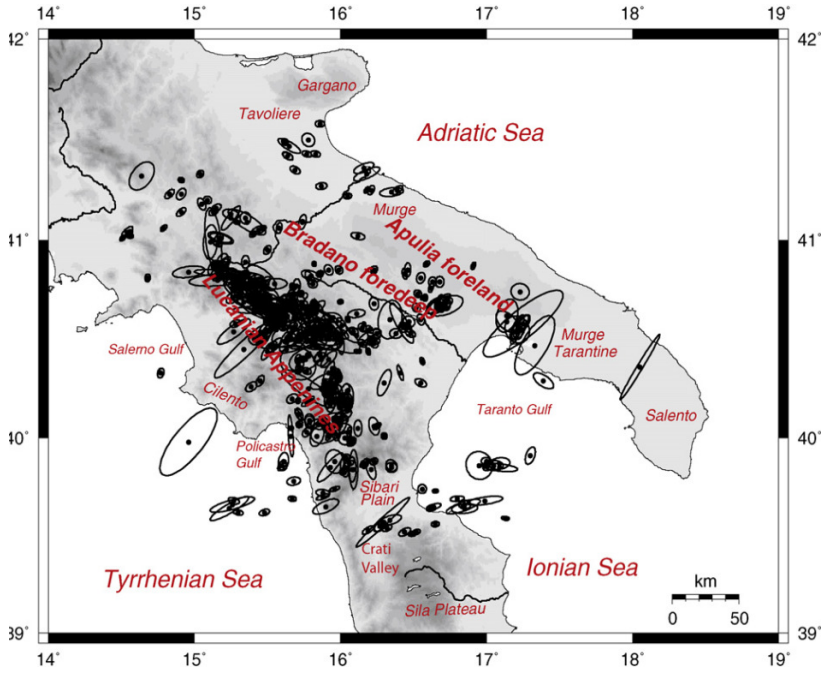

Figure 5.8: Map distribution of the 566 selected events and error ellipses (99% confidence limit) (from Frepoli et al., 2011).

Some low-magnitude earthquakes are also recorded in the Murge Tarantine area with depth between 5 and 20km (Fig. 5.7b, cross-section IL; Fig. 5.7c, cross-section OP). The almost aseismic Salento peninsula shows only two deep crustal earthquakes located at 30 and 40 km, respectively (Fig. 5.7c, cross-section OP) (Frepoli et al., 2011).

5.4 Focal mechanisms and stress tensor inversion (incremented dataset)

I computed focal mechanisms for the best located earthquakes using the FPFIT code (for more details, see Appendix C). The dataset consists of 162 fault-plane solutions with a minimum number of eight (8) observations. From this dataset, I selected 102 focal mechanisms with the two output quality factors Q_f and Q_p of the FPFIT code, ranging from A to C for decreasing quality (Table 5.1).

All fault-plane solutions having Q_f or Q_p equal to C were rejected. The 102 selected focal mechanisms for which A–A, A–B, B–A and B–B quality factors are obtained, are relatively well constrained (Table 5.3, Fig. 5.9).

Focal mechanisms with quality A–A are 51, those with A–B and B–A are 48 and those with quality B–B are only 3. the average number of polarities per event used in this study is 13. By examining the plunge of the P- and T-axes I observe that around 57% of the focal solutions show normal faulting mechanisms whereas 28% are pure strike-slip. The other solutions show transtensional kinematics. T-axes for most of the solutions are sub-horizontal (plunge < 30◦) with an average anti-Apenninic trend (N45◦), whereas P-axes have an average plunge of 60–70◦ and trend mainly between 120◦ and 150◦ (Fig. 5.10).

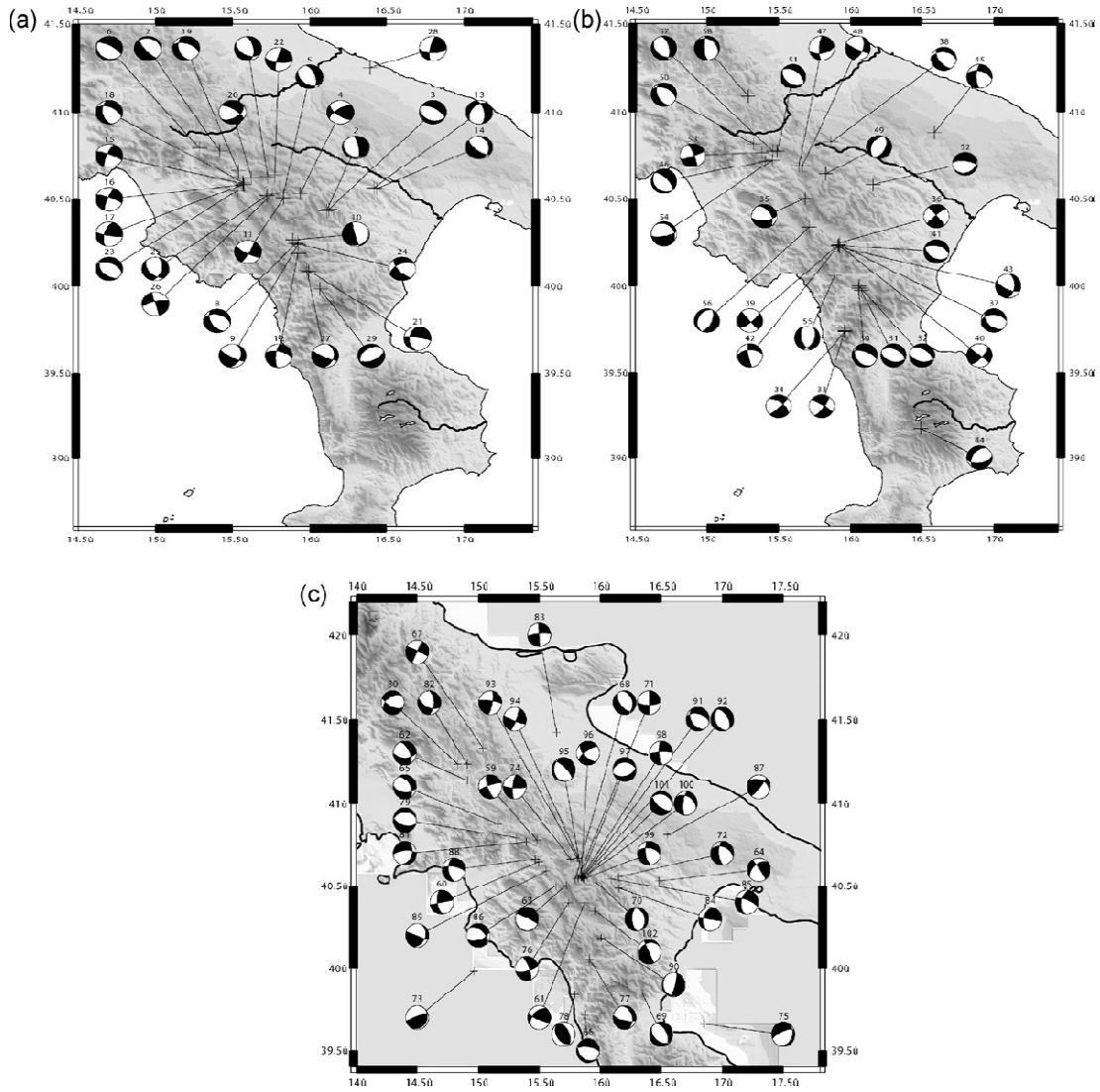

Figure 5.9: Focal mechanisms of 162 selected fault-plane solutions. Event numbers of Table 5.3 are shown close to each focal mechanism (from Frepoli et al. 2011).

No.	Date	O.T.	Latitude	Longitude	Depth	M_L	r.m.s.	ERH	ERZ	Strike	Dip	Rake	Q_f	Q_p	N. P.	Category	Area
1	010914	08:02	40° 37.64	15° 43.67	20.81	2.4	0.38	0.8	0.7	120	45	−130	A	A	11	NF	Potentino
2	011104	10:22	40° 26.10	16° 06.65	12.32	2.1	0.62	0.4	1.0	130	20	−130	A	A	11	NF	Dolomiti Lucane
3	011104	10:28	40° 26.45	16° 07.53	14.19	2.3	0.60	0.3	1.1	110	30	−100	B	A	16	NF	Dolomiti Lucane
4	011113	13:21	40° 31.93	15° 56.46	36.15	1.9	0.79	0.5	0.8	130	65	150	A	A	13	SS	Potentino
5	011121	06:21	40° 32.14	15° 49.99	13.11	2.3	0.26	0.4	1.2	125	40	−120	A	B	12	NF	Potentino
6	011209	12:15	40° 47.72	15° 17.23	16.63	3.3	0.31	0.5	1.0	130	20	−80	B	A	15	NF	Irpinia
7	020102	02:17	40° 46.72	15° 25.04	15.40	2.8	0.23	0.6	1.5	140	75	−80	A	A	9	NF	Irpinia
8	020208	04:38	40° 15.45	15° 55.48	11.24	2.2	0.19	0.5	3.3	150	55	−60	A	A	10	NF	Moliterno
9	020226	17:12	40° 14.52	15° 55.59	5.45	2.1	0.29	0.3	0.8	15	40	−20	A	A	9	U	Moliterno
10	020402	04:22	40° 16.15	15° 53.45	13.70	2.7	0.66	0.4	1.3	165	85	−100	A	A	14	U	Moliterno
11	020413	08:44	40° 30.32	15° 49.80	13.12	2.4	0.30	0.4	1.3	120	75	−170	A	A	13	SS	Potentino
12	020413	10:48	40° 11.39	15° 55.51	12.36	2.1	0.21	0.5	1.1	285	60	−160	A	B	8	SS	Moliterno
13	020413	17:04	40° 33.91	16° 25.11	29.33	3.0	0.40	0.4	0.8	350	60	−120	A	A	32	NF	Basentano
14	020413	20:28	40° 33.60	16° 26.07	28.87	2.1	0.25	0.9	3.4	130	65	−110	A	B	8	NF	Basentano
15	020418	21:00	40° 35.30	15° 34.13	10.28	3.0	0.28	0.4	0.5	200	75	−10	A	B	17	SS	Savoia di Lucania
16	020418	21:36	40° 34.96	15° 34.39	9.60	2.2	0.24	0.6	0.5	200	80	−10	A	B	13	SS	Savoia di Lucania
17	020418	22:58	40° 35.00	15° 34.23	9.47	2.7	0.29	0.4	0.5	100	80	150	A	B	12	SS	Savoia di Lucania
18	020419	18:06	40° 35.72	15° 34.05	6.00	2.5	0.24	0.6	2.9	170	50	−50	A	A	10	NF	Savoia di Lucania
19	020504	09:41	40° 39.65	15° 32.20	15.77	2.3	0.39	0.4	1.1	160	45	−50	B	A	11	NF	Irpinia
20	020505	06:40	40° 37.31	15° 37.32	21.58	1.9	0.24	0.6	0.9	155	50	−150	A	A	8	NS	Irpinia
21	020508	19:29	40° 05.32	15° 59.62	14.50	2.9	0.29	0.4	1.1	280	85	−130	B	A	21	U	Northern Pollino
22	020512	20:20	40° 38.15	15° 46.51	18.47	2.1	0.32	0.4	1.0	100	65	170	A	B	11	SS	Potentino
23	020526	10:19	40° 32.96	15° 32.02	11.38	2.6	0.30	0.5	1.4	140	45	−70	A	A	8	NF	Vallo di Diano
24	020531	16:31	40° 14.93	15° 54.59	10.38	2.5	0.20	0.4	0.5	140	70	−40	B	A	13	NS	Moliterno
25	020611	20:02	40° 31.13	15° 43.45	13.97	2.1	0.45	0.3	0.6	140	50	−130	B	A	19	NF	Potentino
26	020618	23:31	40° 31.73	15° 45.47	10.97	2.3	0.37	0.3	0.5	255	75	0	A	A	19	SS	Potentino
27	020621	19:34	40° 05.56	15° 58.90	10.55	2.4	0.42	0.4	0.6	10	35	−20	B	A	13	U	Northern Pollino
28	020623	21:41	41° 15.02	16° 23.52	22.65	2.8	0.29	0.9	1.0	90	60	160	A	A	10	SS	Murge
29	020712	11:12	39° 59.24	16° 04.04	16.16	3.2	0.31	0.6	2.7	65	55	−80	A	A	13	NF	Northern Pollino
30	020713	05:57	39° 59.24	16° 03.42	9.22	2.1	0.47	0.4	0.7	145	30	−60	A	A	11	NF	Northern Pollino
31	020713	11:49	39° 58.52	16° 04.54	13.65	2.7	0.35	0.6	3.8	105	45	−100	A	A	8	NF	Northern Pollino
32	020718	08:28	39° 59.94	16° 03.61	9.01	2.5	0.46	0.4	0.7	100	45	−110	A	A	9	NF	Northern Pollino
33	020815	12:58	39° 44.47	15° 57.67	35.26	2.1	0.66	0.7	0.8	35	75	−170	A	B	12	SS	Orsomarso
34	020815	14:37	39° 44.16	15° 57.61	34.21	3.0	0.60	0.6	0.7	45	80	−150	B	A	20	SS	Orsomarso
35	020903	01:45	40° 30.11	15° 41.12	14.82	1.9	0.35	0.4	0.5	85	65	−130	B	A	16	NF	Potentino
36	021004	22:58	40° 15.13	15° 55.71	10.83	2.9	0.32	0.5	0.4	320	85	10	A	A	18	SS	Moliterno
37	021006	02:43	40° 14.41	15° 55.23	10.48	1.9	0.21	0.5	0.6	135	50	−60	A	A	12	NF	Moliterno
38	021109	01:53	40° 49.70	15° 51.78	13.52	2.0	0.25	0.6	1.9	145	60	−60	A	A	8	NF	Potentino
39	021119	16:53	40° 14.25	15° 55.05	8.98	1.8	0.19	0.5	1.1	50	80	0	A	A	10	SS	Moliterno
40	021129	10:54	40° 14.12	15° 55.04	10.50	1.9	0.22	0.5	0.9	40	70	0	A	A	9	SS	Moliterno
41	021130	01:19	40° 14.03	15° 54.69	10.57	2.4	0.23	0.4	0.6	120	40	−80	A	A	14	NF	Moliterno
42	021130	17:33	40° 13.84	15° 54.97	11.31	2.2	0.18	0.5	1.1	170	80	−40	B	A	13	SS	Moliterno
43	021201	00:30	40° 13.34	15° 55.54	7.58	2.1	0.28	0.3	0.8	5	50	−30	B	A	11	NS	Moliterno
44	021209	10:38	39° 10.24	16° 29.42	16.55	3.3	0.43	0.5	1.9	80	55	−60	B	A	14	NF	La Sila
45	030311	00:22	40° 53.06	16° 35.14	37.17	2.9	0.40	0.6	1.2	180	70	−40	B	A	16	NS	Murge
46	040224	05:21	40° 42.91	15° 24.39	16.51	3.8	0.26	0.7	1.5	135	25	−90	A	A	13	NF	Irpinia
47	040903	00:04	40° 41.25	15° 38.43	21.91	4.1	0.74	0.6	0.6	80	55	160	B	A	24	SS	Potentino
48	040903	01:22	40° 41.27	15° 39.87	10.75	2.8	0.24	0.7	0.7	20	55	−10	A	A	9	SS	Potentino
49	060107	04:27	40° 38.51	15° 49.77	17.21	2.3	0.23	0.5	2.2	25	50	−90	A	A	10	NF	Potentino
50	060314	03:15	40° 49.07	15° 19.58	10.46	2.7	0.29	0.4	0.6	155	50	−60	A	A	9	NF	Irpinia
51	060717	16:56	40° 46.46	15° 29.41	8.35	2.5	0.36	0.4	0.7	125	40	−90	A	B	9	NF	Irpinia
52	060907	15:31	40° 35.00	16° 09.53	30.70	3.9	0.41	0.3	0.6	65	25	−120	B	A	23	NF	Basentano
53	060915	17:55	40° 45.96	15° 23.03	16.17	2.4	0.17	0.6	1.6	70	85	−170	A	A	10	SS	Irpinia
54	060926	16:29	40° 43.32	15° 27.30	7.84	3.0	0.28	0.3	0.6	80	75	−110	B	A	15	NF	Irpinia
55	061022	00:38	40° 03.57	15° 53.35	16.98	2.4	0.25	0.6	1.1	25	45	−60	A	B	9	NF	Northern Pollino
56	061115	15:08	40° 20.24	15° 42.69	12.59	2.7	0.24	0.5	1.0	25	60	−90	A	A	10	NF	Vallo di Diano
57	061201	15:38	40° 46.48	15° 27.62	15.00	2.7	0.21	0.4	1.3	130	40	−120	A	A	12	NF	Irpinia
58	061205	06:20	41° 05.26	15° 17.29	16.73	2.5	0.41	0.5	1.1	175	70	−70	B	A	10	NF	Northern Irpinia
59	070607	17:16	40° 46.67	15° 28.84	5.28	2.3	0.20	0.9	0.2	160	70	−10	B	B	8	SS	Muro Lucano
60	070618	05:38	40° 38.74	15° 29.74	15.01	2.0	0.11	0.5	0.2	80	90	150	A	B	8	SS	Balvano–Irpinia
61	070619	00:01	40° 23.93	15° 52.24	62.92	2.8	0.38	1.3	0.4	115	75	130	A	A	41	TS	Marsico Vetere
62	070620	07:08	41° 08.31	14° 54.79	17.29	2.1	0.12	0.5	0.3	90	55	−140	A	A	8	NF	Beneventano
63	070714	02:27	40° 30.19	15° 43.36	20.22	2.6	0.22	0.7	0.3	105	5	−100	A	A	15	U	Brienza
64	070720	00:57	40° 31.83	16° 28.84	26.64	1.9	0.32	0.6	0.2	325	85	−140	A	A	10	U	Ferrandina
65	071206	21:25	40° 52.61	15° 09.77	14.09	2.8	0.94	0.6	0.1	95	50	−130	A	A	8	NF	Lioni–Irpinia
66	071208	07:09	39° 43.11	15° 52.51	284.09	3.4	0.71	0.6	0.3	130	25	−60	B	A	29	U	Northern Calabria
67	071226	19:20	41° 19.83	15° 02.34	23.26	2.6	0.27	0.6	0.2	295	85	180	A	B	11	SS	Beneventano
68	080114	22:58	40° 32.61	15° 47.77	23.83	2.3	0.35	0.5	0.2	345	35	−70	B	A	10	NF	Abriola
69	080115	02:38	39° 51.07	16° 20.78	25.25	3.0	0.31	0.9	0.3	125	40	−110	A	B	10	NF	Civita–Pollino
70	080120	20:55	40° 31.25	15° 58.11	11.16	2.2	0.47	0.5	0.2	345	35	−100	A	A	14	NF	Anzi
71	080202	00:13	40° 33.02	15° 49.08	17.37	2.3	0.16	0.7	0.2	0	90	−20	A	A	12	SS	Abriola
72	080213	04:09	40° 33.43	16° 09.12	21.97	1.9	0.19	0.7	0.2	175	65	−50	B	B	10	NS	Pietrapertosa

Table 5.3: Selected fault-plane solutions. Date in format year-month-day; O.T. = origin time (hour and minute); latitude north and longitude east; depth in km; ML = local magnitude of events belonging to the 2001–2002 period from the Italian Seismic Catalogue (CSI) and belonging to the 2003–2008 period from INGV Seismic Bulletin; r.m.s. = root mean square of residuals; ERH and ERZ = horizontal and vertical location errors; strike, dip and rake of the first nodal plane; Qf and Qp = focal mechanism quality factors based on misfit and confidence regions; N.P. = polarities number; category = fault-plane solution type (SS = strike-slip, NS = normal fault with small strike-slip component, NF = normal fault, U= undefined solution category); area = geographical locality of event epicenter (from Frepoli et al. 2011).

No.	Date	O.T.	Latitude	Longitude	Depth	M_L	r.m.s.	ERH	ERZ	Strike	Dip	Rake	Q_f	Q_p	N. P.	Category	Area
73	080220	23:26	39° 58.84	14° 57.89	301.86	3.2	0.63	2.8	1.1	40	15	50	A	A	26	U	Southern Tyrrhen.
74	080225	05:42	40° 39.89	15° 45.56	21.58	1.8	0.26	0.7	0.2	185	75	10	B	A	13	SS	Potenza
75	080310	10:33	39° 39.63	16° 50.98	20.00	3.3	0.32	0.8	0.4	25	25	−130	B	A	18	NF	Taranto Gulf
76	080405	10:09	40° 23.92	15° 44.42	14.50	1.8	0.30	0.7	0.1	340	75	−20	A	B	10	SS	Marsico Nuovo
77	080413	22:26	40° 03.43	15° 54.73	18.54	2.4	0.30	0.7	0.3	105	70	−120	A	A	11	NF	Lauria–Polino
78	080520	22:56	39° 50.45	15° 47.54	227.49	3.4	0.21	4.3	1.2	140	40	80	A	B	29	TF	Northern Calabria
79	080527	16:19	40° 47.52	15° 18.82	14.12	2.7	0.45	0.6	0.2	105	55	−80	A	A	9	NF	Santomenna–Irpi.
80	080706	22:28	41° 13.92	14° 49.83	16.24	2.3	0.13	0.6	0.2	115	60	−50	A	A	10	NS	Beneventano
81	080810	12:35	40° 45.01	15° 23.68	5.65	2.3	0.40	0.5	0.3	20	40	−150	A	A	10	NS	Castelgrarde–Irp.
82	080811	02:52	41° 13.95	14° 54.54	14.67	2.2	0.24	0.8	0.3	115	55	−140	A	A	10	NS	Beneventano
83	080812	21:21	41° 25.19	15° 38.50	9.81	3.0	0.46	0.6	0.1	265	80	180	B	B	22	SS	Foggia
84	080813	05:58	40° 29.03	16° 09.17	23.99	2.6	0.32	0.6	0.2	100	85	130	A	B	9	U	Accettura
85	080815	01:45	40° 32.63	16° 05.46	32.00	1.7	0.22	0.9	0.2	290	75	−140	A	B	14	NS	Pietrapertosa
86	080907	20:43	40° 29.87	15° 38.15	20.43	2.0	0.28	0.6	0.2	70	60	−130	A	A	13	TF	Brienza
87	080925	20:27	40° 48.62	16° 32.98	28.99	2.4	0.39	0.8	0.2	40	80	50	A	A	9	TS	Altamura
88	081103	05:24	40° 39.93	15° 28.05	13.90	1.8	0.14	0.6	0.2	280	70	−140	A	B	8	NS	Balvano–Irpinia
89	081108	09:24	40° 35.47	15° 33.47	12.08	2.8	0.36	0.6	0.2	20	30	0	B	A	21	U	Sawoia di Lucania
90	081108	13:15	40° 11.12	16° 00.47	16.13	2.5	0.26	0.8	0.2	15	80	−80	A	A	9	U	Castelsaraceno
91	081112	19:31	40° 33.35	15° 51.45	14.42	2.4	0.36	0.5	0.2	145	45	−50	B	A	16	NF	Abriola
92	081114	01:59	40° 33.30	15° 51.49	14.13	2.8	0.31	0.5	0.2	150	40	−80	B	A	16	NF	Abriola
93	081114	20:44	40° 40.33	15° 48.75	20.68	2.9	0.31	0.6	0.1	10	75	10	A	A	21	SS	Potenza
94	081114	21:04	40° 40.31	15° 49.35	20.23	2.0	0.30	0.6	0.1	20	80	−10	A	B	9	SS	Potenza
95	081117	00:13	40° 33.47	15° 50.93	16.94	2.9	0.37	0.5	0.2	155	20	−50	B	A	17	NF	Abriola
96	081118	19:54	40° 33.45	15° 50.60	15.70	2.5	0.34	0.5	0.2	135	60	20	B	A	16	NS	Abriola
97	081118	20:05	40° 33.57	15° 50.65	15.97	2.9	0.34	0.5	0.2	75	50	−100	A	A	19	NF	Abriola
98	081118	22:14	40° 33.09	15° 50.78	16.51	2.4	0.31	0.5	0.2	175	75	−10	A	B	14	SS	Abriola
99	081120	21:00	40° 32.62	15° 51.91	14.07	2.2	0.30	0.7	0.2	170	65	−40	A	A	12	NS	Abriola
100	081127	16:52	40° 33.05	15° 51.65	15.16	2.0	0.32	0.7	0.2	300	40	−150	A	B	9	NS	Abriola
101	081127	23:49	40° 32.90	15° 51.66	12.94	2.2	0.35	0.6	0.2	130	65	−80	A	A	14	NF	Abriola
102	081225	18:55	40° 21.00	15° 57.23	19.13	2.7	0.32	0.5	0.1	245	90	50	A	A	12	U	Viggiano

Table 5.3: (continued)

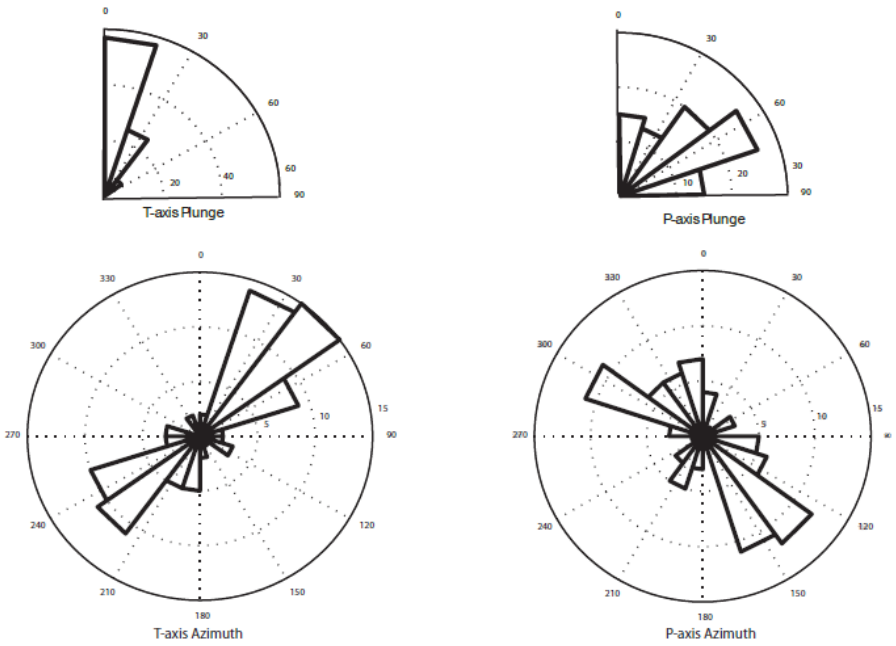

Figure 5.10: Rose diagrams showing P- and T-axes plunge and azimuth distribution (modified from Frepoli et al. 2011).

I computed the stress tensor inversion of the 102 selected fault-plane solutions applying the inversion technique proposed by Gephart and Forsyth (1984) and further implemented by Gephart (1990) (see Appendix D).

I performed the inversion by using only crustal seismicity (depth < 30 km) located and clustered beneath the Apenninic chain. For the surrounding areas (Bradano foredeep, Apulia foreland and peri-Tyrrhenian margin) I do not have a sufficient number of focal mechanisms to reliably apply the inversion method. This selection allows me to define the boundary of two smaller crustal volumes approaching better the assumption of the uniform spatial stress field. I performed a first inversion with 58 focal mechanisms located within the Apenninic chain from the Irpinia–Potentino area, to the NW, to the Abriola–Pietrapertosa sector, to the SE. The minimum average misfit is 8.0◦, corresponding to a stress tensor with a horizontal σ_3 (plunge 11◦) NE–SW directed, an NW–SE oriented σ_2 (plunge 12◦) and a σ_1 (plunge 73◦) (Fig. 5.11). The large value of misfit suggests an inhomogeneous stress distribution within the considered crustal volume (Wyss et al., 1992). The 95% confidence intervals of the principal stress axes are small, suggesting that the three axes are well constrained by the data. Stress ratio R near the solution is 0.5. This result is in agreement with the fault slip data of active faults available for the study area (Pantosti and Valensise, 1990; Hippolyte et al., 1995; Papanikolaou and Roberts, 2007) and with the regional stress field obtained previously by using moderate magnitude earthquakes (Frepoli and Amato, 2000; Frepoli et al., 2005; Maggi et al., 2009) and borehole breakouts (Montone et al., 1999; Cucci et al., 2004). I performed the second inversion in the area located to the south of the seismic gap of the Vallo di Diano–Upper Val d'Agri sector using the available 22 focal solutions of the Moliterno–Pollino Range sector. This inversion shows a dimensionless parameter R of 0.4 and a misfit value of 6.2◦. The minimum stress axis (σ_3) is sub-horizontal (plunge 5◦) and NE–SW oriented, σ_1 is quite close to the vertical (71◦ of plunge) and σ_2 is sub-horizontal (plunge 18◦) and NW–SE directed (Fig. 5.11). The two stress tensor inversions performed in this study show results very similar suggesting that the whole Southern Apennines, from Irpinia to the Pollino Range, is characterized by an almost horizontal and NE-trending σ_3 and sub-vertical σ_1 (Frepoli et al., 2011).

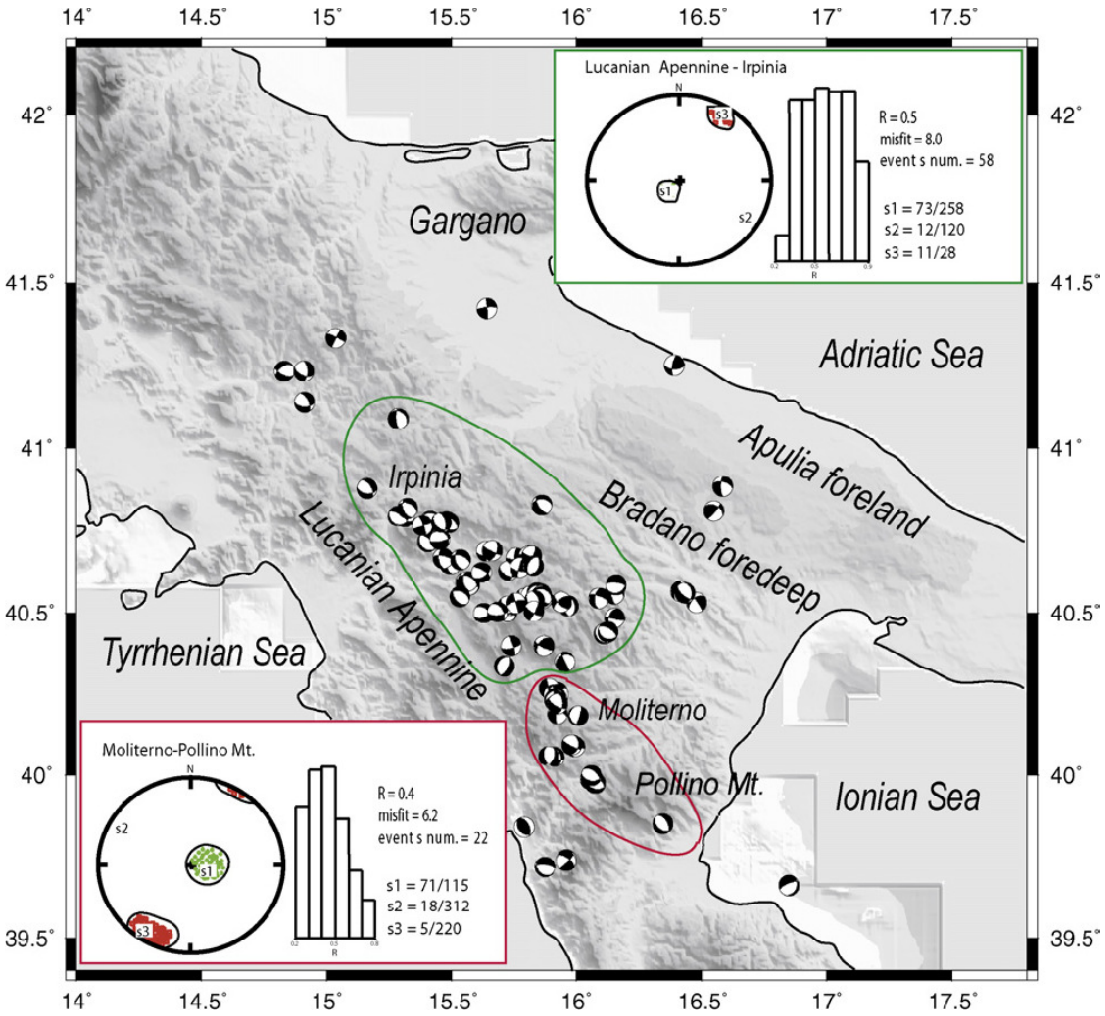

Figure 5.11: Stress inversion results using (a) the 58 fault-plane solutions located in the Lucanian Apennines–Irpinia area (green line), and (b) the 22 focal mechanisms of the Moliterno–Pollino Range area (red line). For each solution the stereonet plot is shown with the 95% confidence limits for σ_1 and σ_3 and the histogram illustrating the uncertainty in the dimensionless parameter R. Plunge and trend for the three principal stress axes, stress ratio R, misfit and total number of fault-plane solutions are shown to the right of the histograms (from Frepoli et al. 2011).

5.5 Discussion

The background seismicity analyzed in this chapter closely follows the pattern delineated by the seismicity of the last three decades (Castello et al., 2005, 2008; Chiarabba et al., 2005). Thanks to the SeSCAL passive experiment operated in the period between 2007-2008 I

increased considerably the dataset and the data collected by Maggi et al. (2009) (Table 5.4). Moreover, the results obtained by two database are similar.

Most of the events show hypocentral depths ranging between 5 and 25 km and are located in the Irpinia and Potentino areas, to the north, and in the Moliterno and north-western Pollino Range, to the South.

Dataset	Recording arrays	P-picks	S-picks	Relocated events	Quality A	Quality B	Quality C	Quality D	Focal mechanisms
A	RSNC, SAPTEX	7570	4956	359	226	69	31	33	58
B	RSNC, SAPTEX, SeSCAL	15666	9228	566	319	155	92	111	102

Table 5.4: Local earthquake datasets examined by (A) Maggi et al.(2009) and (B) Frepoli et al. (2011).

The observed seismicity overlaps the area characterized by the most active normal faults of the Southern Apennines (DISS, 2006; Basili et al., 2008). Regional extension drives the activity of these major NW-trending seismogenic faults, either NE or SW-dipping (Pantosti et al., 1993; Benedetti et al., 1998; Cello et al., 2003; Maschio et al., 2005). This normal fault system crosscuts the pre-existing contractional structures and bound the large intermountain basins (Cinque et al., 1993). Large part of the studied microseismicity in the Southern Apennines could be explained with the post-seismic crustal deformation process (Reddy and Prajapati, 2009 and reference therein), which can last for several years or decades, related to the 1980 Irpinia, 1990–1991 Potentino and 1998 Castelluccio–Lauria sequences. Post-seismic relaxation process with stress transfer from the large 1980 Irpinia earthquake to the Potentino seismogenic zone was analyzed by Nostro et al. (1997). As observed even in previous studies (Frepoli et al., 2005; Maggi et al., 2009), the Vallo di Diano–Upper Val d'Agri sector, located along the main axis of the Lucanian Apennine, is characterized by a scarcity of seismicity with only a few low-magnitude events recorded during this surveys (Table 5.3). The 8-year long monitoring period of this study shows a clustered seismicity with depth ranging between 5 and 20 km (Fig. 5.7a, b, cross-section GH). The shallower events of this swarm could be related with the fast water level changes in the Pertusillo reservoir as proposed by Valoroso et

al. (2009). Swarm-type activity is commonly observed in reservoir induced seismicity examples (Talwani, 1997 and reference therein). Following the macroseismic data (Branno et al., 1983, 1985; Alessio et al., 1995) and the most recent geological and geomorphological studies (Benedetti et al., 1998; Cello et al., 2003; Maschio et al., 2005), the active fault related to the destructive 1857 Basilicata earthquake (Me = 6.9; XI MCS) is hypothesized to be located within the Val d'Agri basin. Moreover, the background seismicity gap observed in the area is partially correlated in space with the epicentral zone of the complex seismic sequence occurred in 1561 (Me = 6.4; X MCS; Castelli et al., 2008). From a geological and a tectonical point of view the two strong events of 1561 and 1857 are located in an area characterized by the extensional basins of the Vallo di Diano and the Auletta. These major NW-trending normal faults should be considered as potential seismogenic sources in the seismic hazard valuation of this area (Amicucci et al., 2008). Within the transition zone between the Apenninic chain and the Bradano foredeep in the central Lucanian region I observe two seismic clusters E–W elongated. The first and smaller one, to the north, is located in the same area of the two Potentino sequences of 1990 and 1991, and shows hypocentral depths between 15 and 25 km. Directly to the South, the second cluster extends from the Abriola–Pietrapertosa sector to the Bradano foredeep, where some deep crustal events are recognized with foci between 30 and 40 km depth. I suggest that these two significant seismic features are representative of the transition from the inner portion of the chain, characterized by extension, to the external margin where dextral strike-slip kinematics is prevailing, as evidenced by the fault-plane solutions of the 1990 and 1991 Potentino seismic sequences (Azzara et al., 1993; Ekström, 1994) and, more to the north, of the 2002 Molise sequence (Di Luccio et al., 2005) and the Gargano seismicity (Del Gaudio et al., 2007). About the Molise and Gargano areas, it is important to note that the dextral strike-slip kinematics is related to the development of a lithospheric transfer zone produced by the differential retreat of two adjacent slab segments with the consequent segmentation of the thrust front (Scrocca, 2006). Scattered seismicity with larger hypocentral depth (generally between 20 and 40 km) is located beneath the Bradano foredeep, Apulia foreland and Taranto Gulf. The denser seismic station coverage reached in the last decade provides a more extensive low magnitude earthquake dataset. Hypocentral determinations within the Apulia foreland are improved. Background seismicity beneath the Tavoliere (northern Apulia foreland) is located between

the Mattinata fault (Gargano promontory) to the North and the Ofanto Graben to the South. This seismicity shows foci between 5 and 20 km depth. The only available focal mechanism for the area (#83 in Table 5.3; 9.8 km of depth) shows a pure strike-slip solution. Taking into account the main E–W oriented tectonic features of the Gargano area (Tondi et al., 2005; Piccardi, 2005; Argnani et al., 2009), this solution is consistent with the seismological observations reported by Del Gaudio et al. (2007) in which the northern Apulia foreland shows a regional stress combining NW compression and NE extension. The area hit by the 1560 Barletta–Bisceglie earthquake in the Ofanto Graben is characterized by few events of low magnitude with depth between 20 and 35 km and shallower events with depth ranging from 5 to 20 km. The focal mechanism #28 (Table 5.3), located in the Barletta–Bisceglie area at 23 km of depth, displays a strike-slip solution with a large inverse component (P-axis NW oriented), denoting a quite similar regional stress in this sector with that observed to the north in the Gargano area (Del Gaudio et al., 2007). The central portion of the Apulia foreland seems to be aseismic with the exception of the Altamura–Gravina di Puglia–Matera area, where both shallow (around 5–10 km) and deep (20–40 km) earthquakes are recognized. Two focal mechanisms are available for this sector (#45 and #87 in Table 5.3) with hypocentral depth of 37 and 29 km, respectively. Both solutions display a P-axis NNW oriented but with different kinematics. The first one extensional while the second one with a large inverse component. New observations of such lower crust seismicity are needed in order to better understand the seismotectonics of this area and its relationship with the geodynamic evolution of the Adriatic microplate. Within the Salento peninsula, only the area to the north of the Taranto city (Murge Tarantine) shows background seismicity with hypocentral depth scattered between 5 and 20 km. The crust beneath the Salento peninsula tip and its central part seems to be aseismic (Frepoli et al., 2011). Two small earthquakes, with depth around 30 and 40 km respectively, together with the deep Lucanian Apennine event (62 km of depth, M_L = 2.8), are representative of the flexure of the Adriatic lithosphere induced by the east-southeasterward migration of the Apenninic chain-thrust front system (Doglioni et al., 1994; Pieri et al., 1997; Gueguen et al., 1998; Rosenbaum and Lister, 2004). Offshore area southeast of the Salento peninsula was hit by seismic sequences of moderate magnitude in the years 1974, 1977 and 1991 (D'Ingeo et al., 1980; Favali et al., 1990; Argnani et al., 2001). Local stress accumulation due to the small radius of curvature of the Adriatic-Apulian plate under

the double load of the Hellenides and Apennines–Calabrian arc was proposed to be the main triggering factor (Argnani et al., 2001). The kinematics of the Lucanian and the southern Adriatic areas can be explained with the modern interpretation of the complex setting characterizing the central Mediterranean region dominated by the NNW–SSEEurasia–Nubia plate convergence (D'Agostino and Selvaggi, 2004). The westward flexural bending of the Adriatic continental lithosphere beneath the Lucanian region, associated with the increasing depth of the seismogenic layer (Chiarabba et al., 2005), is consistent with the presence of positive Bouger anomalies and very high heat flow values related to the uprising asthenospheric material in the upper mantle below the Tyrrhenian margin of the Apenninic chain and the adjacent Tyrrhenian Sea (Scrocca et al., 2005; Tiberti et al., 2005). The uplift and crustal thinning with the consequent active rifting process along the Apenninic belt are triggering the shallower seismicity (5–15 km of depth) within the chain. In addition to these observations, geothermal gradient and tomographic studies point out a brittle–ductile transition at 28–30 km beneath the foredeep and foreland compared with the 15–18 km of depth of the same boundary beneath the chain (Harabaglia et al., 1997; Chiarabba and Amato, 1996). My results show a seismogenic layer with depth of about 20 km beneath the chain (Fig. 5.7b, cross-sections AB, CD and EF), increasing down to over 30 km below the foreland area (Fig. 5.7b, cross-section GH). Besides focal mechanisms of strong earthquakes, fault-plane solutions of background seismicity are helpful in delineating the main seismotectonic provinces of a study area. The widespread NE extension observed in this chapter is consistent with previous studies concerning focal mechanisms of low to moderate magnitude events (Frepoli and Amato, 2000; Frepoli et al., 2005, 2011; Maggi et al., 2009). Taking into account the background seismicity gap located in the Vallo di Diano–Upper Val d'Agri sector, along the main axis of the Apenninic belt, fault-plane solution dataset is subdivided in two sub-datasets, one to the north with the Irpinia and Potentino area (58 focal mechanisms) and the other to the south including the Moliterno area and Pollino Range (22 fault-plane solutions). Both stress inversions display a very similar stress tensor orientation. The average misfit in the northern and more extended sector is quite large (8◦) (Frepoli et al., 2011). Probably this inversion result suffers from the influence of the stress field change within the selected area, from pure extension beneath the chain to a transpressive stress regime in the outer margin, as observed with the focal mechanisms of the two Potentino sequences of 1990 and 1991

(Azzara et al., 1993; Ekström, 1994). Moreover, as observed before, this tectonic shear regime characterizing the outer margin is also well shown by the fault-plane solutions of the 2002 Molise earthquake sequence (Di Luccio et al., 2005) and the focal mechanisms computed by Del Gaudio et al. (2007) for the Gargano area. However, the lack of pure reverse focal solutions in the southern foreland (Gargano and Apulia) suggests that accretion processes are not active at present.

The buoyancy forces acting beneath the Southern Apennines and related to the westward subduction of the Adriatic continental lithosphere could be responsible for the observed widespread NE extension.

Chapter 6

Detailed analysis of clustered seismicity

A high resolution imaging of seismicity distribution is very important to detect potential seismic structures. These data, with the active tectonics and historical earthquake information, are a powerful tool to constrain the regional seismotectonic, geodynamic context and to evaluate the hazard. In this chapter, I used a recent methodology called double-difference technique (DD) to further improve the earthquake locations. Later, considering this results and different data kinds available in literature, I carried out a detailed analysis of single groups of events named Irpinia, Potentino, Pietrapertosa, Moliterno, Castelluccio and Bradano foredeep, respectively. I relocated these events with DD technique using singular value decomposition method (SVD). Beyond, I computed composite focal mechanisms for the closely located events (maximum inter-event distance of 2 km) and with few observed polarities to compute singular event focal mechanisms by superimposing data from the events rupturing the same fault segment (Sbar et al., 1972). For this task, the major assumption is that all events used have the same focal mechanism, i.e. have the same radiation pattern, as the reference event (earthquake put in the centre of the cluster). This is reasonable if earthquakes occur along the same fault of the reference event. However, in practice, this condition is not necessarily real. Some earthquakes may occur on faults of a much different orientation from the reference event. Hence, composite projections rarely show a perfect separation of compressional and dilatational first motions. I reported only the most reliable solutions.

6.1 HYPODD relocation

I were able to relocate 474 events applying the double-difference (DD) earthquake location algorithm (Waldhauser and Ellsworth, 2000, Waldhauser, 2001) to the 566 events located with HYPOELLIPSE (see Chapter 5). The HYPODD algorithm can be used when the hypocentral distance between two earthquakes is small compared with the source-receiver distance and the velocity heterogeneity scale length (see Appendix E). Therefore, the ray paths between the events and common stations are similar and the difference in the travel-times for two events recorded by the same station can be attributed only to the spatial offset between the events (Fréchet, 1985; Got et al., 1994). I minimized the DD residuals for pairs of earthquakes at each station by weighted least squares using the conjugate gradients method (LSQR, Paige and Saunders, 1982) (see Chapter 2 section 2.2.3). The final solutions are found by iteratively adjusting the vector difference between the nearby earthquake pairs.

The hypocenters located with this programme appear more clustered but the seismicity distribution is not very different from that obtained with the HYPOELLIPSE code because the DD method is able to solve small structures. Figure 6.1a shows the 474 earthquakes relocated with the HYPODD algorithm (blue dots) and HYPOELLIPSE code (red dots), and Figure 6.1b, c shows the cross sections. Figure 6.2 shows histograms with a location error and depth of events distribution. I outline that HYPOELLIPSE statistics are obtained by absolute locations while the HYPODD statistics refer only to relative hypocenter locations. Moreover, the seismicity located with HYPOELLIPSE in the Taranto gulf was rejected by HYPODD because it is scattered, i.e. the distance between events is large compared to the maximum distance between event pairs and station (MAXSEP) imposed.

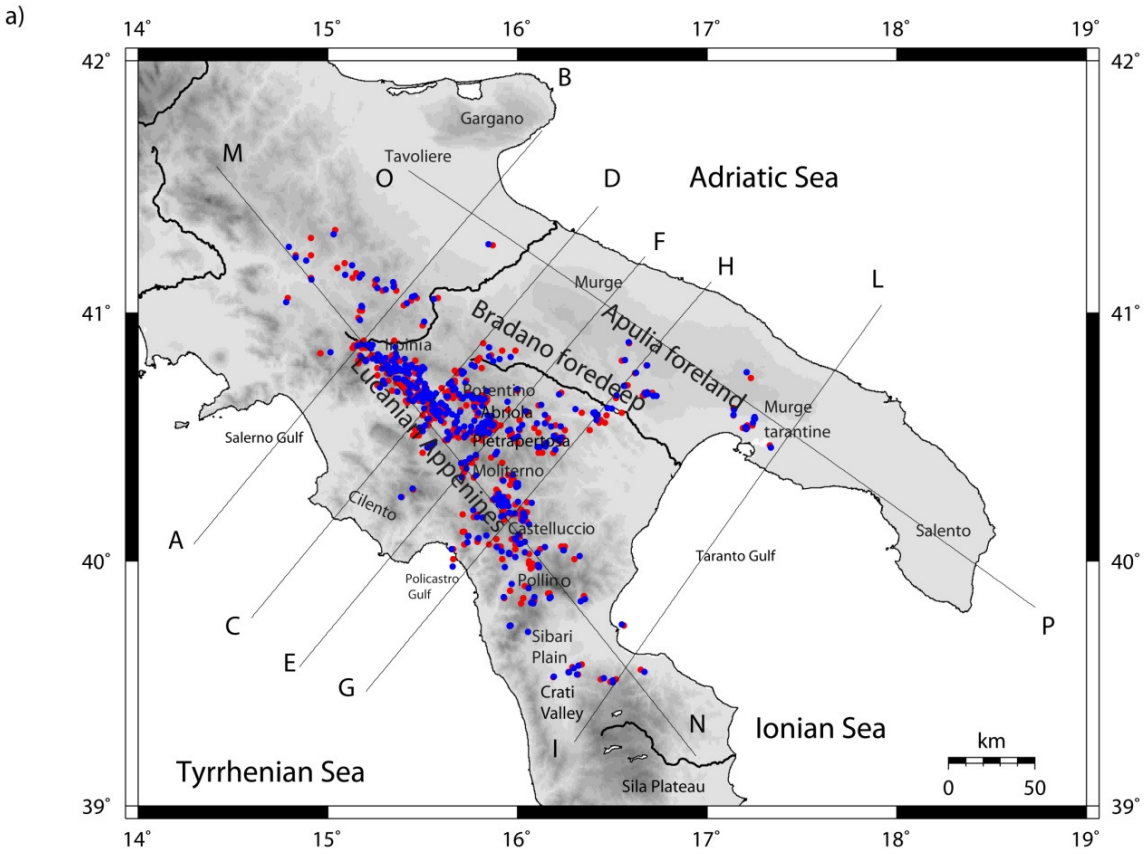

Figure 6.1: a) Map of epicentral distributions of 474 best relocated events by HYPOELLIPSE (red dots) and HYPODD (blue dots). b) Anti-Apenninic and Apenninic cross-sections for HYPOELLIPSE and HYPODD relocations.

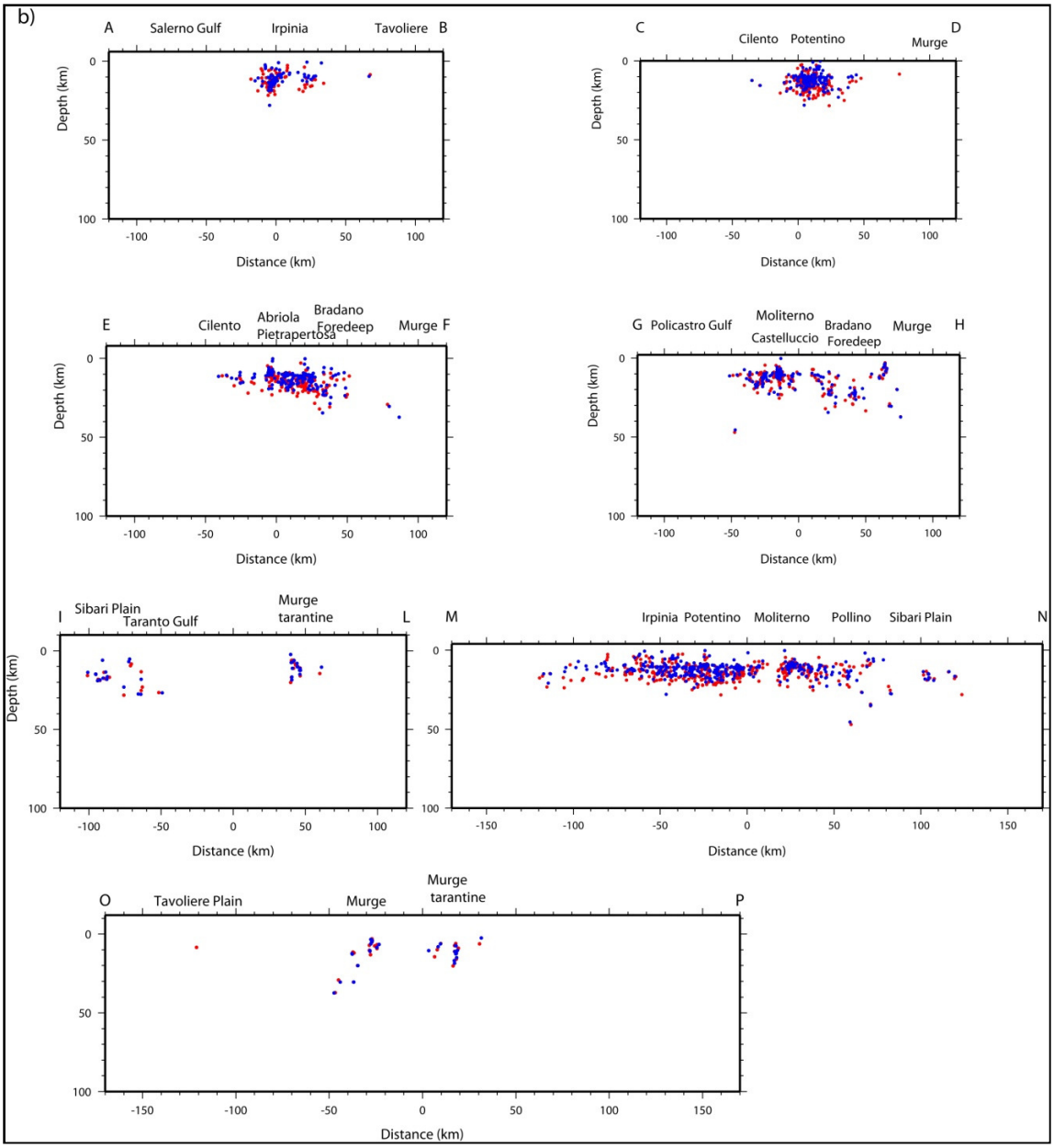

Figure 6. 1: (continued).

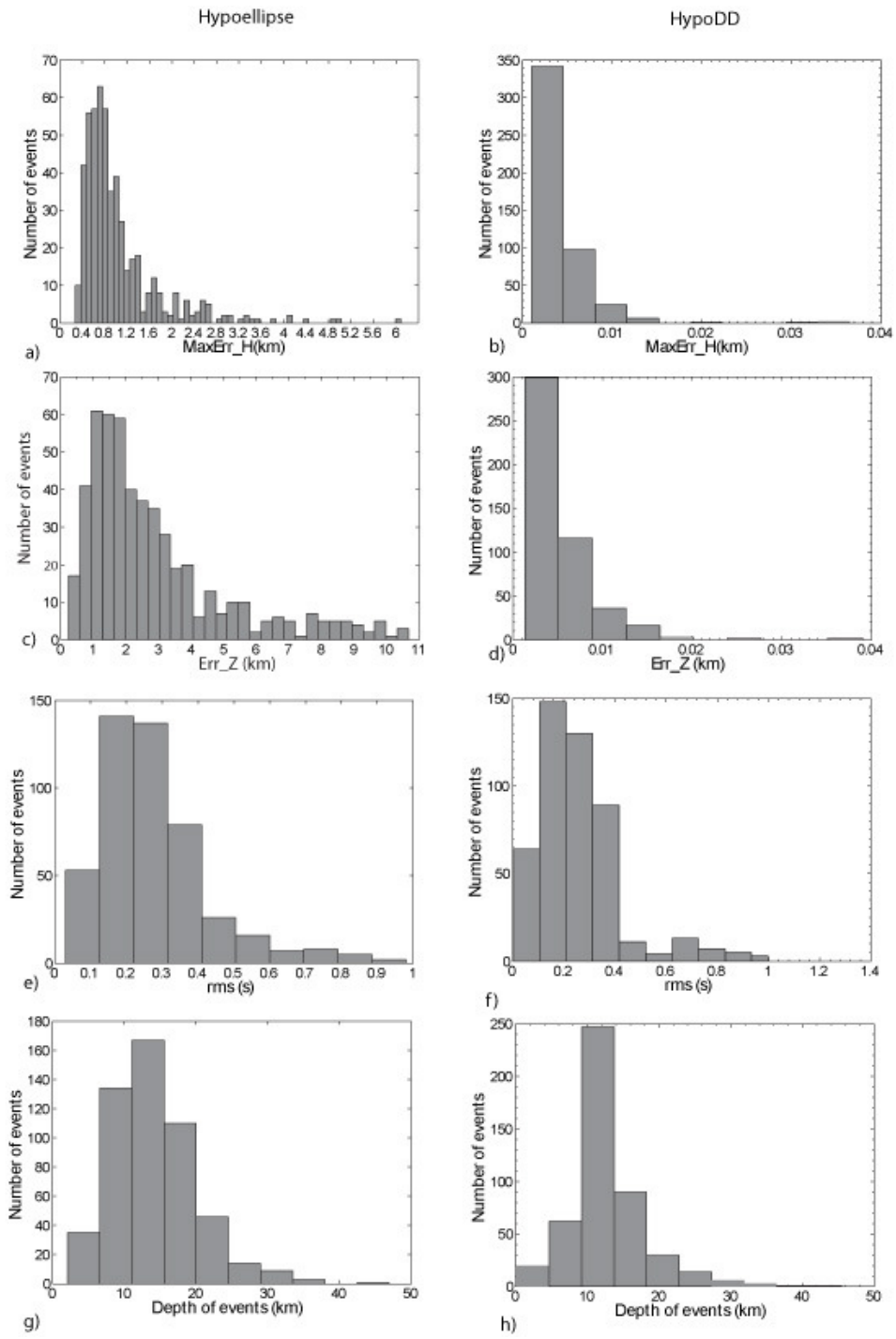

Figure 6.2: Event relocation statistics. Histograms (a), (c),(e) and (g) show maximum horizontal error, vertical error, rms and depth distribution of the 474 studied earthquakes located with HYPOELLIPSE and the *Test_8* velocity model; Histograms (b), (d), (f) and (h) show the relative error statistics for the same dataset relocated with HYPODD.

6.2 Group 1: Irpinia

This area was hit by a moment magnitude M_W=6.9 earthquake on November 23, 1980 (for more details see Chapter 1 section 1.2). It was the first well-documented example of surface faulting related with certainty to coseismic displacement (Pantosti and Valensise, 1990). This area was hit by other two historical events. The September 8, 1694 earthquake (M_W 6.9) damaged the same areas, and was characterized by the same region of maximum intensities of the 1980 event (Fracassi and Valensise, 2007). Moreover, it did not cause slip on the fault responsible for the 1980 earthquakes but was located in proximity of the antithetic fault (not observed on the surface). Another historical earthquake was that of April 09, 1853 with M_W 5.9, located to the East of the Picentini fault.

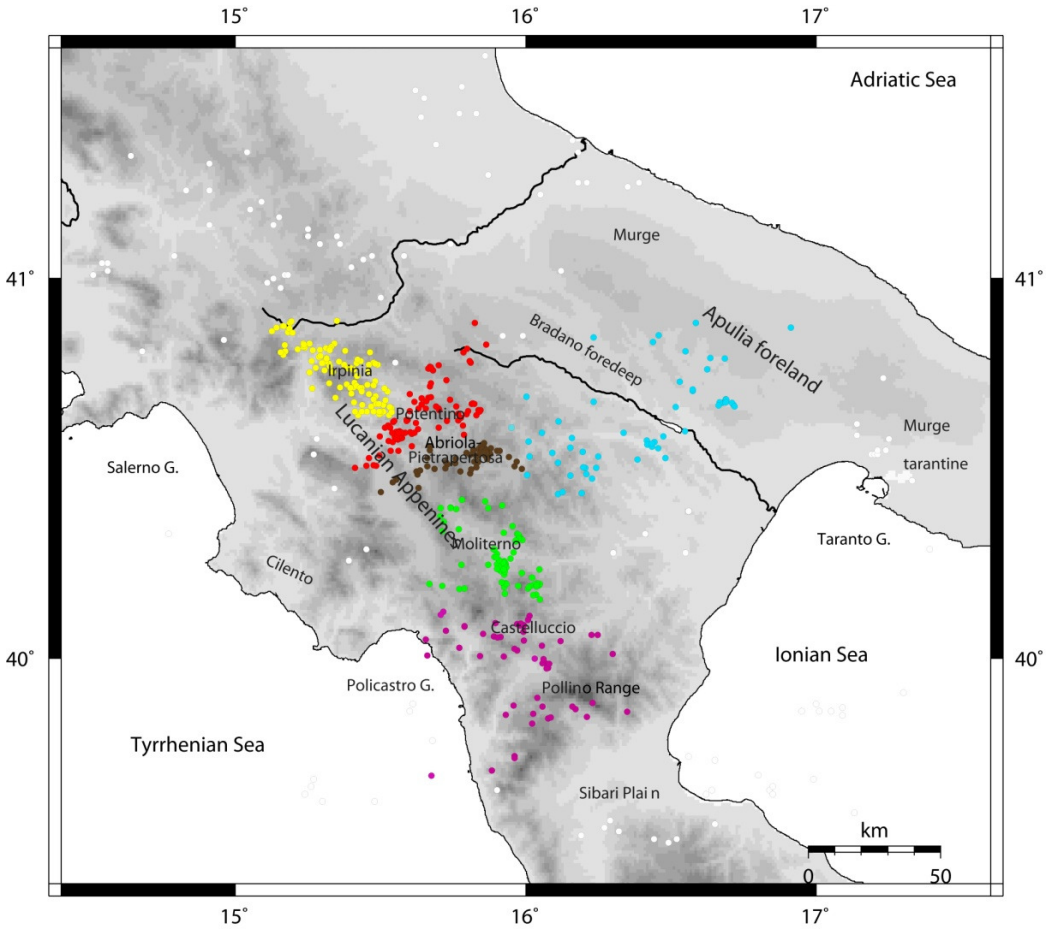

Figure 6.3: Map of HYPOELLIPSE location of 566 events. The different colors are used to indicate the events that form the six different groups analyzed with HYPODD.

The Irpinia group is located within an area ranging from 40.62° to 40.9° latitude N and from 15.10° to 15.54° longitude E. Initially, it was composed by 102 events located with HYPOELLIPSE code (see Fig. 6.3, yellow dots) but the HYPODD program relocated 97 earthquakes removing the isolated events. I observed a high concentration of hypocenters with depths between 10-18 km (Fig. 6.4 g, h). It is evident the improvement due to the DD method because the hypocenters are more clustered with respect to those obtained with the HYPOELLIPSE location (Fig. 6.5 a, b).

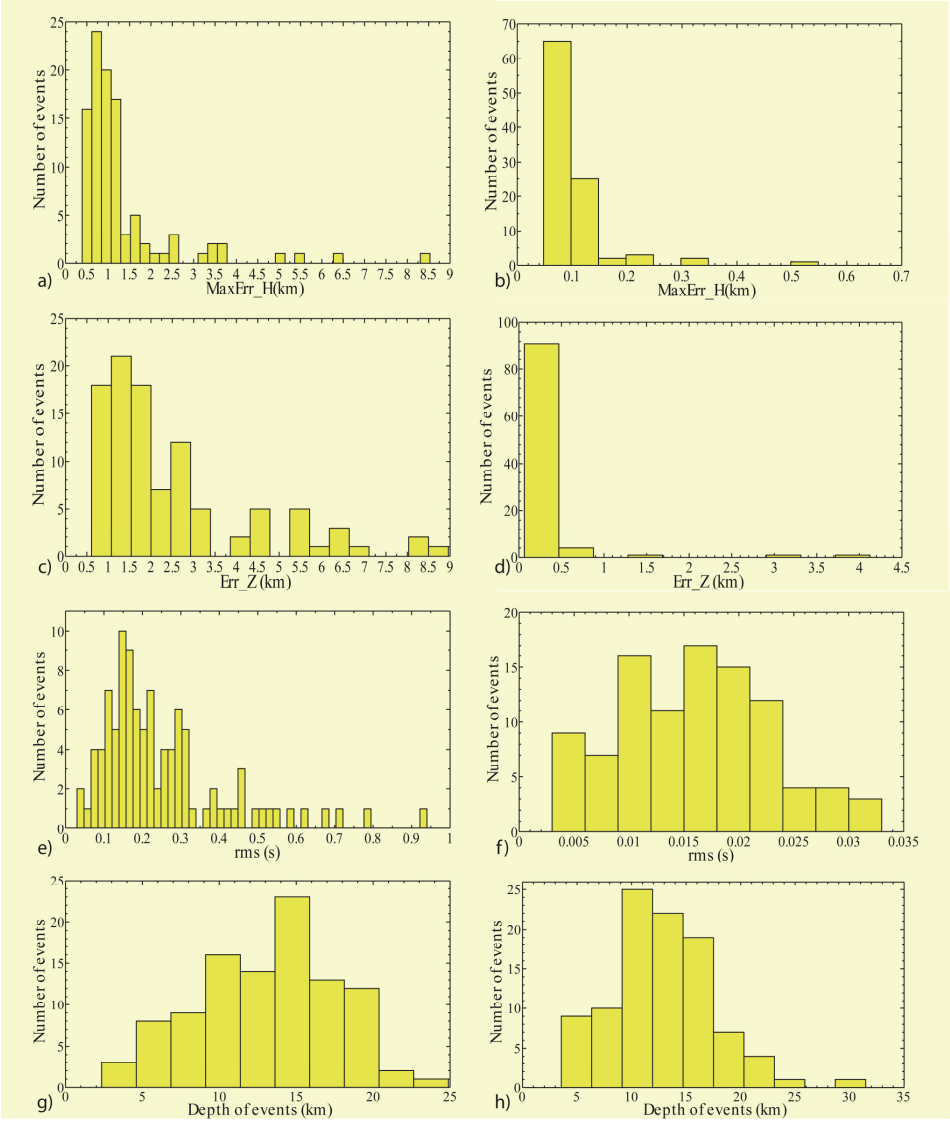

Figure 6.4: a, b) Maximum Horizontal (MaxErr_H) and c, d) vertical (Err_Z) errors (kilometres), e, f) rms (seconds) and g, h) depth distribution of the 97 best earthquakes located using HYPOELLIPSE (a, c, e, g) and HYPODD code (b, d, f, h).

Analyzing the epicentral distribution I observe that the hypocenters are mainly located within well-known structures of Irpinia (Fig. 6.5a, b) in the area of strong historical and instrumental earthquakes. In particular, I observe a denser cluster in the restrict area of the 1980 earthquake mainshock at SW Carpineta fault (with 315°strike and ~60° NE) (Fig. 6.5 b, d, f). In Fig. 6.5 f I observe that the seismicity contouring the hypothetical fault profiles. Moreover, the earthquakes distribution is very similar to that of the 1980 aftershocks, including the few sub-events that involved a low-angle rupture (dip ~20° NE) at the base of the brittle layer upper crust and started 20 s after the mainshock (Fig. 6.5, 6.6). Considering the increase of earthquakes depths moving from NW to SE and the hypothetical fault profiles, I supposed that the Carpineta-Marzano faults (dip ~60°NE) and antithetic fault (dip ~70° SW) are adjoined at 12 km depth on the SE end of Carpineta fault and at a smaller depth out of Marzaro fault (Fig. 6.5 c, d, e, f). Another result is the lack of seismicity associated at a gap of 6 km in surface faulting separating the Cervialto scarp (Picentini fault) from the Marzano-Valle scarp (Pantosti and Valensise, 1990) in the Valle del Sele area (easily erodible sediments). It is characterized by a strong low-velocity anomaly in the upper ~7 km suggesting that this area represents a creeping section of the Irpinia main fault, probably associated with a lithological and rheological discontinuity (Amato and Selvaggi, 1993). The discussed results are clearly visible in the hypocentral space distribution of earthquakes in the animation (irpinia.avi file).

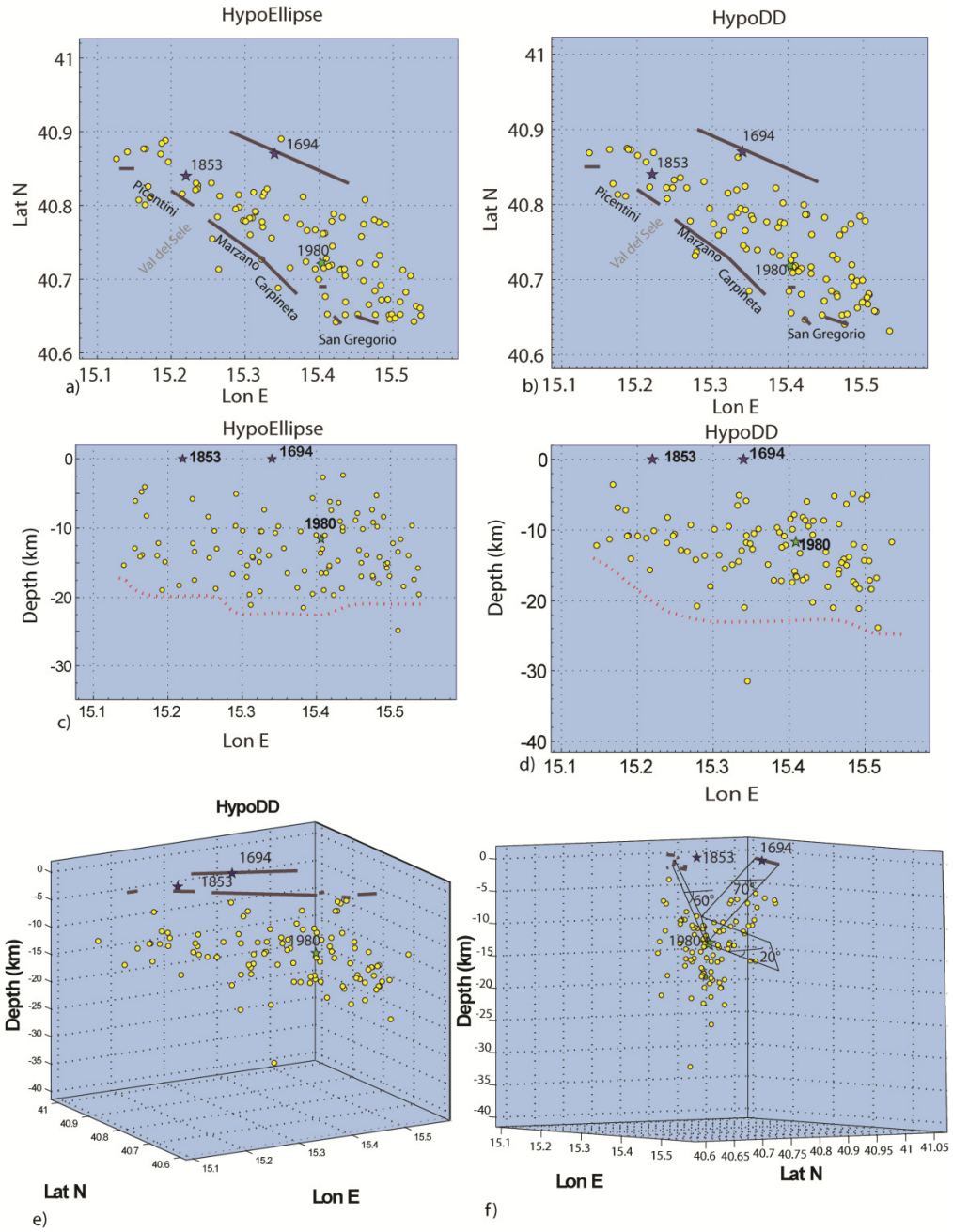

Figure 6.5: Map view of hypocentral distribution and sections WE of 97 events located with HYPOELLIPSE (a, c) and HYPODD code (b, d). Plot 3D of these events located with the DD method (e anti-apenninic, f apenninic observation directions respectively). The red dotted line traces an approximation of the seismogenic base. The brown line shows the active structure observed in this area (DISS Working Group, 2009). Blue stars represent epicentres of historical earthquakes (Fracassi and Valensise, 2007) and green star hypocenter of instrumental seismicity (Westaway, 1993). The bordered black areas show a hypothetical Marzaro-Carpineta structure and its associate antithetic fault (see Figure 6.7).

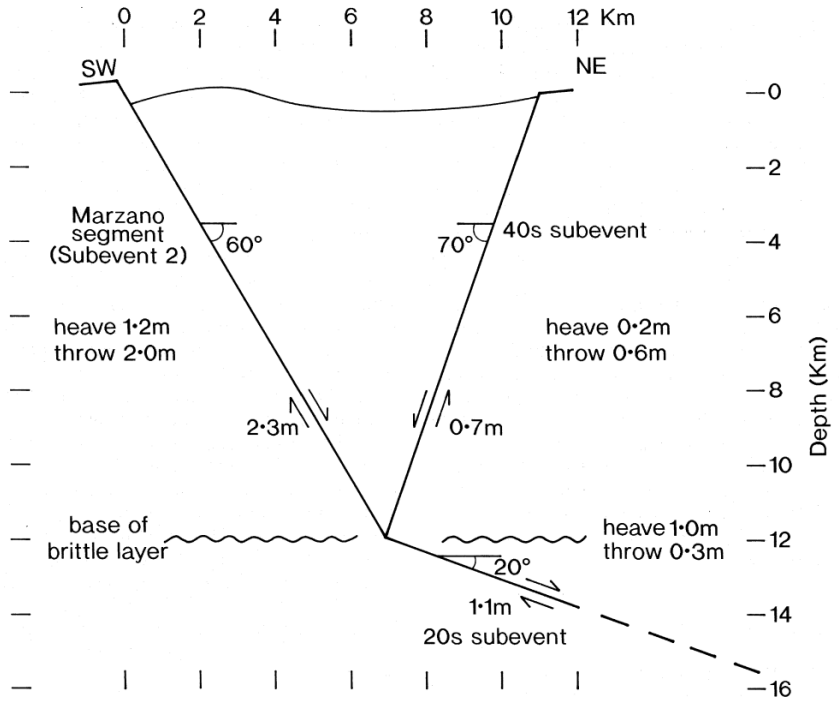

Figure 6.6: Schematic cross-section across the Marzano fault and the associated antithetic fault at 11km NE obtained by Westaway, 1993 for the 1980 Irpinia earthquakes.

6.3 Group 2: Potentino

The second group is located in the Potentino area (15.42-15.88 E, 40.5-40.9 N), which was hit by two moderate and minor seismic sequences occurred in 1990 (M_W 5.7) and 1991 (M_W 5.1) in the Potenza area at only 40-50 km ESE of the Irpinia 1980 zone (for more details see Chapter 1 section 1.2). This group consists of 89 events located with HYPOELLIPSE (Fig. 6.3 red dots). Relocating 84 earthquakes with HYPODD code I obtained denser clusters. In this way I could observe that most of earthquakes have foci within the 7-20 km depth range (Fig. 6.7 g, h). Moreover, hypocentral locations improved with the DD method. Analyzing the epicentral distribution it is possible to remark that the earthquakes are mainly located to the SW of the two Potentino sequences on November 9, 1990 (M_W 5.7) and May 26, 1991 (M_W 5.2) (Fig. 6.8 a, b). However the hypocentre depths are concentrated between ~8-20 km in the Savoia di Lucania area, while they were deeper (~13-28 km) in the 1990-1991 seismic sequence zone. A

small seismic sequence, started with the event of April 18, 2002 (local magnitude M_L 4.1, Frepoli et al., 2005), is located at 12.4 km of depth beneath Savoia di Lucania (Fig. 6.8 a, b). Hypocentral depths of this sequence is ranging between 8 and 13 km (Fig. 6.8 c, d) and slightly elongated in a NW-SE direction (Fig. 6.8 f).

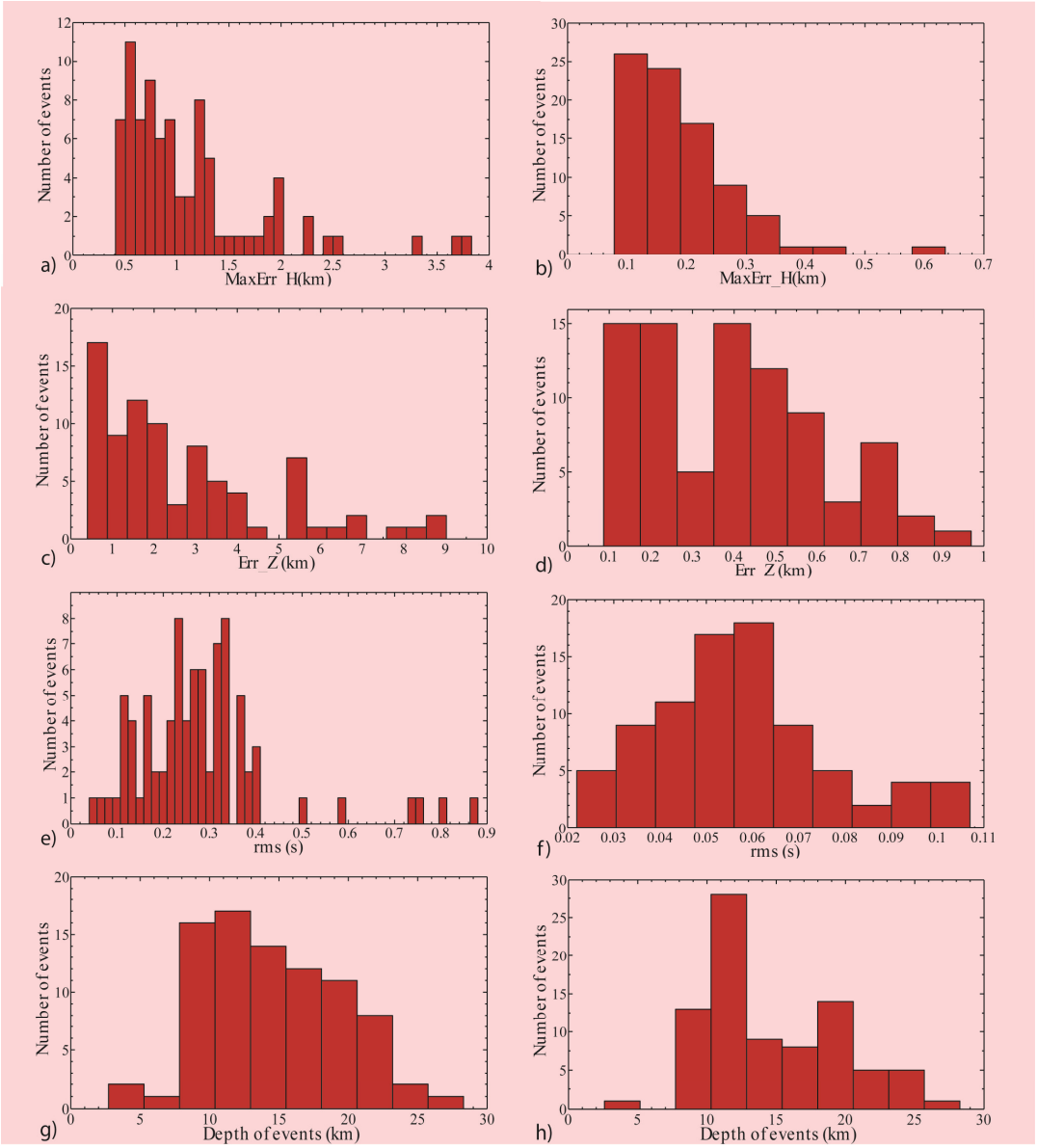

Figure 6.7: Rms residuals (seconds), horizontal and vertical errors (kilometres) and depth distribution of the 84 earthquakes located using HYPOELLIPSE (a, c, e, g) and HYPODD code (b, d, f, h).

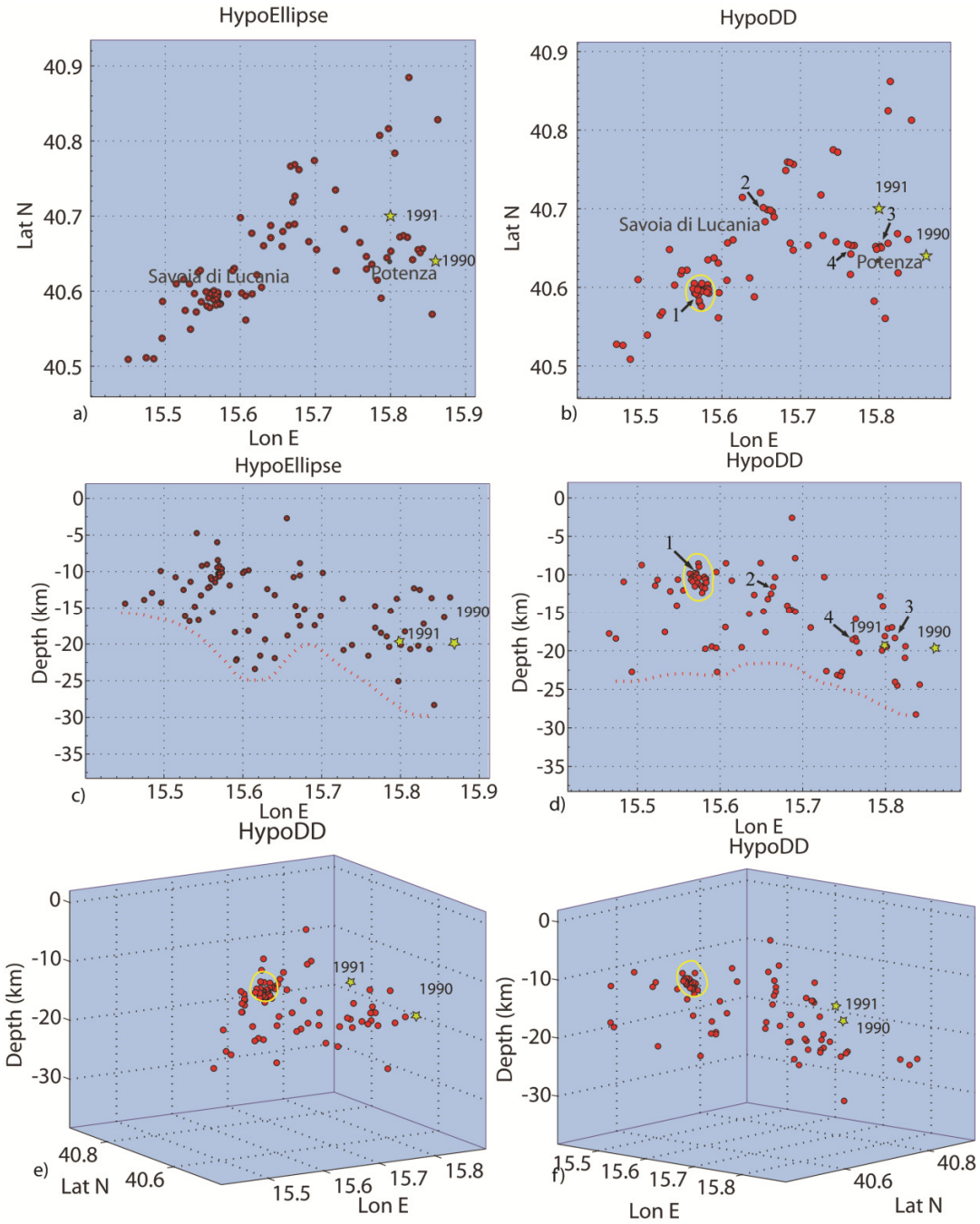

Figure 6.8: Map view of hypocentral distribution and W-E cross-sections of the 84 events located with HYPOELLIPSE (a, c) and HYPODD code (b, d). 3D plots of events relocated with DD method (e anti-apenninic, f apenninic observation directions respectively). Green stars hypocentre of instrumental earthquakes (Azzarra et al., 1993; Di Luccio et al., 2005). Red dotted line trace variation in seismogenic base. Yellow circle outlines the Savoia di Lucania cluster. Numbers indicate clusters used to compute composite focal mechanisms in Figure 6.9.

Analyzing the earthquake distribution and computing composite focal mechanisms I distinguish two different zones. The first zone is located along the Apenninic chain in the upper crust (Inner Apulian carbonate platform) with a seismicity distribution observed along a NE-SW direction. It is characterized by normal fault plain solutions (Fig. 6.9 Potentino 1, 2) with NE-SW extension as the Southern Apennine chain earthquakes. While in the second area, where the Apennine units overthrust the Apulian crust, I observe a strike-slip seismicity elongated EW and characterized by a right-lateral strike-slip nodal plain as the 1990-1991 Potenza sequences (see Fig. 6.9, Potentino 3, 4). The different tectonic and the deeper depths of the events located in the eastern of Apenninic chain might be explained by rheological stratification of the crust which consists of a strong brittle layer at middle crustal depths between two plastic horizons associated to the E-W faults affecting the foreland region of Apennine (Fig. 6.10). These faults propagate up to 25 km of depth and the earthquakes of this area reflect the reactivation, during Middle-Late Pleistocene, of a deep pre-existing fault system (Di Luccio et al., 2005) which probably resulted from the SE displacement of the Calabrian Arc (Bonini et al., 2011). These shear zones are in good agreement with the deformation field affecting the Gargano area and the Apulia foreland.

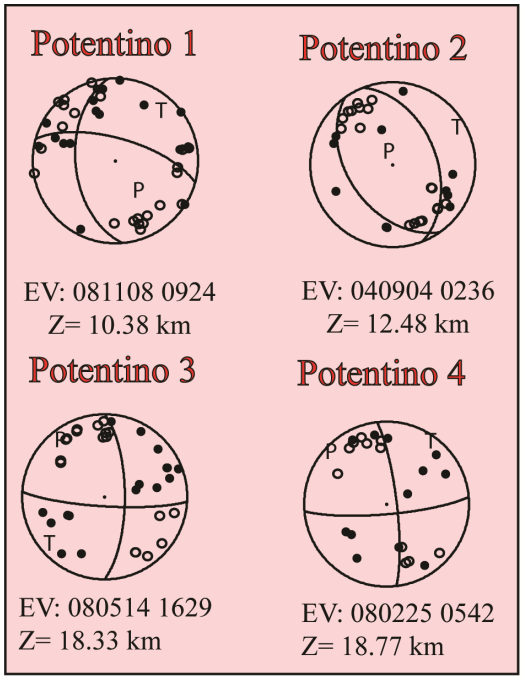

Figure 6.9: Composite focal mechanisms computed for four clusters located in the Potentino area (see Fig. 6.8b, d 1,2,3,4).

The discussed features are clearly visible in the hypocentral space distribution of earthquakes through the animation of the potentino.avi file.

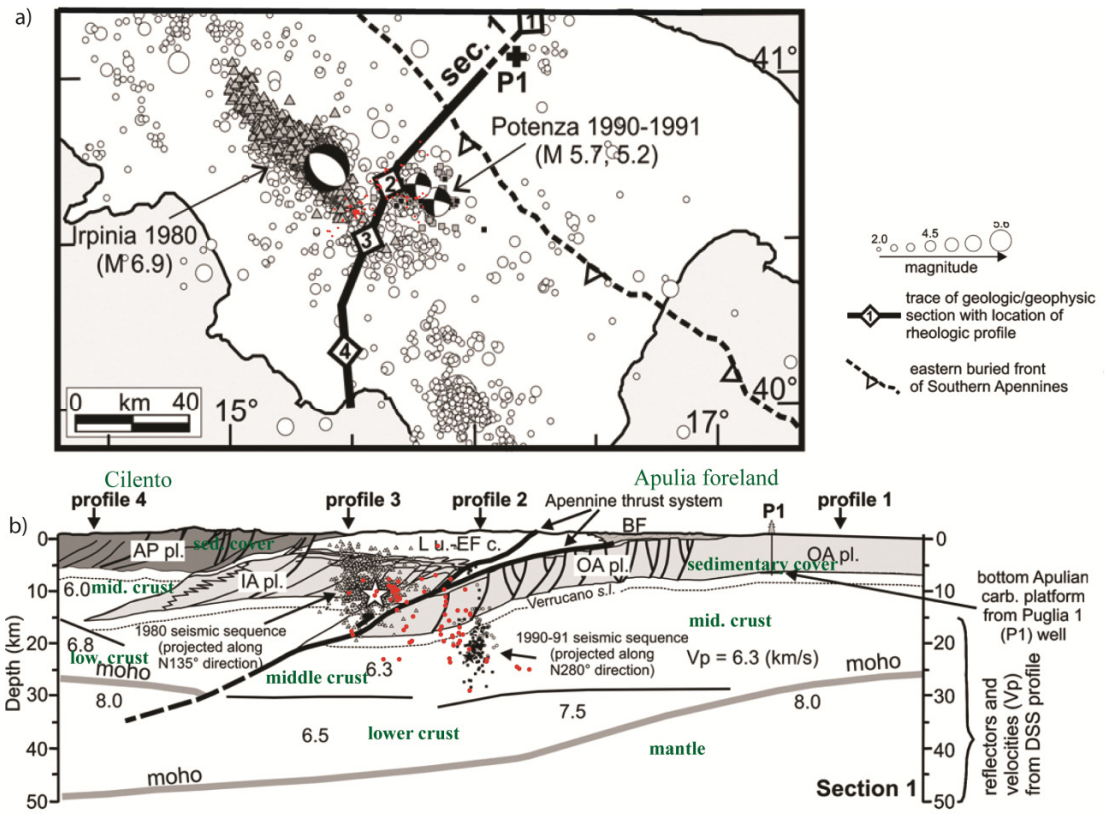

Figure 6.10: a) Map of Southern Italy with 1981–2002 seismicity from CSI catalogue (Castello et al., 2006), location of the 1980 Irpinia, 1990–1991 Potenza aftershock sequences and the ours HYPODD relocations (red dots) for the Potentino area. b) Seismotectonic section across southern Italy with projection of the 1990–1991, 1980 earthquake sequences, ours potentino relocations (red dots) and the geologic section (figure modified from Boncio et al., 2007). AP pl.=Apennine carbonate platform; IA pl.=Inner Apulian carbonate platform; OA pl.=Outer Apulian carbonate platform; Lu.-EF c.=Lagonegro units and External Flysch complex; Mo-Sa u.=Molise and Sannio units; Ap. u.=Apennine units; BF=Bradanic foredeep.

6.4 Group 3: Pietrapertosa

This area is characterized by scarce seismicity and is located between the maximum intensity areas of two of the most destructive earthquakes reported in the Italian seismic catalogue: the Val d'Agri earthquake (1857) and the Irpinia earthquake (1980). It is not associated with known historical events and for this reason is currently object of investigation as a potential seismic gap. In fact the probability of future ruptures is higher than in surrounding regions, also for the static stress increase caused by the two above mentioned earthquakes (Lucente et al., 2005). This group is located in the area between 40.44°-40.57°N of latitude and 15.50°-16.00°E of longitude named Abriola-Pietrapertosa and consists of 67 earthquakes (Fig. 6.3 brown). I relocated 64 events with the DD method improving the hypocentral locations (Fig. 6.11, see pietrapertosa.avi). The background seismicity of this area was characterized by isolated events and a superimposed a swarm. The increased number of seismic stations in the study area, with the temporary array of the passive experiment SeSCAL, allowed me to record and relocate these events with good accuracy. Most of earthquakes show hypocentral depths between 10 and 18 km (Fig. 6.11 g, h). These relocated events are elongated in a E-W direction. A new result in this work is given by the observation of the swarm of November 2008, which consists of 33 events ($1.0 \leq M_L \leq 2.9$) with a hypocentral distribution that depicts a sub-vertical plane (Fig. 6.12). This cluster is oriented along a NW-SE direction (Fig. 6.12 a, b) to the east of Apenninic chain and shows a depth range of 10-17 km and a length of ~2 km (Fig. 6.12 c, d). I will analyze in detail this swarm using the cross-correlation method and computing composed focal mechanisms in Chapter 7.

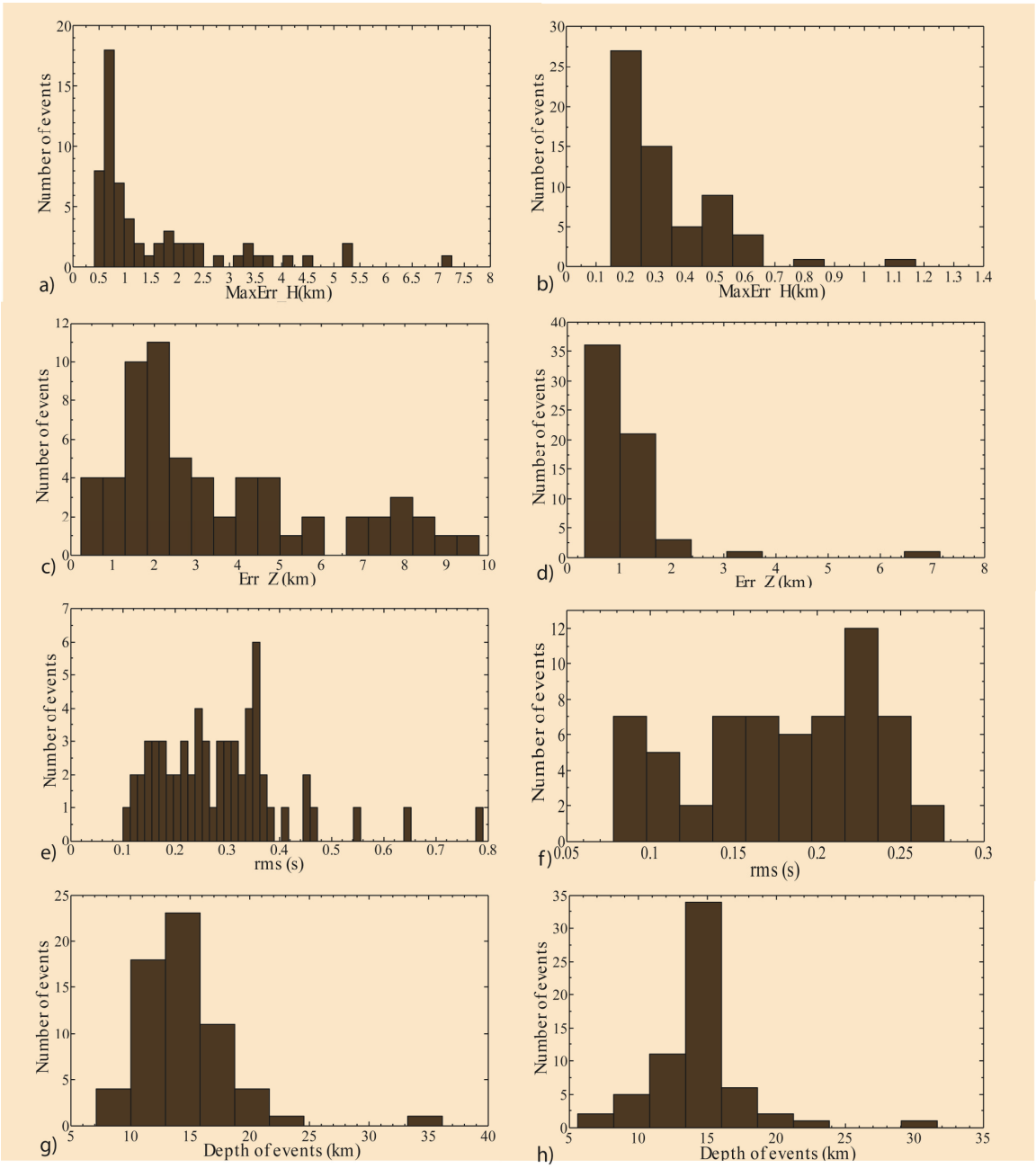

Figure 6.11: Rms residuals (seconds), maximum horizontal (MaxErr_H) and vertical (Err_Z) errors (kilometres) and depth distribution of the 64 earthquakes located with HYPOELLIPSE (a, c, e, g) and HYPODD code (b, d, f, h).

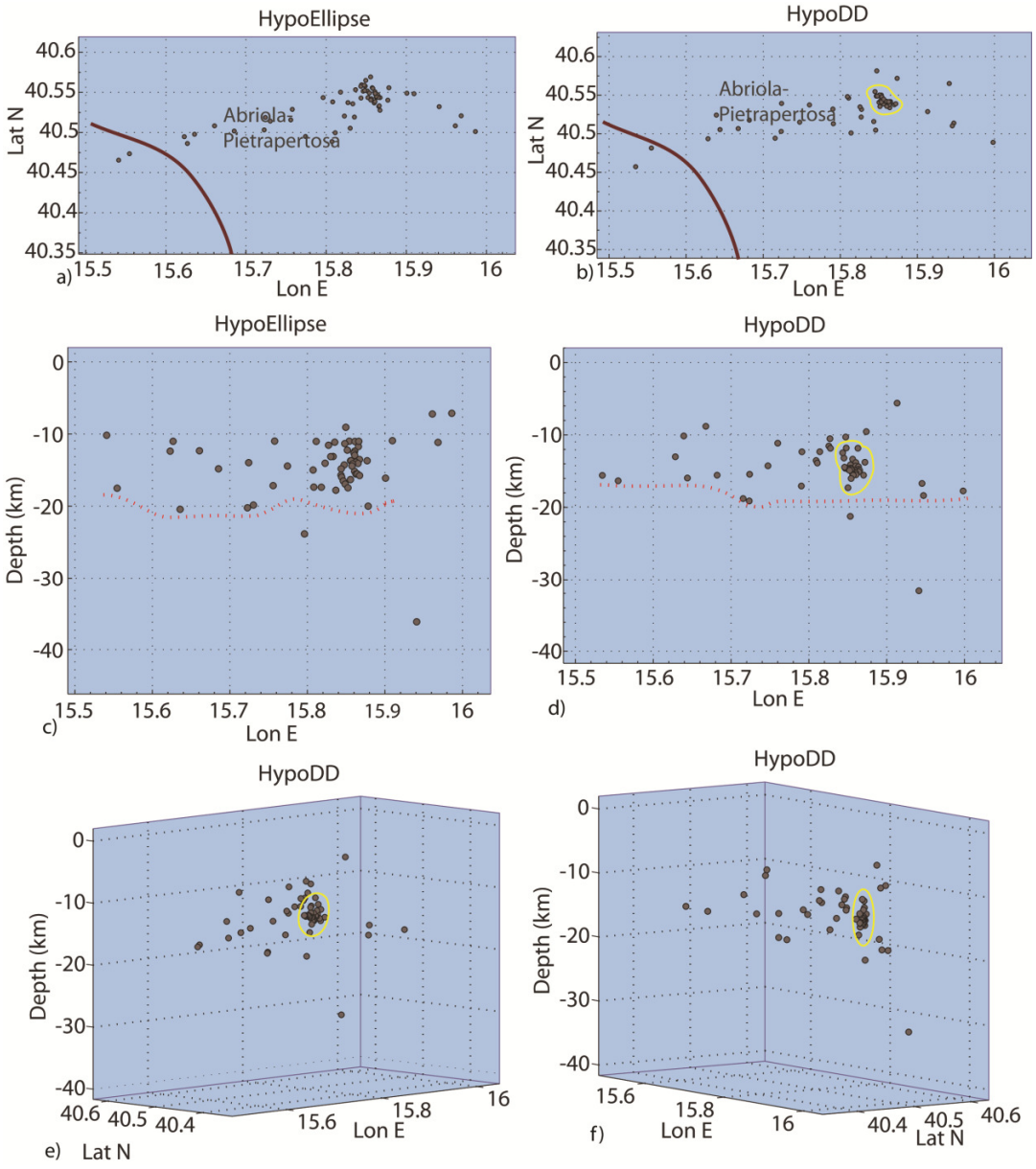

Figure 6.12: Map view of the hypocentral distribution and W-E cross-sections of the 64 events located with HYPOELLIPSE (a, c) and HYPODD code (b, d). 3D plots of events relocated with DD method (e anti-apenninic, f apenninic observation directions respectively). Red dotted line trace variation in seismogenic base. Yellow circle outlines the cluster of the Abriola-Pietrapertosa swarm.

6.5 Group 4: Moliterno

The Moliterno zone includes the area of Auletta Basin, Vallo di Diano and Val d'Agri (40.10°-40.43° N of latitude and 15.62°-16.10°E of longitude) (Fig. 6.3 green dots). This area with the northern Irpinia boundary, is characterized by scarce seismicity in my period of observation. Within the Val d'Agri basin a destructive event occurred in 1857 (Mw 7.0, Boschi et al., 2000) (for more details see Chapter 1 section 1.2) characterized by a normal fault NW-trending and NE-dipping (Monti della Maddalena Fault System MMFS) similar to the 1980 Irpinia earthquake. This seismicity distribution consists of 78 earthquakes (Fig. 6.3 green dots) but I relocated 74 events with the DD method improving hypocentral locations (Fig. 6.14, see moliterno.avi). Events are mainly located within the 9-15 km depth range (Fig. 6.13 g, h). Hypocenters appear more clustered by using the HYPODD code, mainly, the Moliterno cluster located at SW of Pertusillo lake to the SE of the Upper Val d'Agri active faults in an area of 3.4 km × 4.5 km (Fig. 6.14 yellow circle). It includes events of a significant swarm named Moliterno studied by Frepoli et al., 2005 (February-December 2002). They analyzed this seismicity and observed that in the first period few events had a $M_D \leq 2.8$; then, during June-September, there was a quiescence period. Later on starting from October 2002, the seismicity increased again. The relocated events of the Moliterno swarm show hypocenter depths between 6 and 11 km and these could be regarded as a reservoir induced seismicity associated with the initial impoundment and/or with great and rapid water level changes in the reservoir. It results from an instantaneous effect of loading (or unloading) and delayed effect due to pore pressure diffusion (Gupta et al., 1972 Talwani et al., 1997). The Pertusillo lake level shows an evident change with an annual cycle: it rapidly rises from November to March, and slowly lowers from June-October (Valoroso et al., 2009). Moreover, the occurrence of seismicity increase with the growth of water level and decrease with reduction of this. The composite focal mechanisms of this cluster is a normal solution with strike parallel to the lake (Fig. 6.15 Moliterno 1).

To the east and the NE of the Moliterno swarm the microseismicity is rather sporadic. In particular I located two clusters: the first to the SE of the eastern Agri Fault System (EAFS) and the second to the south characterized by a normal mechanism trending NW-SE with a SW-dipping following the main seismogenic structure EAFS (Fig. 6.15 Moliterno 2, 3).

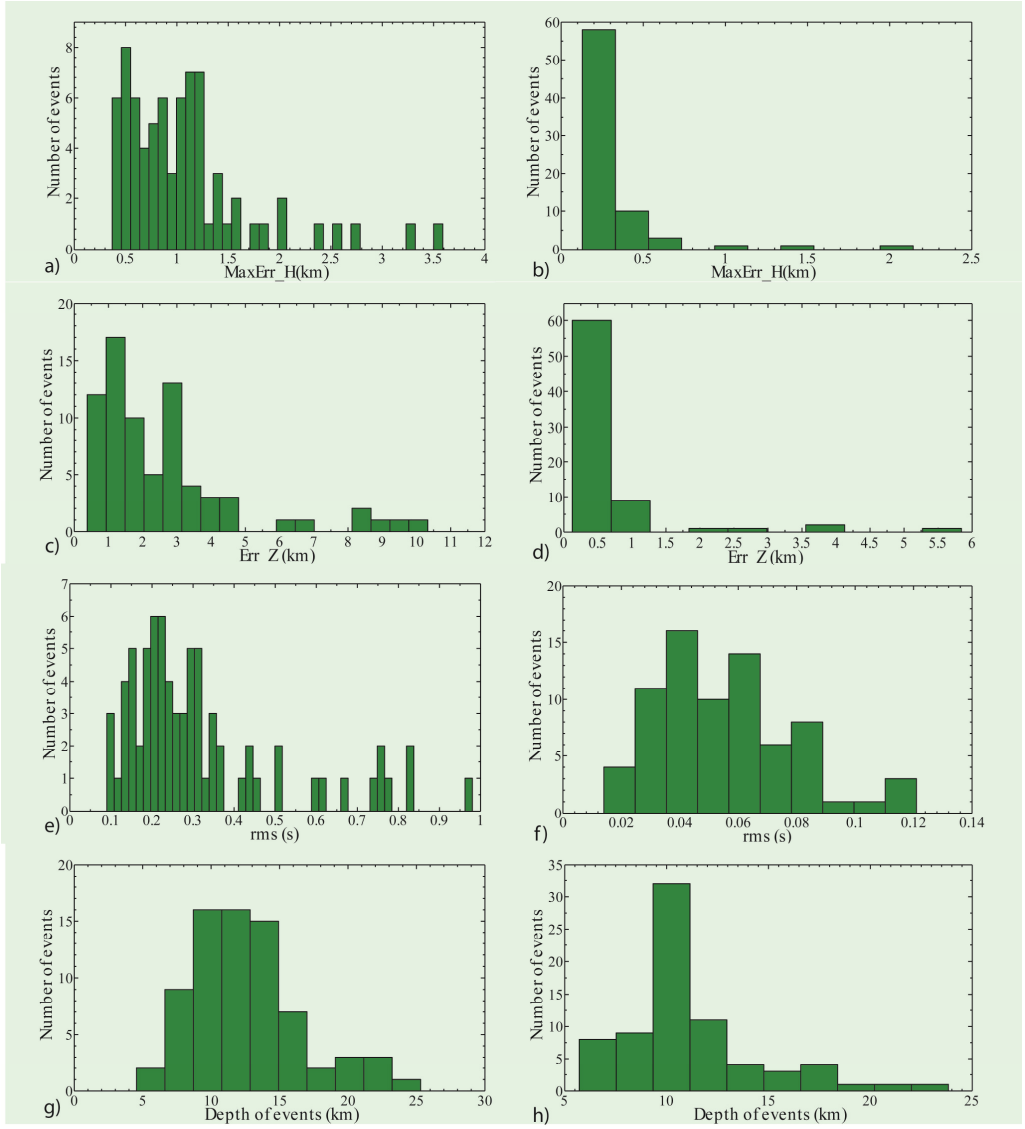

Figure 6.13: Rms residuals (seconds), horizontal and vertical errors (kilometres) and depth distribution of the 74 earthquakes located using HYPOELLIPSE (a, c, e, g) and HYPODD code (b, d, f, h).

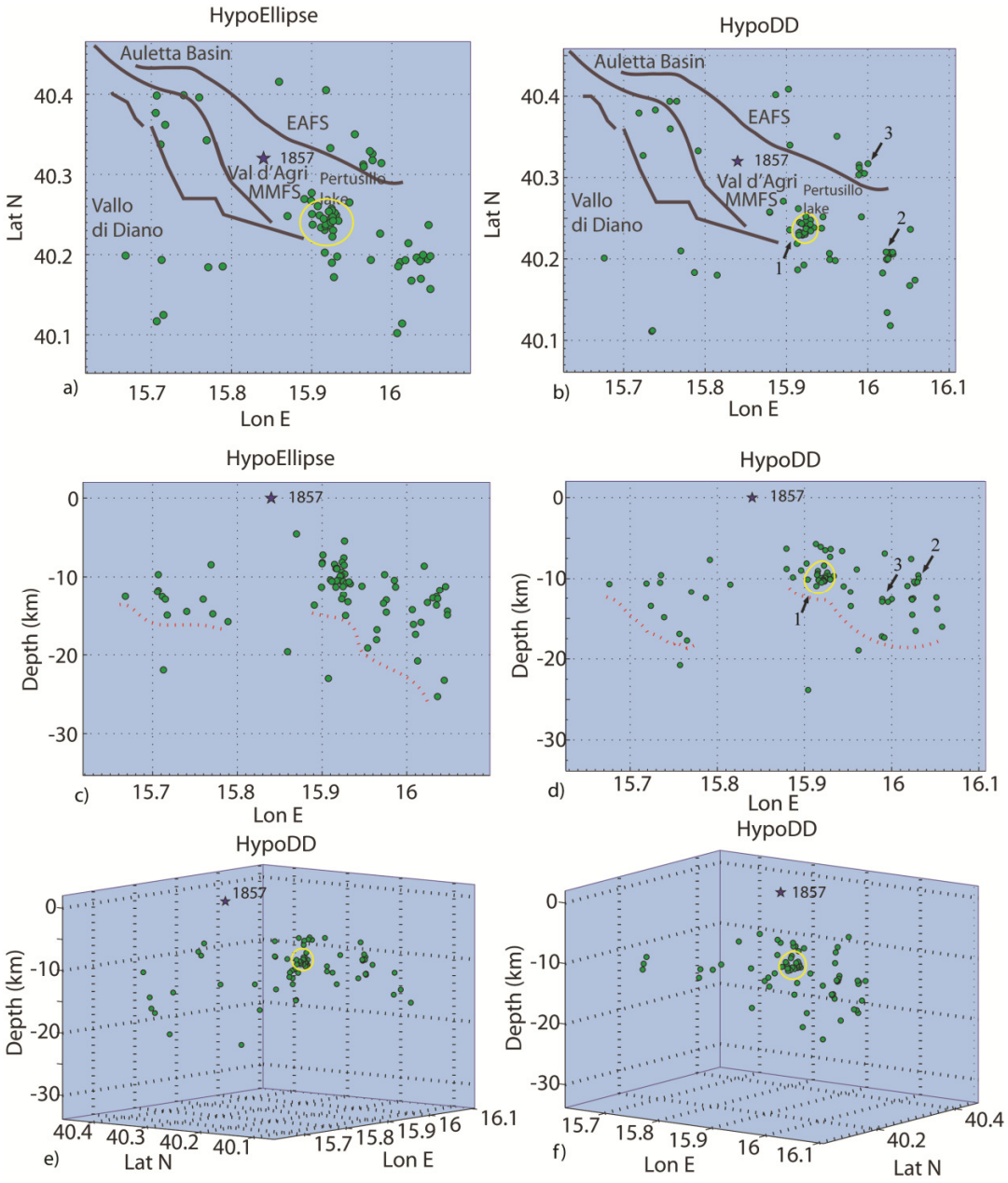

Figure 6.14: Map view of the hypocentral distribution and W-E cross-sections of the 74 events located with HYPOELLIPSE (a, c) and HYPODD code (b, d). 3D plots of events relocated with DD method (e anti-apenninic, f apenninic observation directions respectively). Red dotted line trace variation in seismogenic base. Brown lines show the active structures observed and Quaternary fault in this area (DISS Working Group, 2009, Maschio et al. 2005). Blue star: epicentre of historical earthquake (Pantosti and Valensise, 2007). Yellow circle outlines cluster of the Moliterno sequence. Numbers indicate clusters used to compute composite focal mechanisms (Fig. 6.16). Monti della Maddalena Fault System (MMFS). Eastern Agri Fault System (EAFS).

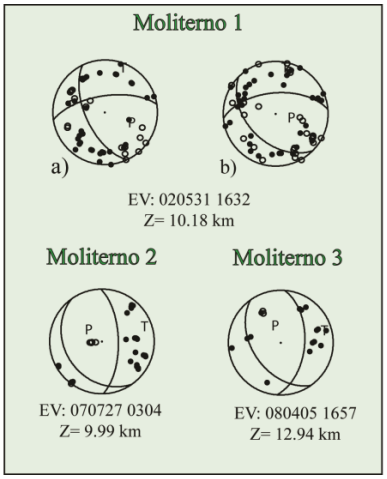

Figure 6.15: Composite focal mechanisms computed for three clusters located in the Moliterno area (see Fig. 6.14 b,d 1,2 and 3).

6.6 Group 5: Castelluccio

Southern Italy is divided in two regions: the southern-most one is called Calabrian Arc, where the Ionian lithosphere still subducts beneath the Tyrrhenian Sea. The second region located to the north of the Calabrian Arc, is called Southern Apennines and constitutes the accretionary prism of the Adriatic plate subduction. These two geodinamically separated regions meet in the Pollino Chain. I studied the region surrounding this Chain (Fig. 6.3, magenta dots).

The seismicity of this group is concentrated between 39.62°-40.14° N latitude and 15.65°-16.36° E longitude in the area of the Mercure Valley (Castellucio area) and the South of the Pollino Range, which, initially, consisted of 54 earthquakes. The microseismicity of this group is located in the same area of the small 1998 seismic sequence of Castelluccio (mainshock M_W 5.6) (for more details see Chapter 1 section 1.2). I relocated 50 events with the DD method improving hypocentral locations (Fig. 6.17, see castelluccio.avi). Hypocenters are more concentrated in the 10-15 km depth range following the Castello Seluci to Piana Perretti and Timpa della Manca fault (CSPT) (Fig. 6.16g, h) observed for the first time by Brozzetti et al., 2009. This seismicity, as the 1998 sequence, involves the sedimentary cover of the region where two important contacts exist: the boundary between the Apenninic Chain and the Calabrian Arc (at the surface) and the limit between the Adriatic and the African plate (in depth). These contacts are not yet well understood either at subduction on crustal levels (Guerra et al., 2005). The CSPT fault was the individual source associated to the 1998 Mercure events that fits well the mainshock and the aftershocks hypocentral locations and the distribution of the damages at surface.

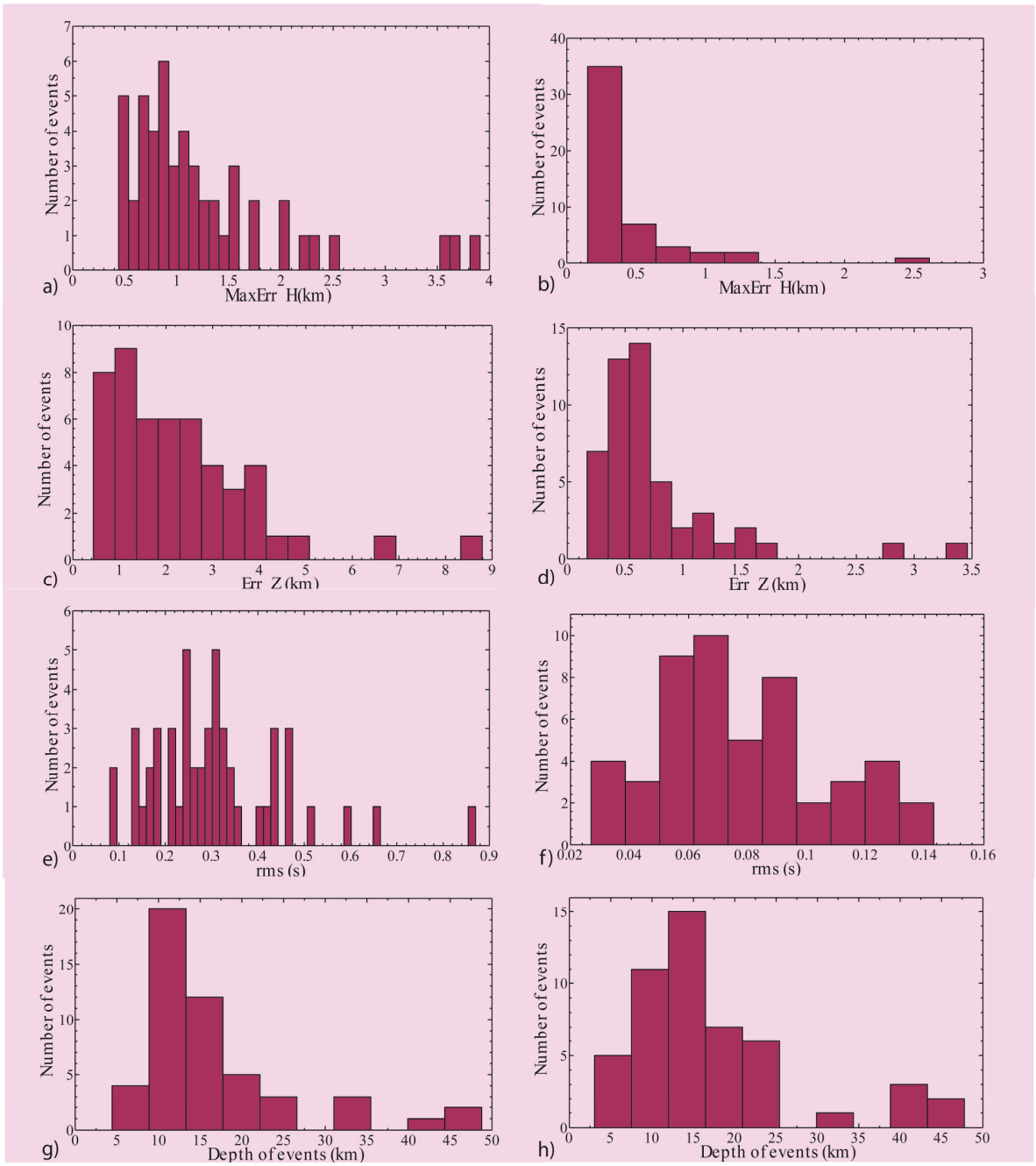

Figure 6.16: Rms residuals (seconds), maximum horizontal (MaxErr_H) and vertical (Err_Z) errors (kilometres) and depth distribution of the 50 earthquakes located using HYPOELLIPSE (a, c, e, g) and HYPODD code (b, d, f, h).

Its maximum extent was 18 km (field data) and its plane dips SSW-ward with an average dip of 60° and a down-dip length of nearly 12 km in agreement with my seismicity distribution and composite focal mechanism (Fig. 6.17, 6.18).

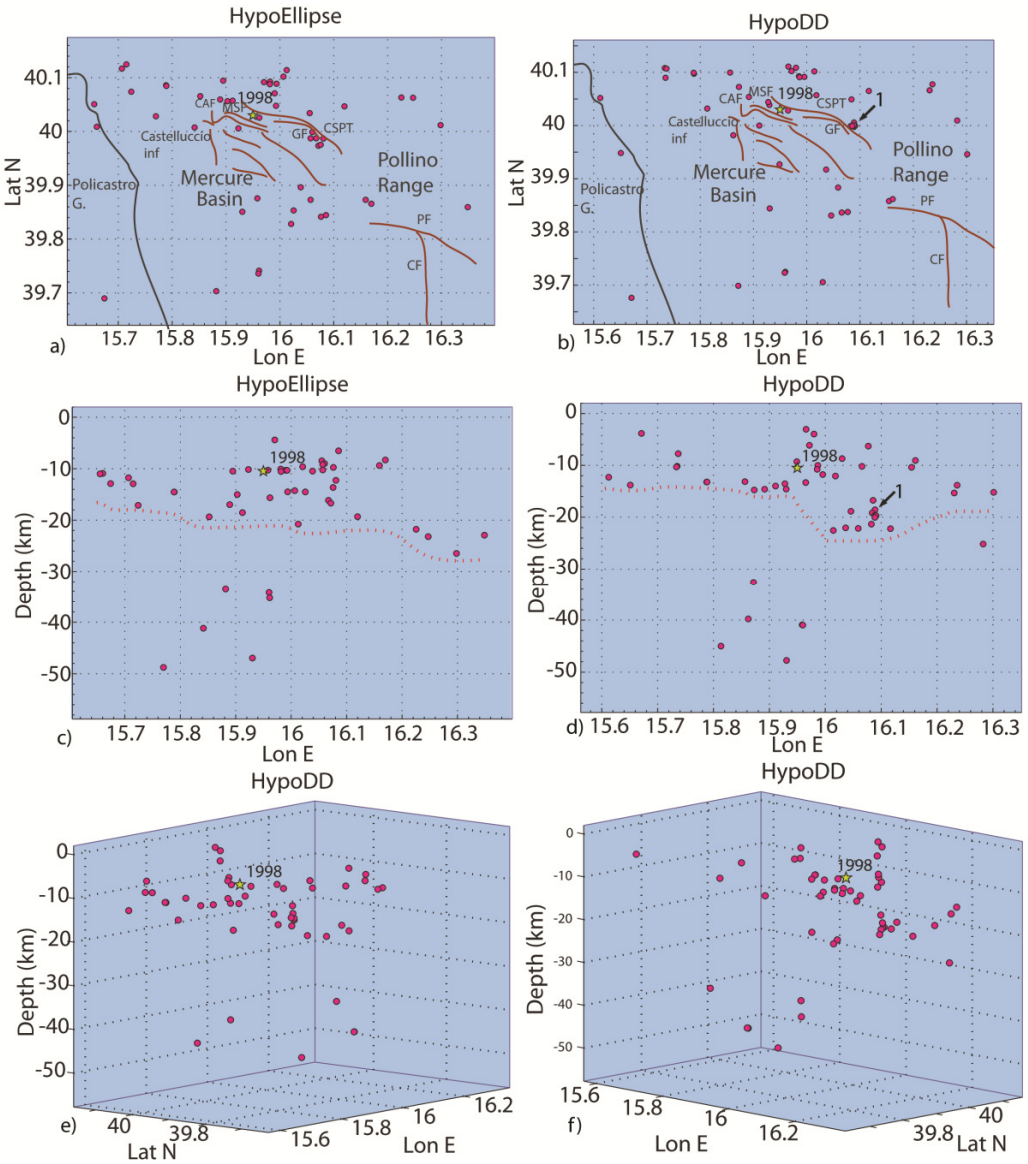

Figure 6.17: Map view of the hypocentral distribution and W-E cross-sections of the 50 events located with HYPOELLIPSE (a, c) and HYPODD code (b, d). 3D plot of the events located with DD method (e anti-apenninic, f apenninic observation directions respectively). Red dotted line trace variation in seismogenic base. Grey line: coastline. Yellow star: epicentres of historical earthquake. Numbers indicate clusters used to compute composite focal mechanisms. Brown lines refers, from the eastern, to Castello Seluci Piana Perretti Timpa della Manica Fault (CSPT), the Madonna del Soccorso F. (MSF), the Gallizzi F. (GF), the Castelluccio F. (CaF) (Brozzetti et al., 2009), Castrovillari F. (CF) and Pollino F. (PF) (Cinti et al., 1997).

This seismicity gap in the Pollino region is bounded to the north by Agri Valley historical earthquake and to the south by seismicity in the Crati Valley. The simplest interpretation for seismicity gaps is that they represent zones where the active deformation occurs aseismically because of unique local geological conditions even if they contain seismogenic faults. Geomorphic and paleoseismological investigations in this region show that the Castrovillari fault (CF) is a major seismogenic source (normal fault with NE-SW to E-W trending) (Brozzetti et al., 2009; Cinti et al., 1997) that could potentially fill the southern part of this gap. Moreover, Cinti et al., 1997 suggested that the fault might be ready to produce a large earthquake considering the minimum recurrence time expected for surface-faulting earthquakes (≈ 1200 years) and dated back three paleoearthquakes in the CF fault. Finally, few events, located to the SW of the Pollino Range, are deeper than 30 km and this seismicity is or could be related with the Southern Tyrrhenian subduction zone.

Figure 6.18: Composite focal mechanism computed for one cluster located in the Castelluccio area (see Fig. 6.18 b, d).

6.7 Group 6: Bradano foredeep

The seismicity of this group is located in the area of the Bradano Foredeep and the Apulian Foreland (40.40°-40.90° N of latitude, 16.00°-16.88°E of longitude). The Apulian is an emerged portion of the Adriatic microplate (Adria), representing the foreland-foredeep area of the stretch of the Apennine chain in Southern Italy. The interaction between the relatively rigid microplate and the contiguous more deformable domains is responsible for the intense seismicity affecting the chain area. The microplate plays the role of foreland for the more deformable bordering regions. Compared with the seismically active Apenninic belt, the internal part of Adria shows a much lower rate of seismic activity which is not negligible. This activity has been interpreted as intra-plate seismicity or as an effect of structural discontinuities (Favali et al., 1993; Renner and Slejko, 1994).

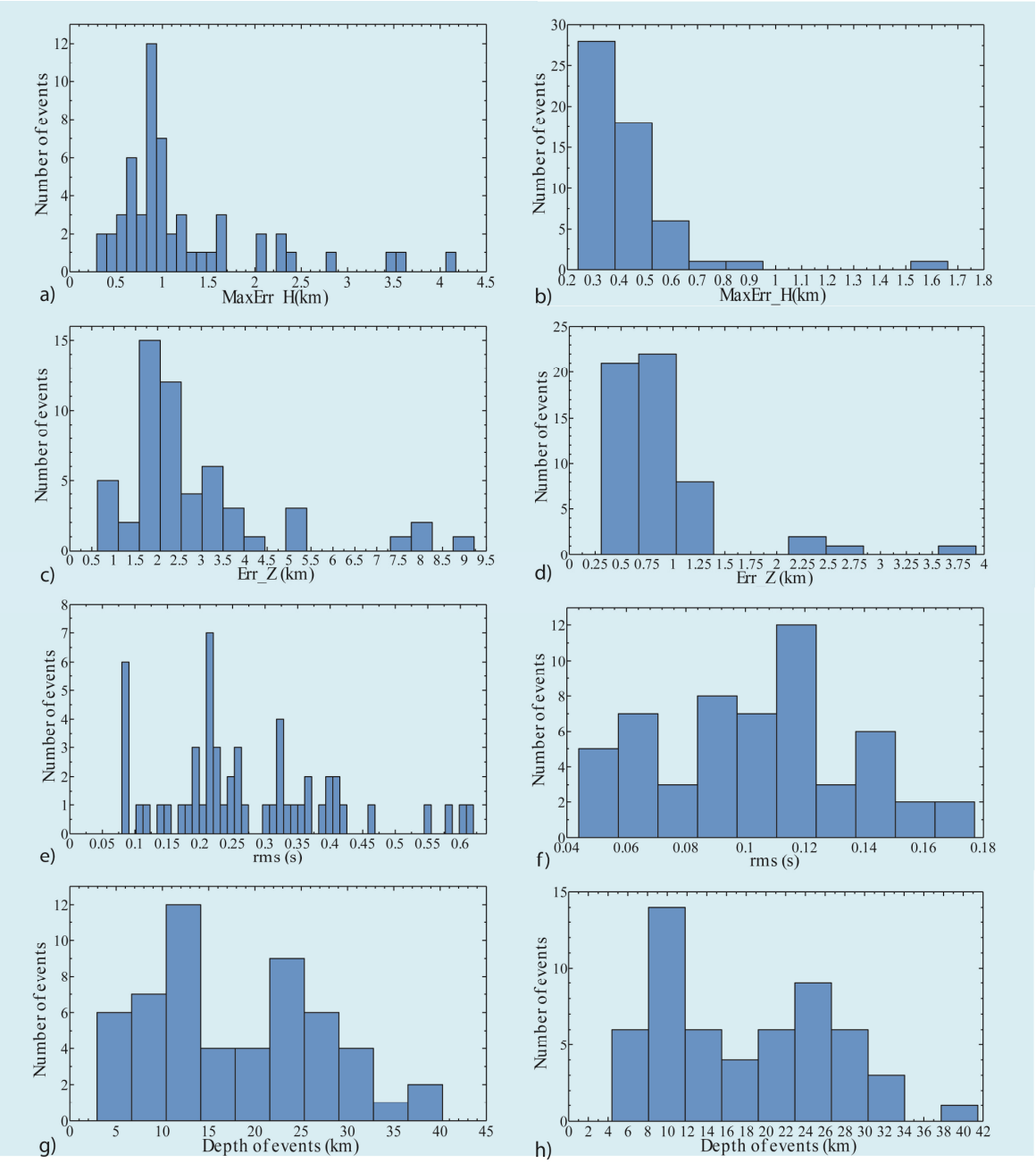

Figure 6.19: Rms residuals (seconds), horizontal and vertical errors (kilometres) and depth distribution of the 54 earthquakes located with HYPOELLIPSE (a, c, e, g) and HYPODD code (b, d, f, h).

In this area, I located 56 earthquakes (Fig. 6.3, blue dots) characterized by a more sparse seismicity. From historical records I know that this area was not hit by strong earthquakes. I relocated 54 events with the DD method improving the hypocentral locations (Fig. 6.20, see bradano.avi). Most of the microseismicity is located in the Bradano foredeep area. To the West, close to the eastern margin of the chain, the seismicity shows hypocentral depths between 9 and 30 km, while in the eastern part of the Bradano foredeep, it is characterized by deeper events (9-40 km depth range) (Fig. 6.20). However, the seismicity increases its depth in the southern part of the studied area and where it approaches the Apulian foreland (see Fig. 6.20 e, f). Other studies, based on different kinds of data, show this heterogeneity pointing out the presence of a lithosphere thickening in the Southern part of the Adria (Calcagnile and Panza, 1980; Doglioni et al., 1994); the crust-mantle transition is quite sharp to the north and gradual to the south (Venisti et al., 2005) and a belt of seismic activity crosses the Adriatic sea (Console et al., 1989). The deep crustal seismicity in the Bradano Foredeep and the Apulia Foreland area indicates the westward flexure of the Adria plate beneath the Apenninic belt related to the geodynamic process of Southern Italy and described in detail in the Chapter 1.

Another result is the cluster of shallow events (around 5-10 km of depth) to the east of Matera city: an area characterized by few events probably associated to small structures present in the area (Pieri et al., 1997).

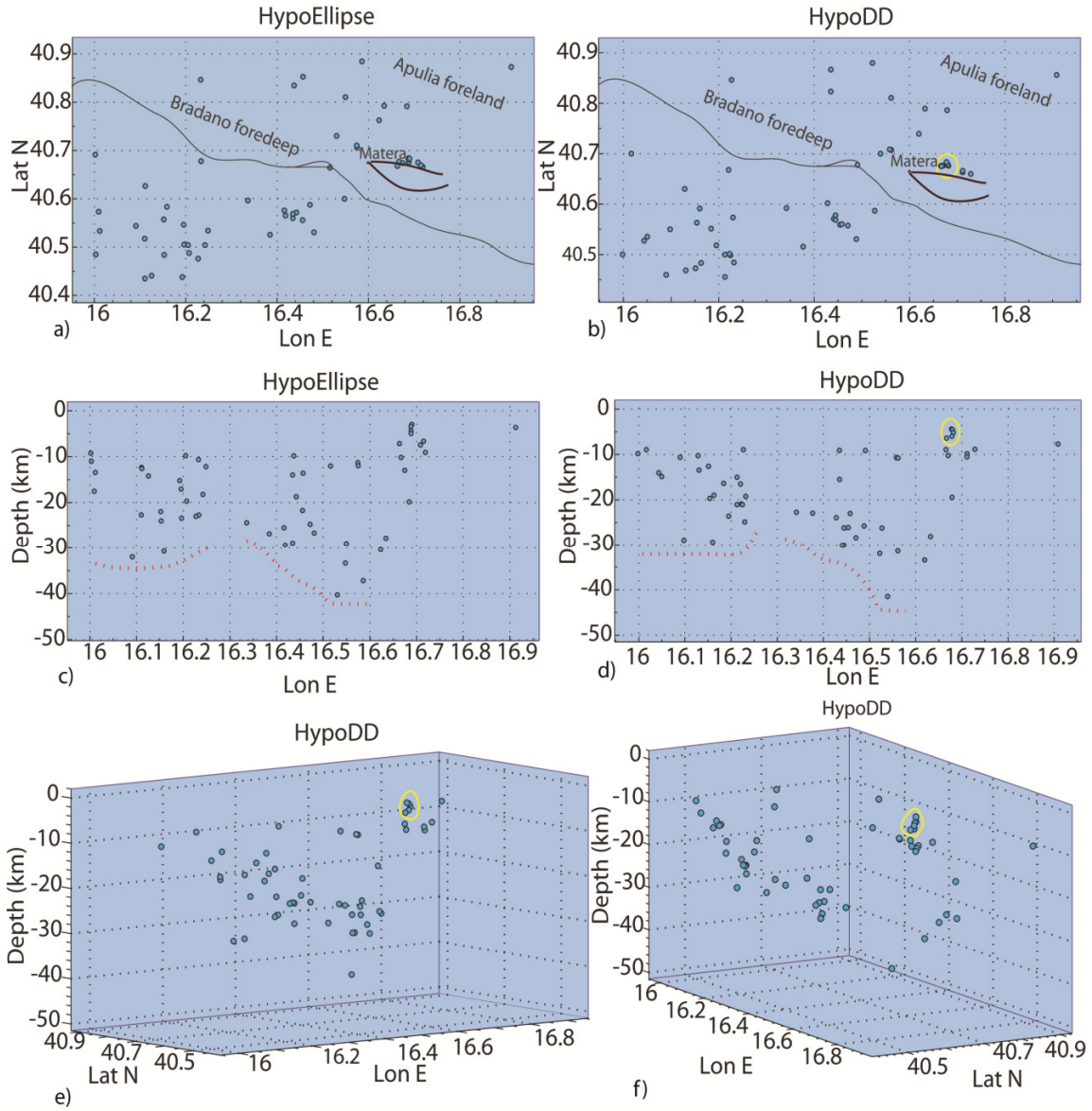

Figure 6.20: Map view of hypocentral distribution and W-E cross-sections of the 50 events located with HYPOELLIPSE (a, c) and HYPODD code (b, d). 3D plots of the events relocated with the DD method (e anti-apenninic, f apenninic observation directions respectively). Red dotted line trace variation in seismogenic base. Brown lines refers to small structures (Pieri et al., 1997). Yellow circle outlines the cluster of Matera.

6.8 Discussion

In this chapter I observed the noteworthy improvement of earthquake location thanks to the DD method. This improvement is more evident for restrict areas, especially for the sequences of Savoia di Lucania (Fig. 6.8), Moliterno (Fig. 6.14) and 11/2008 swarm in the area named Abriola-Pietrapertosa (Fig. 6.12). The accurate earthquake relocations in this study allowed me to retrieve a detailed picture of the microseismicity in the area of the Lucanian Apennine. Earthquakes are mostly located along the Apenninic chain and overlap the area characterized by the great active normal faults of the Southern Apennines.

The Apennines orogeny starts in the middle Miocene when a strong compressional tectonic phase began. While the long-lasting compressional regime caused progressive thrusting of different tectonic units corresponding to the different paleogeographic domains with strong crustal shortening, the deformation axis migrated eastward, toward external domains (Azzarra et al., 1993). The piled tectonic units that formed the Apennines deformed belt were in turn thrust over the Apulo-Adriatic foreland (Merlini and Mostardini,1986). At the end of this Pliocene the Southern Apennines was a highly complex imbricated thrust belt with abundant lateral and vertical lithologic transitions, the original geometrical framework being completely dissected and hidden by orogenic transport (Pantosti and Valensise, 1990). Finally, during the Plio-Pleistocene, a neotectonic distensive phase caused the regional raising and fragmentation of the brittle limestone platform (Ogniben, 1975). The Apennine crust undergoing extension produced extensive volcanism on the Tyrrhenian margin of the Chain: the NW-SE trend of extension migrated toward the NE. Subsequently, the region was further fragmented into several isolated blocks identified by large stratigraphic throws or gaps. The new tectonic trends often follow older fault zones associated with the compressional phases. This characteristic plays an important role at all scales of observation in the central and Southern Apennines. The structure setting of the epicentral areas reflects the complex history of the Apennines that is dominated by thrusting of highly deformed nappes toward the NE and NNE and by widespread normal faulting. In this study I underline a correlation between the tectonic phases and the rheological stratification of the analyzed area, thanks to the seismicity distribution and the computed composite focal mechanisms. I observed that the still active NE-SW extension is responsible for the formation of the NW-SE striking faults that dissect the inner sectors of the chain where the most energetic and majority of the events

occurred in the Southern Apennines (Fig. 6.5, 6.8, 6.9 Potentino1 and Potentino2; Fig. 6.14, 6.15 Moliterno 2, 3, and Fig. 6.17, 6.18). Moreover, the zone where the Apennine units overthrust the Apulian crust during the Late Pliocene-Middle Pleistocene is characterized by a deeper crustal seismicity due to E-W fault zones inherited from previous tectonic phases and reactivated by the present strike-slip tectonic regime, but located at deep crustal levels (Boncio et al., 2007; Valensise et al., 2004, Barba et al., 2009). These structures are outlined by my results about the Potentino area (Fig. 6.8, 6.9 Potentino4, Potentino5). The eastern portion of this zone is characterized by relatively deeper events which appear anomalous compared to the adjacent Irpinia seismicity. It is explained by crustal rheology which consists of a strong brittle layer at mid crustal depths sandwiched between two plastic horizons (Fig. 6.11). The seismicity located in the Southern studied areas as Moliterno and Castelluccio is mainly associated to the NW-SE with SW-dipping of EAFS and CSPT fault except the reservoir induced seismicity of Moliterno cluster located to the SW of Pertusillo lake (see Fig. 6.14, Fig. 6.15 Moliterno1, Moliterno2, Fig. 6.17, 6.18). The low-energy and scattered seismicity in the Bradano foredeep group can be associated to Quaternary uplift of the Murge that is growth of several normal and transestensional faults (Pieri et al., 1997).

As regards the depth of the seismogenic layer, it is around 20 km beneath the Apenninic chain and between 30 and 40 km below the outer margin of the chain and the Apulia Foreland (deeper seismicity). This eastward deepening indicates a deeper boundary between the brittle and ductile crust beneath the external margin of the Lucanian Apennine and the foredeep, compared to that beneath the chain itself. This increasing depth of the seismogenic layer is associated with the westward flexural bending of the Adriatic continental lithosphere beneath the Apenninic chain during the Quaternary.

Finally, the studied microseismicity beneath the Chain could be explained with the post-seismic relaxation process related to the strong earthquakes that hit the Southern Apennines. In particular, Azzara et al., 1990 proposed that the 1990 Potenza sequence is close to the SE of the Irpinia fault and this could be regarded as a possible evidence of the interaction between adjacent fault segments. Moreover, the scarce microseismicity observed in some sectors along the Apenninic chain could be related with active fault segments presently locked where possible large earthquakes might be expected in the future. Considering the “silent area” of the Pollino range, where I observed a seismicity gap, a seismicity hazard assessment,

based only on the historical record, may be not completely reliable. In fact, Cucci et al., 1996 recognized paleoearthquakes in this zone and estimate the expected minimum recurrence time ≈ 1200 years deducing that the CF fault might be ready to produce a large earthquake. Also the Mercure area must be considered comparable, in term of seismic hazard, to the Pollino area where according to the Brozzetti et al., 2009 hypothesis, the 1998 Mercure earthquake would have only activated a small portion of such a plane of the CSPT fault.

Chapter 7

Swarm of 11/2008

During November 2008 the seismic stations of SeSCAL experiment recorded a swarm in an area that I called Abriola–Pietrapertosa. The importance of this swarm is in the area that it hit (40.53-40.57 N and 15.82-15.88 E). It is situated between the maximum intensity areas of two of the most destructive earthquakes reported in the Italian seismic catalogue: the Val d'Agri earthquake (1857) and the Irpinia event (1980). This area is not associated with known historical events and for this reason is currently object of investigation as a potential seismic gap (Lucente et al., 2005).

I carried out a detailed analysis using methodologies mentioned above and the waveform cross-correlation technique to better constrain the hypocentral locations. Thanks to the composite focal mechanisms analysis I obtained interesting information about the tectonics of this area.

7.1 HYPOELLIPSE and HYPODD locations

I analyzed in detail the November 2008 swarm shown in Fig. 7.1. Initially, this swarm was constituted by 41 events with $1.0 \leq M_L \leq 2.9$. I located 37 events using HYPODD code and obtaining a denser cluster and a better hypocenter distribution with respect to HYPOELLIPSE locations. I observe that the events: mapped in the detailed area of ~ 2 km x 2 km in Fig. 7.1, have depths between 10-18 km and a subvertical distribution. Moreover, I observe a denser and deeper cluster that was analyzed computing the waveform cross-correlation to better constrained hypocenter locations.

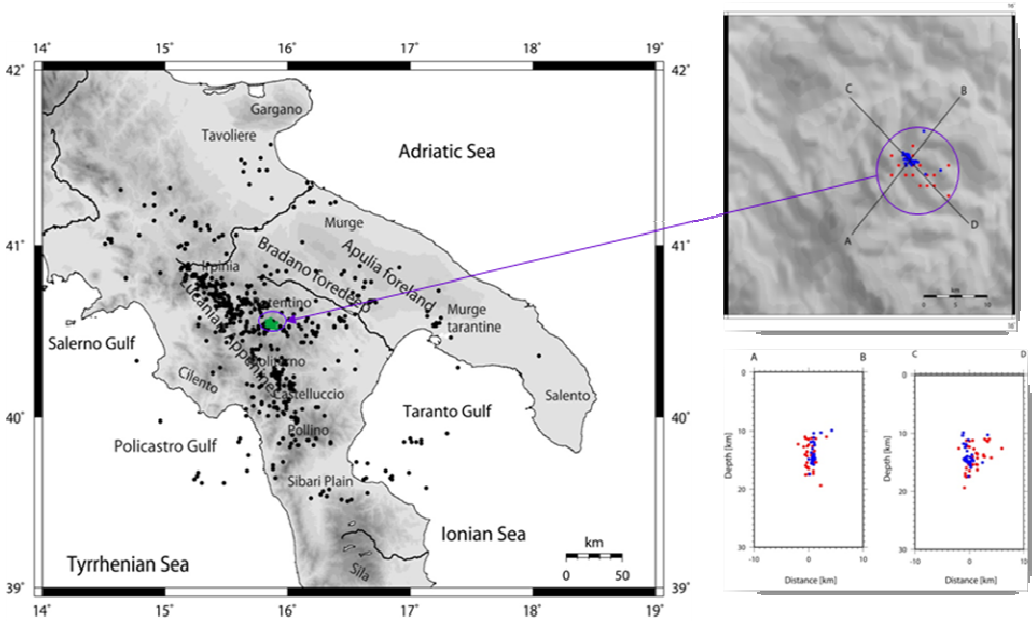

Figure 7.1: Map of the HYPOELLIPSE locations of all studied events (black dots) and of 11/2008 swarm (green dots) (left hand). Map of the swarm with HYPOELLIPSE (red dots) and HYPODD locations (blue dots).

7.2 Waveform cross-correlation

I could further improve location precision by improving the accuracy of the relative arrival-time readings using the waveform cross-correlation method. I used a MATLAB software GLOBALLOCALIZER developed by Pignatelli et al., 2008 for more details, see Appendix F) for searching of small aftershocks subsequent to an underground explosion. This code was modified for my use. The time difference between waveforms is computed with respect to a reference station after choosing a reference event.

Generally, two earthquakes produce similar waveforms at a common station if their source mechanisms are virtually identical and their source is co-located so that signal scattering, due to velocity heterogeneities along the ray paths, has small influence. This assumption is valid up to some frequency threshold. The time difference between the two arrivals is taken to be the time shift of one record with respect to the other that yields the maximum of the correlation function in the time domain. Correlation (R) between two waveforms is defined as (Taylor, 1982):

$$R = \frac{N\sum_{i=1}^{N} X_i Y_i - \sum_{i=1}^{N} X_i \sum_{i=1}^{N} Y_i}{\sqrt{\left[N\sum_{i=1}^{N} X_i^2 - \left(\sum_{i=1}^{N} X_i\right)^2\right]\left[N\sum_{i=1}^{N} Y_i^2 - \left(\sum_{i=1}^{N} Y_i\right)^2\right]}} \qquad (7.1)$$

where X_i and Y_i are the samples of the digital waveform segments and N is the number of samples of the correlation window. If R assumes the maximum value of 1 then the two seismograms are identical, while if they are different then they are associated with lower cross-correlation values. This program was built in a way to interactively select a window size. It is known that a small window is associated to a greater correlation because the similarity between wave-forms is easier. I selected a window size of 0.3 s surrounding the first arriving P-wave. I used a number of 300 steps starting 1 s before the first onset for all waveforms (see Fig. 7.2).

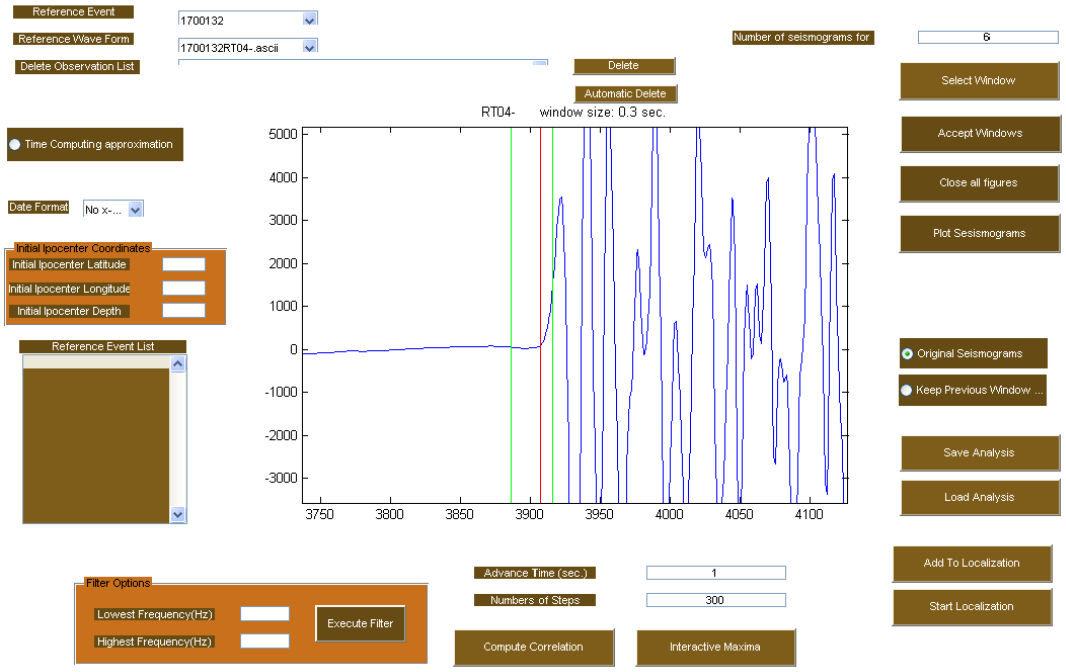

Figure 7.2: An example of GLOBALLOCALIZER GUI program. In this window is shown a zoom of the waveform associated to the reference event 1700132 recorded by the RT04 SeSCAL station. Red line is the P-arrival time hand-picked and green lines represent window borders of 0.3 sec size.

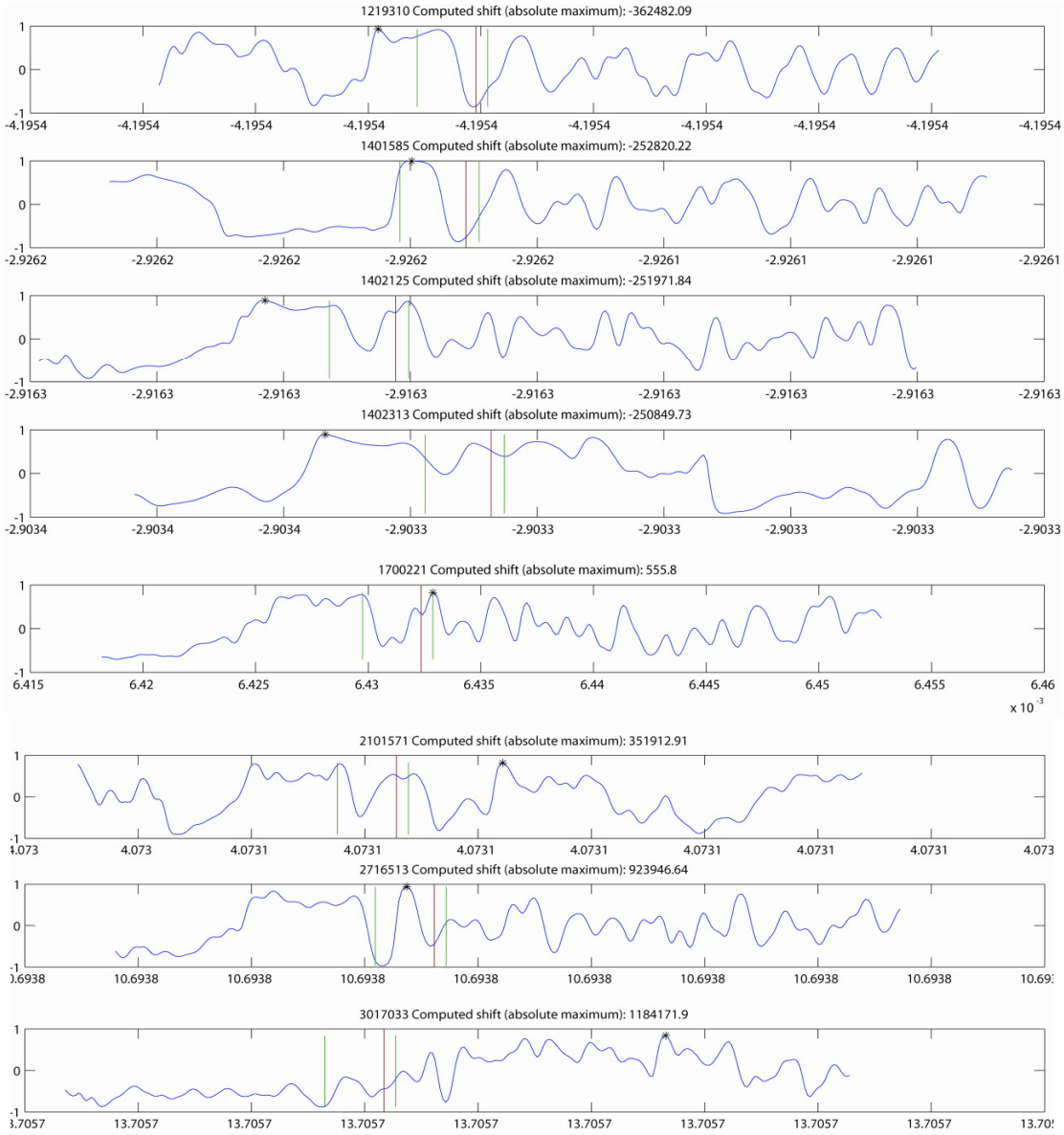

Figure 7.3: Cross-correlation functions displayed by the GLOBALLOCALIZER GUI. Stars are automatic absolute maximum values of cross-correlation function for RT04 waveforms and numbers 1219310, 1041585, 1402125, 1402313,…, are event names. The computed shift is the corresponding time difference obtained.

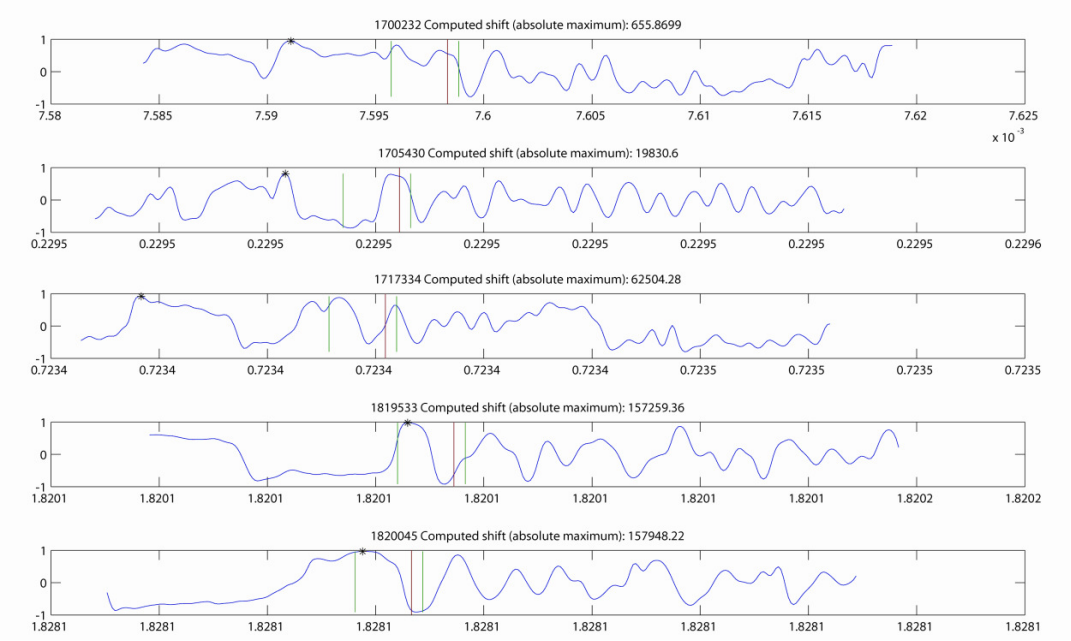

Figure 7.3: (continued).

I can choose to manually select the maximum of correlation functions or to accept the absolute maximum value computed automatically. Sometimes, I selected a maximum manually when the cross-correlation value was a little different and nearer to picking value. The P-waves have a cross-correlation coefficient > 0.7.

I relocated this cluster of 22 events using both HYPOELLIPSE (catalogue data) and cross-correlation data as input locations (see video swarm.avi). I observe a noteworthy improvement of earthquakes distribution using the DD method. The events result clustered and with depth between ~13 and ~16 km (Fig. 7.4 a, b c, d, e, f and Fig. 7.5 j, k, l). Analyzing the results obtained considering only catalogue data as input I observe an E-W distribution of epicentres in the east side and a small cluster northern. This result is slightly more visible in the locations obtained applying the cross-correlation data (Fig. 7.4 b, c). Moreover, the hypocenters deepen from NE to SW direction (Fig. 7.4 e, f, k, l). I observe that my relocations are characterized by a large number of events with rms included in the 0.18–0.30 s interval. Most of these events show maximum horizontal errors (MaxErr_H) smaller than 0.35 km and vertical errors (Err_Z) smaller than 0.6 km (Fig. 7.5 c, f, i).

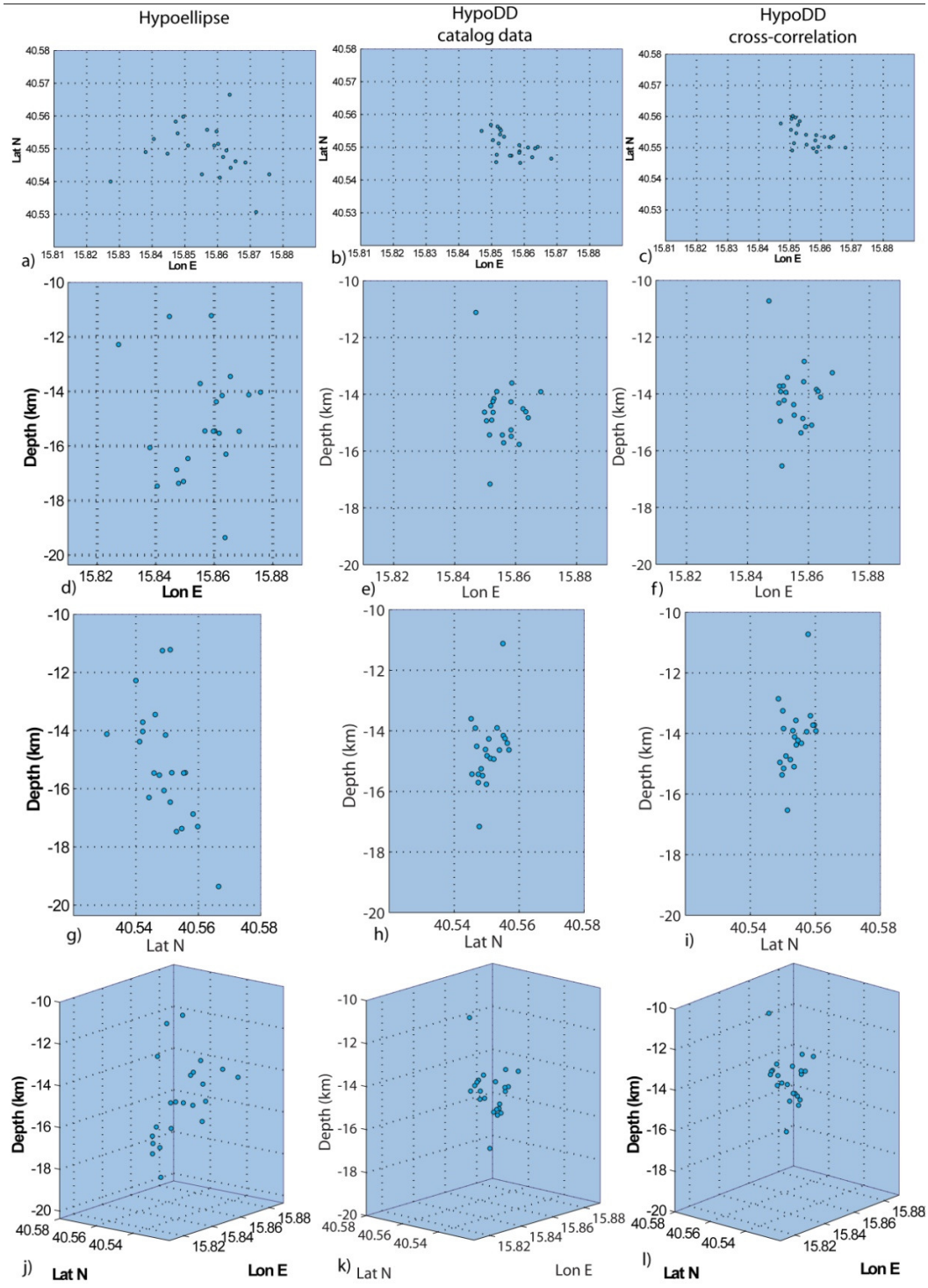

Figure 7.4: Event relocation distributions. (a), (b) and (c) Epicentral distributions of the 22 events located with HYPOELLIPSE, HYPODD using solely catalogue data, and HYPODD with catalogue and cross-correlation data. (d), (e) and (f) Hypocentral distributions section E-W. (g), (h) and (i) Hypocentral distributions section N-S. (j), (k) and (l) Hypocentral distribution in the space with the observation point along anti-Apenninic direction.

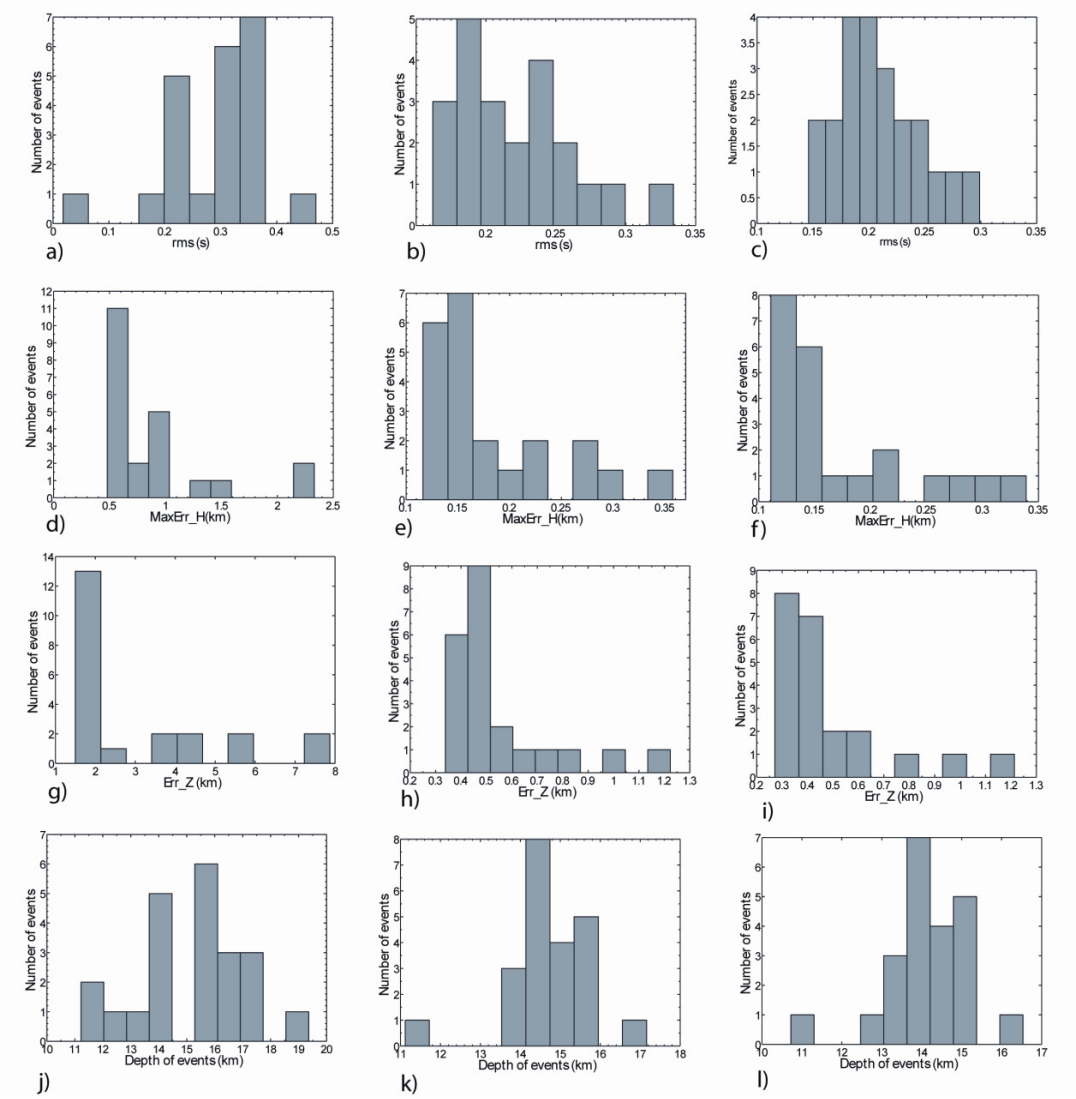

Figure 7.5: Event relocation statistics. (a) rms, (d) maximum horizontal error (MaxErr_H), (g) vertical error (Err_Z), and (j) depth distribution of the 22 studied earthquakes located with HYPOELLIPSE. Location error statistics for the same dataset relocated with HYPODD using HYPOELLIPSE data (b), (e), (h) and (k). (c, f, i and l) Location error statistics of events relocated with the HYPODD code using catalogue and cross-correlation data.

7.3 Composite focal mechanisms

I computed composite focal mechanisms (see introduction to Chapter 6) to better assess the tectonics of this swarm. After careful analysis, I distinguished two principal areas with different tectonics. One is identified by a green line in Fig. 7.6 with a normal focal mechanism and a NW-SE strike. The second is related to a very small group of events located

to the NW of this swarm (Fig. 7.2 c, d 40.56 N 15.85 E, -14 km depth) and characterized by a normal focal mechanism with a NE-SW strike (see magenta line in Fig. 7.6).

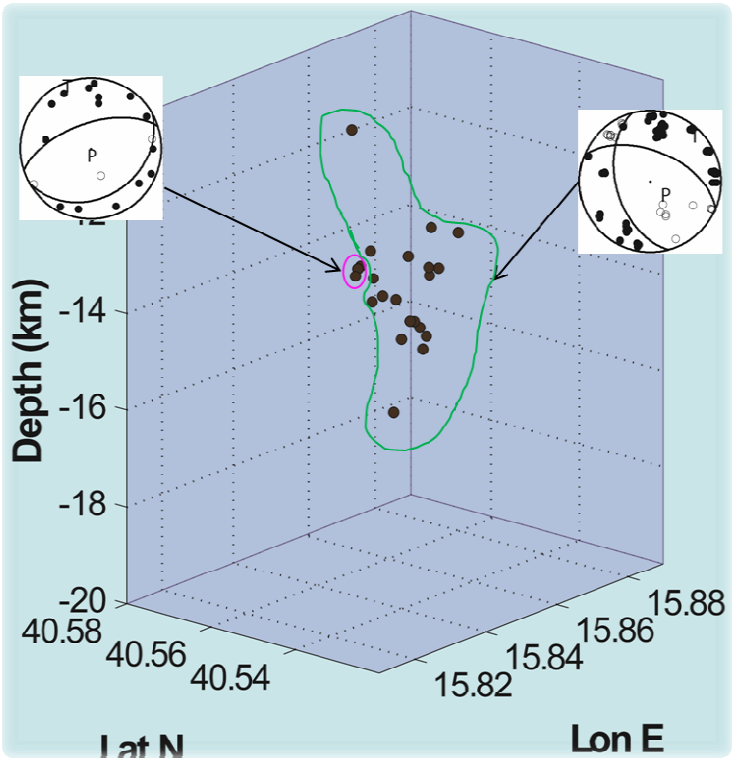

Figure 7.6: Composite focal mechanisms obtained for the two tectonically different areas contouring by magenta and green lines. Brown dots are the hypocenters.

7.4 Discussion

Detailed analysis of the Swarm of 11/2008 is very important for the comprehension of the seismotectonics of this area. It is located between two areas hit by historical and disastrous earthquakes: the Irpinia region to the north and the Val d'Agri area to the south. For this reason it is currently subject of investigation as a potential seismic gap.

I observe two different seismotectonic settings (Fig. 7.4, 7.6):

1. Events located close to ~ 45.56 N, ~ 15.85 E and 14 km depth characterized by a NE-SW normal fault;

2. A larger group (~40.55N, 15.85-15.87E) E-W elongated that deepen from NE (~ 13 km depth) to SW (~ 15 km depth) and a NE-SW composite focal mechanism.

The structural significance of the NE-SW faults, as that I observed, is poorly known. These faults type was generally interpreted by large scale geodynamic models (Oldow et al., 1993; Ferranti et al., 1996; Doglioni, 1996) whose activity mainly developed during pre-Quaternary times (~1,8 million of years), as low-angle, normal faults related to the progressive longitudinal extension of the Apenninic chain axis. Finally, coherently with Milano et al. (2005), I underline that the studied Apennines sector is affected by heterogeneous deformation being characterized by both NE-SW (strong earthquakes) and NW-SE (low energy events as swarms) extensions. Moreover, the NE-SW elongated structures are generally considered to act as a barrier to the propagation of rupture of the active NW-SE striking faults system (Di Bucci et al., 2002). Another attractive hypothesis is that it might be a potential seismic gap area, where the probability of future ruptures is higher than in surrounding regions, also for the static stress increase caused by the two above mentioned earthquakes (Lucente et al., 2005). Therefore, the seismotectonic picture of this transition is more complex than that proposed up to now and cannot be interpreted in light of these few pieces of information.

Conclusions

The new dataset of background seismicity examined in this study is a further contribution to the comprehension of the seismogenesis and state of stress of a tectonically complex region, such as the Southern Apennines, characterized by a very high seismic hazard. The significant improvement in the seismic monitoring of the area, reached using both the permanent Italian national network and two temporary arrays of three-component stations, allowed me to obtain a more detailed picture of the seismotectonics of the region, including the Southern Apennines foreland which had been generally considered substantially aseismic. As already emerged in previous studies, the background seismicity occurs mostly beneath the mountain belt where the main seismogenic structures are located (Maggi et al., 2009, Frepoli et al., 2011). The research conducted in the present Thesis shows that this microseismic activity is substantially clustered at the borders of silent fault segments beneath the Apenninic chain. Here the transition brittle–ductile is inferred between 20 and 25 km from the bottom limit of the located seismicity. This brittle-ductile boundary is located at around 40 km beneath the foredeep and foreland areas. I also suggest that the scarce background seismicity observed in some sectors along the Apenninic chain could be related to fault segments presently locked (e.g. Castelluccio, Potentino and Abriola-Pietrapertosa area) or to the postseismic relaxation process (e.g. Irpinia area) where possible large earthquakes might be expected in the future. I also observed a structure NE-SW oriented in the Abriola-Pietrapertosa area (activated in the swarm occurred in November 2008) similar to that observed also in other areas of the Apenninic chain. The NE-SW elongated structural discontinuity could be considered to act as a barrier to the propagation of a possible rupture of an active NW-SE striking fault system. The events located in the area of Bradanic foredeep and Apulia foreland are associated to the Murge uplift and to the small structures present in the area. The results coming from the present-time stress field studies, as shown in this work, give important contributions to

seismotectonic zoning and seismic hazard assessment. A detailed earthquake distribution and the active stress map might suggest the mechanism by which faults are more likely to rupture in future events, especially in regions where active faults have no surface expression as in some areas of Southern Italy. In fact, many moderate, although hazardous, earthquakes occur on blind faults in the Italian region, with large repeat times of the order of thousands of years. For this reason it is important to integrate the stress field data with historical information and with seismicity patterns determined from instrumental monitoring in order to extend the capability of assessing seismic hazard (Frepoli et al., 2011).

Some of the analysis techniques described in this thesis were also applied to the greater Rome area improving my understanding of those aspects that are useful for hazard analysis in an area of very dense population and rich of architectonic assets (Frepoli et al., 2010).

Appendix A

Program VELEST

VELEST is a FORTRAN77 program that was used to compute 1D velocity models for earthquakes location and as initial reference models for seismic tomography (Kissling, 1998; Kissling et al. 1994).

This program solves in "simultaneous mode" and in "single-event-mode". In the first mode it is used to define a 1D velocity model and station corrections and performs the Joint-Hypocenter-Determination (JHD) described in Section 2.2.2. The second is used to locate single local earthquakes, blasts and shots. In both modes the forward problem is solved by ray tracing from hypocenter to receiver. It computes the direct, refracted and eventually the reflected ray using 1D model.

The solution is obtained iteratively and one iteration consists of solving the complete forward and inverse problem once, as described in the flow-chart of Fig. 1.

The input files are:

1. Control parameters (*.cmn). The computation of the 1D velocity model required multiple runs to select and test the appropriate values.
2. station list (*.sta)
3. initial 1D velocity model (*.mod)
4. initial data location (*.cnv)

The output file is a main print output (*.out)

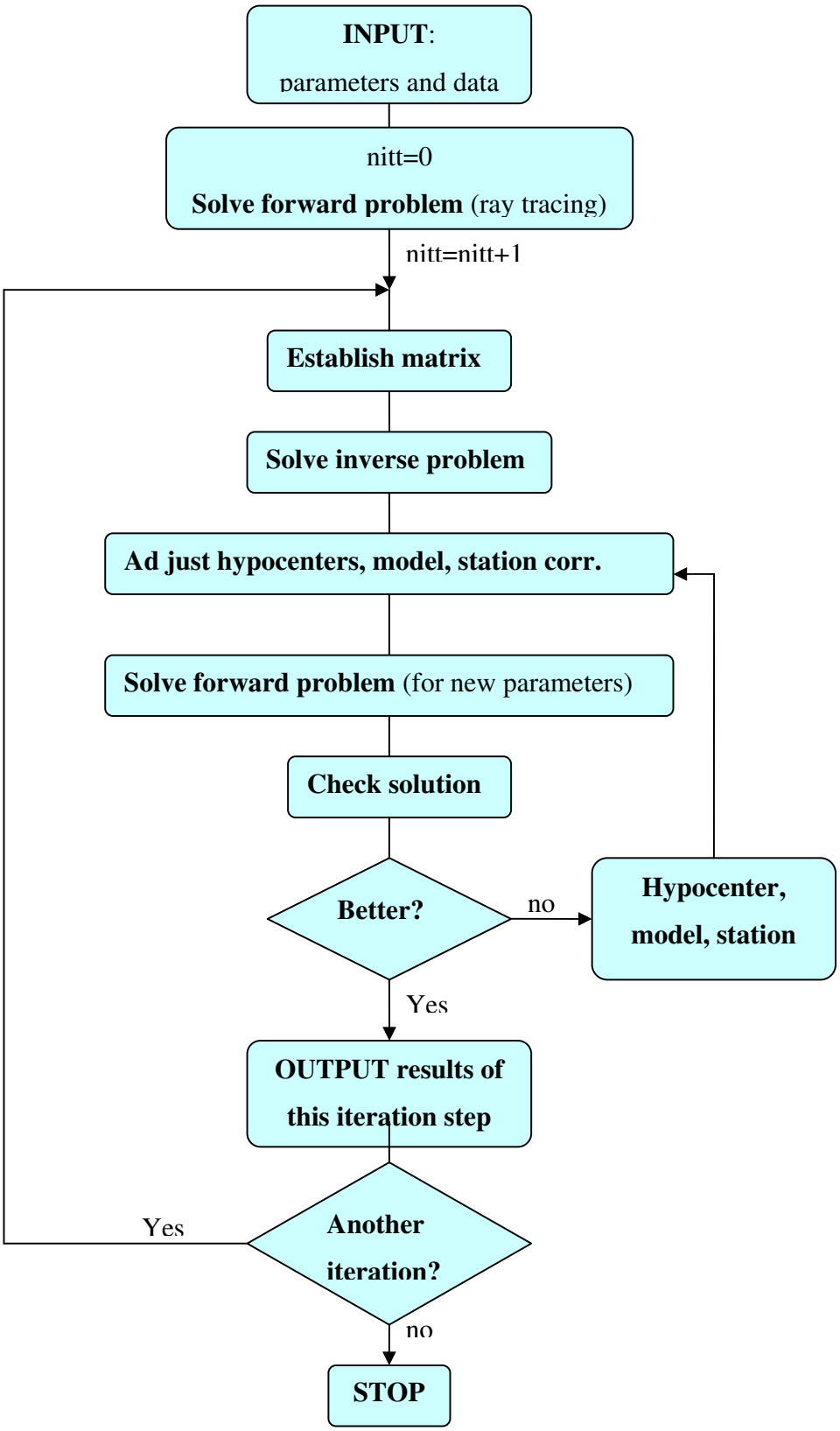

Figure 1: VELEST procedure (modified from Kissling, 1995).

Computation of 1D-velocity model (simultaneous mode)

This is a coupled hypocenter-velocity model problem and consists of the hypocenters, the velocity model, and station corrections. The differences between calculated and measured travel-times are called the misfit (or residuals) of the solution. Consider any possible combination of hypocenters, velocity model, and station corrections be rated by its RMS misfit two situations are possible:

1) A well-posed problem that would only have one solution with minimal RMS (Figure 2a);
2) Several local RMS minima occur (case of the coupled problem with local earthquake data Figure 2b). In such situations the solution obtained by any iterative algorithm strongly depends on the initial model and initial hypocenter locations.

You do not a priori know the RMS function and, therefore, you must search for different solutions with minimal misfit (RMS) by varying initial models and hypocenter locations within reasonable but large bounds. Thus, the calculation of a Minimum 1-D model amounts to a TRIAL-AND-ERROR process (for different initial models). Since VELEST does not automatically adjust layer thickness, the appropriate layering of the model must be found by a trial-and-error process.

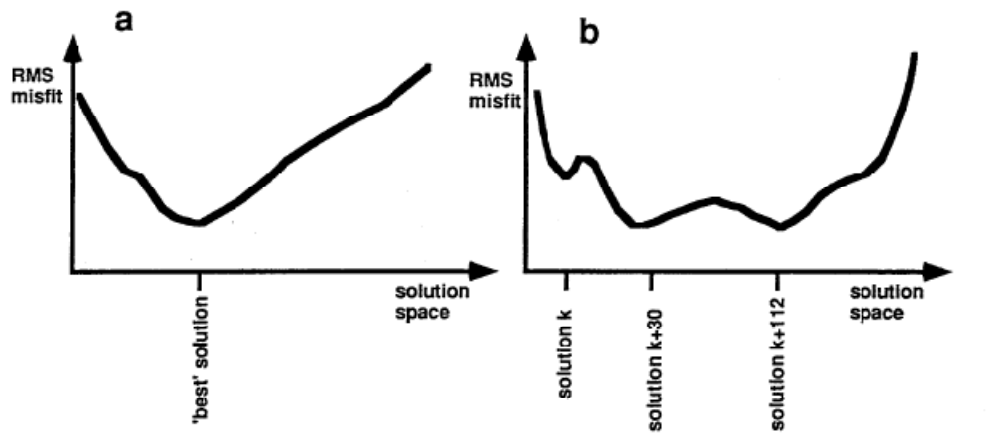

Figure 2: Quality estimate of solutions to the coupled problem. a) Simple case with unique "best fit" solution. b) Normal case with several local minima of RMS misfit (Kissling, 1995).

Thus the calculation of a Minimum 1-D model normally starts with:

Finding an appropriate model layering.

Introduce layers according to refraction models or literature models. Put the trial layer thickness at 2 km for shallow crustal levels and increase layer thickness with increasing depth to about 4 to 5 km at Moho depth.

Setting appropriate control parameters

Begin without low velocity layers (LOWVELOCLAY=0) since they have strong effects on the ray paths and, thus, they increase the non-linearity of the problem. Set damping of velocity-model VTHET=1.0, damping of station-corrections STATHET=0.1, and the hypocentral damping parameters to 0.01.

Set INVERTRATIO[1] to 1 and allow between 5 and 9 iterations. Save this data for later testing (see below).

Initial values and first inversions

Set velocity damping parameters (VDAMP) in Model File (*.mod) all equal to 1.0.

INITIAL HYPOCENTERS: Use the locations of best routine location procedure. If your trial velocity model is largely different from the one used to obtain initial hypocenter locations you might want to try two VELEST runs, one with INVERTRATIO=1 and one with INVERTRATIO=2 and do not vary any other parameter. You may then use these final hypocenter locations and station corrections as initial parameters for the next run of VELEST where you let the model float again.

INITIAL STATION CORRECTIONS: Set all of them to zero.

Probing the solution space

Normally, you have a fairly good idea about the probable average crustal velocity and about the Moho depth. Try several initial velocity models. To probe the dependence of the solution on the initial model one should try at least three different initial velocity models for any model geometry (layer thickness): one with extremely low crustal velocities, one with

[1] In simultaneous mode VELEST may either invert for all hypocenters and model (with station corrections) parameters [type A] or invert only for all hypocenters [type B]. If INVERTRATIO is set to 1, every iteration is of type A. If it is set to 2, every second iteration is an inversion type A.

extremely high and one with intermediate crustal velocities. You will also see if the problem is reasonably well determined by the data. You may then decide on the best model layering based on the results of the previous VELEST runs and based on the depth distribution of the earthquakes. Choose a simple model by combining layers where velocities are very similar, unless you want to mimic a gradient.

Note: The superficial layers are mostly subvertically and bottom layers are mostly subhorizontally penetrated. Therefore, the resolution in these layers is generally lower than in the central layers that contain the hypocenters.

Appendix B

Program HYPOELLIPSE

HYPOELLIPSE (Lahr, 1989) is a code for determining the hypocenters of earthquakes and the ellipsoid that encloses the 68% confidence volume. Travel times are determined from a initial layered-velocity model or from a previously generated travel-time table. Arrival times for the first arrival of P- and S-waves can be used in the solutions. Each arrival can be weighted according to the reading clarity, the epicentral distance to the station, and the deviation of its residual from the mean. The hypocenter is found using Geiger's method described in Chapter 2 section 2.2.1to minimize the root-mean-square (RMS) of the travel-time residuals.

In the my case I used a stratified velocity model with a constant velocity in each layer. The three variables to be specified are: the P-wave velocity (km/s), the depth to top of layer (km), and the $^{V_P}/_{V_S}$ ratio (Table I).

Velocity	real	real	real

Table I: Format of velocity model.

The $^{V_P}/_{V_S}$ ratio can be specified for each layer or defined in the input control file containing the options selected for the location process (Table II).

The input files essential to run the program are:

- velocity model (Table I);
- first arrival of P- and S-waves;
- station list;
- options select (Table II);
- options record.

Test No.	Default Test Value	Description
1	1.78	Ratio of P-wave to S-wave velocity
2	5.0	P-phase velocity for elevation corrections (km/s). If the value is negative, make no elevation corrections. If zero, use first-layer velocity for elevation corrections. If greater than zero, use this for elevation corrections. In the latter case, value must be less than first layer P-phase velocity. Used with computed models if TEST(8) = 0 and with travel-time tables.
Trial Location		
3	0.0	First trial latitude (degrees). North positive. If TEST(3) or (4) = 0, then ignore. See 2.2.12 for use.
4	0.0	First trial longitude (degrees). West positive. If TEST(3) or (4) = 0, then ignore. See 2.2.12 for use.
5	-99.0	Used for first trial depth (km with respect to sea level) unless equal -99 or unless Global Option is in effect. See 2.2.12 for use.
6	0.0	RMS may optionally be computed at additional points on a sphere surrounding the final hypocenter. This is the radius of the sphere (km). If zero, no auxiliary RMS values are calculated. If negative, and if one or more points have lower RMS than the final solution, continue iteration once starting at point with lowest RMS value.
7	10.0	Focal Mechanism Plot. Minimum number of first motions for a first-motion plot to be made. If negative, make a second plot showing station codes.
8	0.0	Elevation of top of computed models with respect to sea level (km).
9	0.0	If not zero, reset negative depths in summary record cols. 32-36 to -00. True depth below (positive) or above (negative) sea level always given in cols. 113-117 of the summary record..
Distance Weighting		
10	0.0	Apply distance weighting on this iteration. See also TEST(11) and (12).
11	50.0	XNEAR = Greatest distance (km) with assigned weight multiplied by 1.0
12	100.0	XFAR = Least distance (km) with assigned weight of multiplied by 0.0. See also TEST(46).
13	50.0	Azimuthal Weighting. Apply azimuthal weighting on this iteration. Warning: this option has not been tested.

Table II: Options select. Options that it is possible to change (from Lahr, 1989).

		depth with respect to sea level, continue at a depth half way between this depth and the surface of the velocity models. See also TEST(42).
28	0.0	To fix the hypocenter on a plane, set absolute value of this equal to azimuth of plunge line of plane (0° to 360° measured clockwise from North). If negative, then a free solution will be determined starting at the best location on the plane. See also TEST(30) and TEST(47).
29	-0.1	If TEST(29) is positive, the standard error of readings assigned zero weight-code is set equal to the RMS residual, unless there are zero degrees-of-freedom or the estimated reading standard error falls below TEST(29). In that case TEST(29) is used for the standard error of the readings. If TEST(29) is negative, the standard error of the zero weight-code readings is always set equal to minus TEST(29). See also 2.2.3.13.
30	0.0	Used if TEST(28) is positive, causing solution to be fixed on a plane. If positive, this is dip of plunge vector of the plane. See also TEST(28) and TEST(47). If negative, then fix epicenter and solve only for depth and origin time, ignoring TEST(47).
Duration Magnitude Parameters (See also TEST(40) and (43))		
31	-1.15	C1, constant
32	2.0	C2, *log((F-P) * FMGC)
33	0.0	C3, *DELTA
34	0.0	If not equal 0, scale the normal equations.
35	0.001	Minimum damping of normal equations.
36	100.0	Maximum first trial depth (km), if computed from P-arrival times.
37	3.0	If termination occurs before this iteration, set iteration number to this and continue. Prevents iteration from stopping before all forms of weighting have been applied. After this iteration, velocity and delay models will not be changed by the SELECT DELAY (2.2.3.6) option.
38	0.0	If 0, use of S arrivals depends upon S-data indicator on INSTRUCTION record. If 1, locate all with and without S arrivals. If 2 locate all with S arrivals. If 3, locate all without S arrivals. If 4, fix all solutions at starting hypocenter, and use S arrival. If negative, use S arrivals only to fix origin time.
39	1.0	Multiply the S and S-P weight-code weights by this factor.

Table II: (continued)

Test No.	Default Test Value	Description
40	0.007	Duration magnitude parameter C4; multiplies the DEPTH (see also TEST(31)-(33) and TEST(43))
41	0.0	If this equals 1, PRINT OPTION is greater than or equal 1, and SUMMARY OPTION equals plus or minus 1, then write a new SUMMARY record after each iteration.
42	75.0	Global solution option: deep starting depth (km with respect to sea level). See also TEST(27).
43	0.0	Duration magnitude parameter C5; multiplies (log ((Γ-P) *FMGC)**2) (see also TEST(31)-(33) and TEST(40))
44	0.0	If 1, rerun "debug events" again (See 2.2.3.10) with critical stations; if 2, make a second run for all events with critical stations See note below for definition of critical stations.
45	0.1379	X-scale factor for focal mechanism plots. Adjust for printer in use. (See 2.3.9)
46	0.0	If TEST(46) not equal 0.0, distance-weighting constant XFAR (see TEST(12)) will be set to a minimum of 10 km beyond the distance of the TEST(46)th station. If TEST(46) is negative, then any station beyond XFAR that would reduce a gap greater than 60 ° by 30° or more is given a distance weight of 0.5.
47	0.0	Constraint equation weight for hypocenter fixed on plane. A large value, such as 1000, will prevent out-of-plane movement. If equal to 0, this option is not used. See also TEST(28) and (30). This option may not be used with the GLOBAL OPTION (see 2.2.3.11).
48	6.5	Half-space velocity used for first trial location (km/s).
49	0.0	If absolute value equals 1, compute Vp/Vs and origin time; if equals 2, also make printer plot of S-P vs P. If negative, use this origin time for earthquake location.
50	0.0	Compute this number of fixed depth solutions, starting with Z(1) = -TEST(8) and continuing with Z(i+1) = 1.2*Z(i) + 1.0. The maximum this value can be is 22., which produces a maximum depth of 225 km.
51	1000.0	Beyond this epicentral distance use first travel-time table model.
52	2800.0	Wood-Anderson magnification used in XMAG calculations.
53	1.0	If equal to 1, then assume stations with 4-letter codes ending with e or n are horizontal east-west and north-south stations, respectively.
54	200.0	If 1st computed trial epicenter is greater than this from closest station, start location at closest station.
55	19.0	Default century if not specified on the summary record.

Table II: (continued)

The default weights and its relative standard errors corresponding to each weight-code are reported in Table III. It is possible to change the default values using the WHEIGHT OPTION.

WEIGHT CODE	STANDARD ERROR (S)	STAND. ERROR RELATIVE TO READINGS WITH WEIGHT CODE ZERO	COMPUTED WEIGHT
0	0.1	1.0	1.0
1	0.5	5.0	1/25
2	1.0	10.0	1/100
3	2.0	20.0	1/400
4	INFINITE	INFINITE	0.0

Table III: Table with default HYPOELLIPSE weights.

The root-mean-square (RMS) is computed using this equation:

$$RMS = \left[\frac{\sum_1^n W_i R_i^2}{\sum_1^N W_i}\right]^{1/2}$$

For i phases, with $i=1,\ldots, N$; R_i is the observed minus computed time of the i^{th} phase and W_i is the computed weight of i^{th} phase.

This program computed for any earthquake location a quality factor based on the values of SEH (the horizontal 68% confidence limit in the least well-constrained direction) and SEZ (the 68% confidence limit for depth) see Table IV.

Quality	Larger of SEH and SEZ (km)
A	≤ 1.34
B	≤ 2.67
C	≤ 5.35
D	> 5.35

Table IV: Quality based on the value of the horizontal error SEH (68% confidence limit), and vertical error SEZ (68% confidence limit).

Appendix C

Program FPFIT, FPPLOT and FPPAGE

Program FPFIT (Reasenberg and Oppenheimer, 1985) finds only the double couple fault plane solution (source model) that best fits a given set of observed first motion polarities for an earthquake. FPFIT formally computes the uncertainty in the model parameters (strike, dip, rake) for each double couple source model obtained. The inversion is carried out through a two stage 3D grid search procedure that finds the source model. The first stage uses 20° increments in each of the three parameters strike, dip, and rake including all possible gridded values of rake and dip. However, only half the range of possible values of strike (from 0 to 160 degrees) is searched to avoid computing source models for both the fault plane and its associated auxiliary plane. For any earthquake, E^j, and any source model, M^i, the program computes the one-norm misfit function, $F^{i,j}$ defined:

$$F^{i,j} = \frac{\Sigma_k \left\{ \left| P_0^{j,k} - P_t^{i,k} \right| W_0^{j,k} W_t^{i,k} \right\}}{\Sigma_k \left\{ W_0^{j,k} W_t^{i,k} \right\}} \qquad (1)$$

Where k indicate the k-th station, $P_0^{j,k}$ and $P_t^{i,k}$ represent the observed and hypothetical first-motion polarity, respectively (0.5 for compression, -0.5 for dilatation). Finally, $W_0^{j,k}$ is the observation weight that must be assigned to the phases and $W_t^{i,k}$ is defined:

$$W_t^{i,k} = [A(i,k)]^{1/2} \qquad (2)$$

Is the square root of the normalized theoretical P-wave radiation amplitude, $A(i,k)$, associated at k-th station for source model. This weighting scheme down-weights observations near nodal planes, minimizing the effect of inconsistencies near nodal planes, such as those caused by unmodeled refractions.

The course search identifies the solution corresponding to the minimum misfit, F_{min}, and, if exist multiple solutions considers relative minima in misfit. These are detected in the range

search up to a level of misfit $F \leq F_{min}$ + DFITC (input parameter). Each of these solutions is then taken as the centre of a second stage (fine) search using grid point spacing of 5° for strike and dip, and 10° for rake and parameter ranges relative to the central value of ±45° in strike and dip and ±30° in rake. The final solutions are identified and the solution parameter uncertainties are estimated. The multiple solutions are distinguished by an asterisk in the output files.

These values are used in the display program FPPLOT to graphically define the range of P-axis and T-axis orientation consistent with the data.

For each fault-plane solution, FPFIT calculates these uncertainties:

1. F_j = minimum $[F_{i,j}]$ or a relative minimum of $F_{i,j}$. (F_j = 0.0 perfect fit to the data, while F_j = 1.0 perfect misfit).
2. NOBS = number of observations used in the solution.
3. The mean data weight used in the solution (AVWT); it is an rough measure of the quality of the data used in the solution. AVWT ranges from 0.0 to 30.0, larger values reflecting solutions computed from higher quality data.
4. The station distribution ratio ($0.0 \leq STDR \leq 1.0$). This quantity is sensitive to the distribution of the data on the focal sphere, relative to the radiation pattern. When this ratio has a low value ($STDR < 0.5$), then a relatively large number of the data lie near nodal planes in the solution. Such a solution is less robust than one for which $STDR > 0.5$.

FPFIT summarizes the quality of the adopted fault-plane solution with two letter codes. The first letter code, Q_f, summarizes the value of F_i. The second quality code, Q_p, summarizes the three parameter uncertainties ΔSTR, ΔDIP, and ΔRAK, see Table I:

Quality	**Q_f**	**Q_p**
A	$F_j \leq 0.025$	$\Delta s, \Delta d, \Delta r \leq 20°$
B	$0.025 < F_j \leq 0.1$	20° to 40°
C	$F_j > 0.1$	> 40°

Table I: Values of quality factor Q_f and Q_p for Fault-plane solution. F_j =0 indicate a perfect fit to the data, while F_j =1 is a perfect misfit. Δs, Δd and Δr are ranges of perturbation of strike, dip and rake, respectively.

Moreover, strike is measured clockwise from north; dip is measured down from horizontal; rake of 0 = left lateral, 90 = reverse, +180 = right lateral, -90 = normal.

Input File: FPFIT reads the print output file from programs: HYP071 (Lee and Lahr, 1975), HYPOINVERSE (Klein, 2002) and HYPOELLIPSE (Lahr, 1989). This file contains the hypocenter summary card, followed by (for each P-wave observation) the station to epicenter distance and azimuth, P-remark, angle of incidence, and flag denoting phase data discarded due to Jeffrey's weighting.

FPPLOT

FPPLOT is an interactive plotting program for displaying fault plane solutions calculated by FPFIT using as input file the "RAY" output file produced by FPFIT. FPPLOT produces one frame of graphic output for each solution found by FPFIT.

FPPAGE

FPPAGE is an interactive plotting program for displaying on a single page up to 42 fault plane solutions calculated by FPFIT using as input file the "RAY" output file produced by FPFIT. Each fault plane solution is represented by a lower hemisphere equal area projection. An asterisk (*) indicate multiple solutions. Compressional rays are depicted as solid circles; dilatational rays as open circles. Finally the P- and T-axes of the solution are plotted.

Appendix D

Program FMSI

FMSI (Gephart and Forsyth, 1984; Gephart, 1990) is a FORTRAN program for inverting fault and earthquake focal mechanism data to compute the regional stress tensor.

This program calculate only the three principal stress directions (σ_1, σ_2, σ_3) and one measure of stress magnitudes, $R = \frac{(\sigma_2 - \sigma_1)}{(\sigma_3 - \sigma_1)}$ $(0 \leq R \leq 1)$ that describes the relative magnitudes of the principal stresses and hence constrains the shape of the deviatoric part of the stress tensor. Values of R close to 0.0 indicate that σ_1 is similar to σ_2 (oblate stress ellipsoid) while values close to 1.0 indicate that σ_2 is similar to σ_3 (prolate stress ellipsoid) (Mandal, 2008). The method requires the basic assumption that the stress is uniform in space and time in the investigated volume. It inverts the populations of fault data to determine the best-fitting values of four stress parameters minimizing the rotation differences between given observations and any ones which are consistent with the model. Moreover, FMSI compare the geometry indicated by each nodal plane independently to any stress model, acknowledging that only one actually can be the fault (the true fault plane is the one with the smaller deviation from any fault geometry consistent with the model).

The FMSI input file contain focal mechanisms or fault datum indicating the azimuth and slip of the two nodal planes (degrees) and a sense of slip/weight index.

In this program, the user may select from among three measures of rotation misfit:

1. The Exact method that determines the minimum rotation between an observation and model (most realistic but also most time-consuming).
2. The Pole Rotation method, which computed the minimum rotation about the pole to the fault plane needed to match an observed slip (faster).

3. The Approximate method, which identifies the smallest of the three rotations offers a significant improvement in quality of solutions compared to the Pole Rotation method with similar computational demands.

Later, it is devised a scheme for inspecting a range of possible stresses. At the start, it is selected $\sigma_1$or σ_3 as the *primary* principal stress, and the other as the *secondary* principal stress. A preliminary estimate of principal stress orientations is made from inspection of fault geometries, perhaps based on the distribution of the P and T axes. User inserts input parameters (plunge, azimuth, variance) for the primary principal stress in the program prompt for constructing the grid. The grid search is implemented by selecting sequentially a number of specific primary stress directions.

Appendix E

Program HYPODD

HYPODD is a Fortran computer code package for relocating earthquakes using the double-difference technique (DD) of Waldhauser and Ellsworth (2000). This package is constituted by two programs to compute DD hypocenter locations: PH2DT and HYPODD.

PH2DT searches catalogue P- and S-phase data for event pairs with travel time information at common stations and subsamples these data in order to optimize the quality of the phase pairs and the connectivity between events. It establishes such a network by building links from each event to a maximum number of neighbours per event (MAXNGH) within a search radius defined by maximum hypocentral separation between event pairs (MAXSEP). To reach the maximum number of neighbours with less than minimum number of links to define a neighbour (MINLNK) phase pairs are considered. Generally a strong link are defined by eight or more observations (one for each degree of freedom).

If we consider a large number of events (~10,000) we might consider only strongly connected earthquakes pairs setting minimum number of links per pair saved (MINOBS) equal to MINLNK. For a small number of events we might select all phase pairs available by setting: MINOBS=1, maximum number of links per pair saved (MAXOBS) equal to the number of stations, and MAXNGH equal to the number of events. Another parameter it is MINWGHT that is defined as minimum pick weight [0 - 1(best)]. Exactly, picks with a pick weight smaller than MINWGHT but larger than 0 are ignored and links of event pairs that have less than MINOBS observations are discarded.

PH2DT removes outliers identified as delay times that are larger than the maximum expected delay time for a given event pair. The maximum expected delay time is the time for P-/S-waves to travel between two events calculated considering initial event locations and a P- and

S-velocity of 4 and 2.3 km/s, to it is added 0.5 s to the cuttoff to account for uncertainty in the initial locations. The output value of the average distance between strongly linked events indicates the density of the hypocenter distribution and indicate the value of maximum event separation distance for input catalogue data (WDCT) parameter used in HYPODD.

The value for minimum number of catalogue links per event pair to form a continuous cluster (OBSCT) in HYPODD should be equal to or less than the value for MINLNK in PH2DT. Moreover, it is possible to choice two methods to solve the system of DD equations:

- The singular value decomposition (SVD) described in the Chapter 2 section 2.2.1. It is used for examining the behaviour of small systems (~100 events).
- The conjugate gradients method (LSQR) (Chapter 2 section 2.2.3) for systems of a large number of events. It takes the advantage of the sparseness of the system of DD-equations. Errors reported are grossly under estimated (Waldhauser, 2001).

In Table I and II are described the parameters for the input file of PH2DT and HYPODD respectively.

MINWGHT	Minimum pick weight [0-1(best)]
MAXDIST	Maximum distance (km) between event pair and station
MAXSEP	Max. hypocenter separation between event pairs (km)
MAXNGH	Max. number of neighbours per event
MINLNK	Min. number of links required to define a neighbour
MINOBS	Min. number of links per pair saved
MAXOBS	Max. number of links per pairs saved

Table V: Parameter description for the PH2DT input file.

Input files:

- Input control file for PH2Dt (ph2dt.inp)
- File with station coordinates
- File with event locations and phase data.
- Input file for HYPODD (*.inp)
- Output of PH2DT program event locations (*.sel)
- Output of phase difference times of PH2DT program (*.dt)
- Cross correlation difference times if is used (*.cc).

IDAT	1=cross-correlation data only; 2= absolute (catalogue) data only; 3=cross-corr and catalogue data
IPHA	1=P-wave; 2=S-wave; 3=P- and S- wave
DIST	Max. distance between centroid of the event cluster and stations
OBSCC, OBSCT	Min. number of cross-corr, catalogue links per event pair to form a continuous cluster
ISTART	Initial location: 1= start from cluster centroid, 2= start from catalogue locations
ISOLV	1=SVD; 2= LSQR
NSET	Number of iteration sets
NITER	Number of iteration for the set
WTCCP, WTCCS	Weight for cross-corr P- and S-wave data. -9=data not used
WTCTP, WRCT	Weight for catalogue P- and S-wave data. -9=data not use
WRCC, WRCT	Cutoff threshold for outliers located on the tails of the cross-corr, catalogue data. -9= no outlier removed
WDCC, WDCT	Max. event separation distance (km) for cross-corr and catalogue data respectively. -9= data not activated
DAMP	Damping (only for ISOLV=2)
NLAY	Number of model layers (max 12)
RATIO	Vp/Vs ratio (constant for all layers)
TOP	Depths of top of layer (km)
VEL	Layers velocity (km/s)
CID	Index of cluster to be relocated (0=all)
ID	ID of events to be relocated. Blank for all events

Table VI: Parameter description of input file of HYPODD.

Appendix F

Program GLOBALLOCALIZER

This program was developed by Pignatelli et al, 2008 for searching of small aftershocks subsequent to an underground explosion. The algorithm is a computer code on a MATLAB platform, and has a very simple Graphical User Interface (GUI). This interactive GUI allows results to be rapidly processed and immediately visualized.

Steps of the program:

1. Computing waveform cross-correlation only for P-waves
2. Earthquake relocation using a Joint Hypocentral Determination (JHD) method to the time differences between the seismograms of two events described by Console and Giuntini, (2006). This is developed only for teleseismic earthquakes with a spherical velocity model.

The cross-correlation procedure consist of select an event and a station waveform of reference. If it is necessary, it is possible to carry out an interactive filter using a windows put on down-left side of the reference window. Setting: the window size, the "advance time" (Advance is the instant at which calculation of cross-correlation begins) and the "number of steps" (Step is interpolated sampling interval), the program computed waveform cross-correlation between waveform of the reference station and the others waveforms of the same station for the others events using the equation (Taylor, 1982):

$$R = \frac{N\sum_{i=1}^{N} X_i Y_i - \sum_{i=1}^{N} X_i \sum_{i=1}^{N} Y_i}{\sqrt{\left[N\sum_{i=1}^{N} X_i^2 - \left(\sum_{i=1}^{N} X_i\right)^2\right]\left[N\sum_{i=1}^{N} Y_i^2 - \left(\sum_{i=1}^{N} Y_i\right)^2\right]}}$$

where X_i and Y_i are the samples of the digital waveform segments and N is the number of samples of the correlation window. If R assumes the maximum value of 1 then the two

seismograms are identical, while if they are different then they are associated with lower cross-correlation values. The program allows to interactively move the absolute maximum value of R function to a relative maximum one by button “Interactive Maxima”. The analysis can be saved in a file that can be used successively.

Input files:

- Waveform folder (with the waveform files *.ascii)
- Arrival time folder (with the locations and arrival times files of earthquakes *.ascii)
- File events (containing a list of events *.dat)
- File with station coordinates (*.dat).

References

Alessio, G., Esposito, E., Gorini, A., Porfido, S., 1995. Detailed study of the Potentino seismic zone in the Southern Apennines, Italy. Tectonophysics 250, 113–134.

Amato, A., Selvaggi, G., 1993. Aftershock location and P-velocity structure in the epicentral region of the 1980 Irpinia earthquake, Annali di Geofisica, 36, 3-15.

Amicucci, L., Barchi, M.R., Montone, P., Rubiliani, N., 2008. The Vallo di Diano and Auletta extensional basins in the southern Apennines (Italy): a simple model for a complex setting. Terra Nova 20, 475–482, doi:10.1111/j.13653121.2008.00841.x.

Anderson, H., Jackson, J., 1987. Active tectonics of the Adriatic region. Geophys. J. Roy. Astron. Soc. 91, 937–983.

Argus, D. F., Gordon, R.G., DeMets, C., and Stein, S., 1989. Closure of the Africa-Eurasia-North America Plate Motion Circuit and Tectonics of the Gloria Fault. J. Geophys. Res. 94, B5, 5585-5602.

Argnani, A., Frugoni, F., Cosi, R., Ligi, M., Favali, P., 2001. Tectonics and seismicity of the Apulian Ridge south of Salento peninsula (Southern Italy). Ann. Geofis. 44 (3), 527–540.

Argnani, A., Rovere, M., Bonazzi, C., 2009. Tectonics of the Mattinata fault, offshore south Gargano (southern Adriatic Sea, Italy): implications for active deformation and seismotectonics in the foreland of the southern Apennines. Geol. Soc. Am. Bull. 121, 1421–1440, doi:10.1130/B26326.1.

Azzara, R., Basili, A., Beranzoli, L., Chiarabba, C., Di Giovambattista, R., Selvaggi, G., 1993. The seismic sequence of Potenza (May 1990). Ann. Geofis., 36 (1), 237-243.

Barba, S., Carafa, M.M.C., Mariucci, M.T., Montone, P., Pierdominici, S., 2009. Present-day stress-field modelling of southern Italy constrained by stress and GPS data, Tectonophysics, doi:10.1016/j.tecto.2009.10.017

Barberi, G., Casentino, M.T., Gervasi, A., Guerra, I., Neri, G., Orecchio, B., 2004. Crustal seismic tomography in the Calabrian Arc region, South. Italy. Phys. Earth Planet. Inter. 147, 297-314.

Basili, R., Valensise, G., Vannoli, P., Burrato, P., Fracassi, U., Mariano, S., Tiberti, M.M., Boschi, E., 2008. The Database of Individual Seismogenic Sources (DISS), version 3: summarizing 20 years of research on Italy's earthquake geology. Tectonophysics 453, 20–43.

Bassin, C., Laske, G. and Masters, G., 2000. The Current Limits of Resolution for Surface Wave Tomographyin North America, EOS Trans AGU, 81, F897.

Benedetti, L., Tapponnier, P., King, G.C.P., Piccardi, L., 1998. Surface rupture of the 1857 southern Italian earthquake? Terra Nova 10, 206–210.

Boncio, P., Mancini, T., Lavecchia, G., Selvaggi, G., 2007. Seismotectonics of strike-slip earthquakes within the deep crust of southern Italy: Geometry, kinematics, stress field and crustal rheology of the Potenza 1990-1991 seismic sequences (Mmax 5.7). Tectonophysics, 445, 281-300.

Bonini, M., Sani, F., Moratti, G., Benvenuti, M.G., 2011. Quaternary evolution of the Lucania Apennine thrust frint area (Southern Italy) and its relations with the kinematics of the Adria Plqte boundaries. Journal of Geod., 51, 125-140.

Boschi, E., Guidoboni, E., Ferrari, G., Mariotti, D., Valensise, G., Gasperini, P., 2000. Catalogue of Strong Italian Earthquakes from 461 B.C. to 1980. Ann. Geof., 43, 609-868.

Branno, A., Esposito, E., Marturano, A., Porfido, S., Rinaldis, V., 1983. Studio su base macrosismica del terremoto della Basilicata del 16 Dicembre 1857. Boll. Soc. Nat. Napoli 92, 249–338.

Branno, A., Esposito, E., Marturano, A., Porfido, S., Rinaldis, V., 1985. The Basilicata earthquake of December16, 1857. Atlas of IsoseismalMapsof Italian Earthquake, CNR-PFG, N. 114 (vol. 2A), 88–91.

Brozzetti, F., Lavecchia, G., Mancini, G., Milana, G., Cardinali, M., 2009. Analysis of the 9 september 1998 MW 5.6 Mercure earthquake sequence (Southern apennines, Italy): a multidisciplinary approach. Tectonophysics, 476, 210-225.

Burrato, P. and G. Valensise, 2007. Il terremoto del 16 dicembre 1857 (Mw 7.0): caratterizzazione di una sorgente sismogenetica complessa. In: Ferrari, G.. 16 dicembre 1857 un grande disastro sismico. Da un terremoto laboratorio a laboratori sul territorio, 121-138, Bologna, SGA, ISBN/ISSN: 78-88-85213-13-5.

Burrato, P. and G. Valensise, 2008. Rise and Fallo f a Hypothesized Seismic Gap: Source Complexity in the Mw 7.0 16 December 1857 Southern Italy Earthquake., Bull. Of the Seism. Soc. of America, 98(1), 139-148, doi: 10.1785/0120070094

Calcagnile, G., Panza, G.F., 1980. The main characteristics of the lithosphere-asthenosphere system in Italy and surrounding regions. Pure Appl. Geophys. 119, 865-879.

Cassinis, R., Scarascia, S., Lozej, A., 2003. The deep crustal structure of Italy and surrounding areas from seismic refraction data. A new synthesis. Boll. Soc. Geol. It.,122, 365-376.

Castelli, V., Galli, P., Camassi, R., Caracciolo, C., 2008. The 1561 earthquake(s) in Southern Italy: new insight into a complex seismic sequence. J. Earthquake Eng. 12 (7), 1054–1077, doi:10.1080/13632460801890356.

Castello, B., Selvaggi, G., Chiarabba, C., Amato, A., 2005. CSI Catalogo della sismicità italiana 1981-2002. Versione 1.0 (INGV-CNT, Roma), (on line: http://www.ingv.it/CSI/).

Castello, B., Selvaggi, G., Chiarabba, C., Amato, A., 2006. CSI Catalogo della sismicità italiana 1981–2002. versione 1.1. INGV-CNT, http://www.ingv.it/CSI/.

Castello, B., Moschillo, R., Pignone, M., Vinci, S., Doumaz, F., Nostro, C., Selvaggi, G., 2008. Seismicity map of Italy, 2000–2007. INGV-CNT, Roma.

Cello, G., Tondi, E., Micarelli, L., Mattioni, L., 2003. Active tectonics and earthquake sources in the epicentral area of the 1857 Basilicata earthquake (southern Italy). J. Geodyn. 36, 37–50.

Channell, J.E.T., D'Argenio, B., Horvath, F., 1979. Adria, the African promontory, in Mesozoic Mediterranean paleogeography. Earth-Science Reviews 15, 213–292.

Chatelain, J.L., 1978. Etude fine de la sismicité en zone de collision continentale à l'aide d'un réseau de statios portables: la region Hindu-Kush-Pamir . Thèse de 3 éme cycle, Univ. Paul Sabatier, Toulouse.

Chiarabba, C., and Amato, A., 1996. Crustal velocity structure of the Apennines (Italy) from P-wave travel time tomography. Ann Geofis., XXXIX (6), 1133-1148.

Chiarabba, C. and Frepoli, A., 1997. Minimum 1D velocity models in Central and Southern Italy: a contribution to better constrain hypocentral determinations. Ann. Geofis., XL (4), 937-954.

Chiarabba, C., Jovane, L., Di Stefano, R., 2005. A new view of Italian seismicity using 20 years of instrumental recordings. Tectonophysics, 395, 251-268.

Cimini, G.B., De Gori, P., Frepoli, A., 2006. Passive seismology in Southern Italy: the SAPTEX array. Ann. Geofis., 49 (2/3), 825-840.

Cinque, A., Patacca, E., Scandone, P., Tozzi, M., 1993. Quaternary kinematic evolution of the Southern Apennines: relationships between surface geological features and deep lithospheric structures. Ann. Geofis. 36, 249–259.

Cinti, F.R., Cucci, L., Pantosti, D., D'Addezio, G., Meghraoui, M., 1997. A major seismogenic fault in a 'silent area': the Castrovillari fault (southern Apennines, Italy). Geophys. J. Int. 130, 595–605.

Console, R., Di Giovambattista, R., Favali, P., Smriglio, G., 1989. Lower Adriatic sea seismic sequence (January 1986): spatial definition of the seismogenic structure. Tectonophysics, 166, 235 - 246.

Console, R. and Giuntini, A., 2006. "An algorithm for double difference joint hypocenter determination: application to the 2002 Molise (Central Italy) earthquake sequence", Annals of Geophysics, Vol. 49, No. 2/3.

Corrado, S., Invernizzi, C., Mazzoli, S., 2002. Tectonic burial and exhumation in a foreland fold and thrust belt: the Monte Alpi case history (Southern Apennines, Italy). Geodin. Acta 15, 159–177.

CPTI Working Group, 2004. Catalogo Parametrico dei Terremoti Italiani. Versione 2004 (CPTI04). INGV, Bologna, http://emidius.mi.ingv.it/CPTI04/.

Cucci, L., D'Azzedio, G., Valensise, G., Burrato, P., 1996. Investigating seismogenic faults in Central and Southern Apennines (Italy): modeling of fault-related landscape features. Annals of Geophysics, XXXIX, 3.

Cucci, L., Pondrelli, S., Frepoli, A., Mariucci M.T., and Moro M., 2004. Local pattern of stress field and seismogenic sources in the Pergola-Melandro Basin and the Agri Valley (Southern Italy). Geophys. J. Int., 156 (3), 575-583.

D'Agostino, N., Selvaggi, G., 2004. Crustal motion along the Eurasia–Nubia plate boundary in the Calabrian Arc and Sicily and active extension in the Messina Straits from GPS measurements. J. Geophys. Res. 109, B11402, doi:10.1029/2004JB002998.

D'Agostino, N., Avallone, A., Cheloni, D., D'Anastasio, E., Mantenuto, S., Selvaggi, G., 2008. Active tectonic of the Adriatic region from GPS and earthquake slip vectors. J. Geophys. Res. 113, B12413, doi:10.1029/2008JB005860.

D'Anna, G., Mangano, G., D'Alessandro, A., D'Anna, R., Passafiume, G., Speciale, S, Amato, A., 2009. Il nuovo OBS/H dell'INGV. Quaderni di Geofisica, 65, ISSN 1590-2595.

Del Gaudio, V., Pierri, P., Calcagnile, G., Venisti, N., 2005. Characteristics of the low Energy seismicity of central Apulia (southern Italy) and hazard implications. Jour. of seismology, 9, 39-59.

Del Gaudio, V., Pierri, P., Frepoli, A., Calcagnite, G., Venisti, N., Cimini, G.B., 2007. A critical revision of the seismicity of Northern Apulia (Adriatic microplate-Southern Italy) and implications for the identification of seismogenic structures. Tectonophysics, 436, 9-35.

De Mets, C., Gordon, R.G., Argus, D.F., Stein, S., 1990. Current plate motions. Geophys. J. Int. 104, 73-74.

Di Luccio, F., Fukuyama, E., Pino, N.A., 2005. The 2002 Molise earthquake sequenze: What can I learn about the tectonics of Southern Italy? Tectonophysics, 405, 141-154.

D'Ingeo, F., Calcagnile, G., Panza, G.F., 1980. On the fault plane solutions in the Central-Eastern Mediterranean region. Boll. Geofis. Teor. Appl. 22, 13–22.

Di Bucci, D., Corrado, S., Naso, G., 2002. Active faults at the boundary between Central and Southern Apennines (Isernia, Italy). Tectonophysics 359, 47– 63.

DISS Working Group, 2006. Database of Individual Seismogenic Sources (DISS), Version 3.0.2: A compilation of potential sources for earthquakes larger than M 5.5 in Italy and surrounding areas. http://www.ingv.it/DISS/.

DISS Working Group, 2009. Database of Individual Seismogenic Sources (DISS), Version 3.1.0: A Compilation of Potential Sources for Earthquakes Larger than M 5.5 in Italy and Surrounding Areas. ©INGV 2009-Istituto Nazionale di Geofisica e Vulcanologia. All rights reserved, http://diss.rm.ingv.it/diss/

Doglioni, C., Mongelli, F., Pieri, P., 1994. The Puglia uplift (SE Italy): an anomaly in the foreland of the Apenninic subduction due to buckling of a thick continental lithosphere. Tectonics 13, 1309–1321, doi:10.1029/94TC01501.

Doglioni, C., 1996. Geological remarks on the relationships between extension and convergent geodynamic settings. Tectonophysics 252, 253– 268.

Douglas, A., 1967. Joint epicentre determination. Nature, vol. 215, 47-48.

Ekstrom, G., 1994. Teleseismic analysis of the 1990 and 1991 earthquakes near Potenza. Ann. Geofis., XXXVII, 1591–1599.

Favali, P., Mele, G., Mattietti, G., 1990. Contribution to the study of Apulian microplate geodynamics. Mem. Soc. Geol. It. 44, 71–80.

Favali, P., Funiciello, R., Mattietti, G., Mele, G., Salvini, F., 1993. An active margin across the Adriatic Sea (central Mediterranean Sea), Tectonophysics, 219, 109-117.

Ferranti, L., Oldow, J.S., Sacchi, M., 1996. Pre-Quaternary orogenparallel extension in the Southern Apennine belt, Italy. Tectonophysics 260, 325–347.

Fracassi, U., and Valensise, G., 2007. Unveiling the sources of the catastrophic 1456 multiple earthquake: Hints to an unexplored tectonic mechanism in southern Italy, in stampa, Bull. Seismol. Soc. Am., 93, 3.

Frepoli, A., Selvaggi, G., Chiarabba, C., Amato, A., 1996. State of stress in the Southern Tyrrhenian subduction zone from fault-plane solutions, Geophys. J. Int., 125, 879-891.

Frepoli, A., and Amato A., 2000. Fault plane solutions of crustal earthquakes in Southern Italy (1988-1995): seismotectonic implications. Ann. Geofis., 43 (3), 437-467.

Frepoli, A., Cinti, F.R., Amicucci, L., Cimini, G.B., De Gori, P., Pierdominici, S., 2005. Pattern of seismicity in the Lucanian Apennines and foredeep (Southern Italy) from recording by SAPTEX temporary array. Ann. Geofis., 48 (6), 1035-1054.

Frepoli, A., F. Marra, C. Maggi, A. Marchetti, A. Nardi, N. M. Pagliuca, and M. Pirro, 2010. Seismicity, seismogenic structures, and crustal stress fields in the greater Rome area (central Italy), J. Geophys. Res., 115, B12303, doi:10.1029/2009JB006322.

Frepoli, A., Maggi, C., Cimini, G.B., Marchetti, A., Chiappini, M., 2011. Seisomotectonic of Southern Apennines from recent passive seismic experiments. Journal of Geodynamics, doi:10.1016/j.jog.2010.02.007, (In press).

Fréchet, J., 1985. Sismogenèse et doublets sismiques. Thèse d'État, Université Scientifique et Médicale de Grenoble, 206 pp.

Galadini, F., Meletti, C., Vittori, E., 2000. Stato delle conoscenze sulle faglie attive in Italia: elementi geologici di superficie. In: Galadini, et al. (Eds.), Le ricerche del GNDT nel campo della pericolosità sismica (1996–1999). CNR-Gruppo Nazionale per la Difesa dai Terremoti, Roma, pp. 107–136, Also available from http://www.ingv.it/gndt/Pubblicazioni/Meletti copertina.htm.

Galli, P. and Naso, G., 2008. The "taranta" effect of the 1743 earthquake in Salento (Apulia, southern Italy). Boll. Geof. Teor. Appl..

Gasperini, P., F. Bernardini, G. Valensise, and E. Boschi (1999). Defining seismogenic sources from historical earthquake felt reports, Bull. Seismol. Soc. Am. 89, 94–110.

Gentile, G. F., Bressan, G., Burlini, L., and De Franco R., 2000. Three-dimensional Vp and Vp/Vs models of the upper crust in the Friuli area (northeastern Italy). Geophys. J. Int., 141,457-478.

Gephart, J.W. and Forsyth, D.W., 1984. An improved method for determining the regional stress tensor using earthquake focal mechanism data: application to the San Fernando earthquake sequence, J. Geophys. Res., 89 (B11), 9305-9320.

Gephart, J.W., 1990. FMSI: a Fortran program for inverting fault/slickenside and earthquake focal mechanism data to obtain the regional stress tensor, Comput. Geosci., 16, 953-989.

Got, J. L., Fréchet, J.,. Klein, F.W, 1994. Deep fault plane geometry inferred from multiplet relative location beneath the south flank of Kilauea. J. Geophys. Res. 99, pp. 15375–15386.

Gueguen, E., Doglioni, C., Fernandez, M., 1998. On the post-25Ma geodynamic evolution of the western Mediterranean. Tectonophysics 298, 259–269.

Guerra, I., Harabaglia, I., Gervasi, A., Rosa, A.B., 2005. The 1998-1999 Pollino (Southern Apennines, Italy) seismic crisis: tomography of a sequence. Ann. Geofis., 48, 6.

Gupta, H.K., Rastogi, B.K. and Narain, H., 1972. Common features of the reservoir associated seismic activities, Bull. seism. Soc. Am., 62, 481–492.

Harabaglia, P., Monelli F., and Zito, G., 1997. Geothermics of the Apennines subduction. Ann. Geofis., XL (5), 1261-1274.

Hippolyte, J.C., Angelier, J., Roure, F., 1994. A major geodynamic change revealed by Quaternary stress patterns in the Southern Apennines (Italy). Tectonophysics 230, 199–210.

Hippolyte, J.C., Angelier, J., Barrier, E., 1995. Compressional and extensional tectonics in an arc system: example of the Southern Apennines. J. Struct. Geol. 17, 1725–1740.

Kissling, E., 1988. Geotomography with local earthquake data, Rev. Geophys. 26, 659-698.

Kissling E., Ellworth, W.L., Eberhart-Phillips, D., Kradolfer, U., 1994. Initial reference models in local earthquake tomography. J. Geophys. Res., 99, 19635-19646.

Kissling, E., Ellsworth, W.L., Eberhart-Phillips, D., Kradolfer, U., 1995. Initial reference models in local earthquake tomography. J. Geophys. Res., 99, 19635-19646.

Klein, F.W., 2002. User's guide to Hypoinverse, a Fortran program to solve for earthquake locations and magnitudes, Open-File Report 02-171, me Geological Survey, Menlo Park, California.

Lahr, J.C., 1989. HYPOELLIPSE/Version 2.0: a computer program for determining local earthquake hypocentral parameters, magnitude, and first motion pattern. U. S. Geol. Surv. Open File Rep., 95, 89-116.

Lay, T., and Wallace, T.C., 1995. Modern Global Seismology. Academic press.

Lee, W. H. K. and J. C. Lahr, 1975. HYP071 (Revised): A computer program for determining hypocenter, magnitude, and first motion pattern of local earthquakes, U. S. Geological Survey Open File Report 75-311, 113 pp.

Locardi, E., and Nicolich, R., 1988. Geodinamica del Tirreno e dell'appennino centromeridionale, la nuova carta della Moho. Mem. Soc. Geol. It., 41, 121-140.

Lucente, F.P., Piana Agostinetti, M. Moro, G. Selvaggi, and M. Di Bona, 2005. Possible fault plane in a seismic gap area of the southern Apennines (Italy) revealed by receiver function analysis, J. Geophys. Res., 110, B04307, doi:10.1029/2004JB003187.

Maggi, C., Frepoli, A., Cimini, G. B., Console, R., Chiappini, M., 2009. Recent seismicity and crustal stress field in the Lucanian Apennines and surroundings areas (Southern Italy): seismotectonic implications, Tectonophysics, 463, 130-144, doi:10.1016/j.tecto.2008.09.032.

Magri, G., Molin, D., 1979. Attività macrosismica in Basilicata, Campania e Puglia dal 1847 al 1861. Technical Report, C.N.E.N., RT/AMB (79) 5.

Malinverno, A., and Ryan, W.B.F, 1986. Extension in the Tyrrhenina Sea and shortening in the Apennines as result of arc migration driven by sinking of the lithosphere. Tectonics, 5, 227-245.

Mandal, P., 2008. Stress Rotation in the Kachchh Rift Zone, Gujarat, India. Pure appl. Geophys., 165, 1307-1324. Doi: 10.1007/s00024-008-0362-4

Margottini, C., 1981. Il terremoto del 1743 nella Penisola Salentina. Mem. Conv. Annu. PFG-CNR, 251–279.

Maschio, Ferranti, L., and Burrato, P., 2005. Active extension in Val d'Agri area, southern Apennines, Italy: implications for the geometry of the seismogenic belt. Geophys. J. Int., 162, 591-609.

Mastronuzzi, G., Pignatelli, C., Sansò, P., Selleri, G., 2007. Boulder accumulations produced by the 20th of February, 1743 tsunami along the coast of southeastern Salento (Apulia region, Italy). Mar. Geol. 242, 191–205.

Meletti, C., Patacca, E., Scandone, P., 2000. Construction of a seismotectonic model: the case of Italy. Pure Appl. Geophys. 157, 11–35.

Menardi Noguera, A., Rea, G., 2000. Deep structure of the Campanian–Lucanian Arc (Southern Apennine, Italy). Tectonophysics 324, 239–265.

Merlini, S. and Mostardini, 1986. Appennino centro meridionale: sezioni geologiche e proposta di modello strutturale. Mem. Soc. Geol. It., 35, 177-202, Roma.

Merlini, S. and Cippitelli, G., 2001.Structural styles inferred by seismic profiles, in Anatomy of an Orogen: the Apennines and adjacent Mediterranean Basins. G.B. Vai and I.P. Martini (eds.), Kluwer Academic Publishers, 441-454.

Michetti, A.M., Ferreli, L., Serva, L., Vittori, E., 1997. Geological evidence for strong historical earthquakes in an 'aseismic' region: the Pollino case (southern Italy). J. Geodyn. 24, 67–86.

Milano, G., Di Giovanbattista, R., Ventura, G., 2005. The 2001 seismic activity near Isernia (Italy): Implications for the seismotectonics of the Central–Southern Apennines. Tectonophysics, 401, 167– 178.

Molin, D. And Margottini, C., 1985. The earthquake of July 1627 in the Northern Capitanata. Atlas of Isoseismal Maps of Italian Earthquakes, vol. 2A. CNR-PFG.

Montone, P., Amato, A., Pondrelli, S., 1999. Active stress map of Italy. J. Geophys. Res. 104, 25595–25610.

Montone, P., Mariucci, M.T., Pondrelli S., and Amato, A., 2004. An improved stress map for Italy and surrounding regions (Central Mediterranean). J. Geophys. Res., 109.

Morelli, C., 1997. Recent deeper geophysical results better account for the tectonics in the Italian area. Ann. Geofis., XL (5), 1345-1358.

Morelli, C., 2000. The themes of crustal research in Italy and the role of DSS-WA seismics, Boll. Soc. Geol. It., 119, 141-148.

Nostro, C., Cocco, M., Belardinelli, M.E., 1997. Static stress changes in extensional regimes: an application to Southern Apennines (Italy). Bull. Seismol. Soc. Am. 87 (1), 234–248.

Ogniben, L., 1975. Lithostratigraphic complexes and evidence for tectonic phases in Sicily and Calabria. In: L. Ogniben, M. Parotto and A. Praturlon, Editors, Structural Model of Italy, C.N.R. Quad. Ric. Sci., 90, 365–408.

Oldow, J.S., D'Argenio, B., Ferranti, L., Pappone, G., Marsella, E., Sacchi, M., 1993. Large-scale longitudinal extension in the southern Apennines contractional belt, Italy. Geology 21, 1123–1126.

Paige, C.C. and Saunders, M.A., 1982. LSQR: sparse linear equations and least squares problems. ACM Trans. Mathematical Software 8 2, pp. 195–209.

Pantosti, D., Valensise, G., 1990. Faulting mechanism and complexity of the November 23, 1980, Campania–Lucania earthquake, inferred from surface observations. J. Geophys. Res. 95, 15319–15341.

Pantosti, D., Schwartz, D.P., Valensise, G., 1993. Paleoseismology along the 1980 Irpinia earthquake fault and implications for earthquake recurrence in the southern Apennines. J. Geophys. Res. 98, 6561–6577.

Papanikolaou, I.D., Roberts, G.P., 2007. Geometry, kinematics and deformation rates along the active normal fault system in the southern Apennines: implications for fault growth. J. Struct. Geol. 29, 166–188.

Patacca, E., Sartori, R., Scandone, P., 1990. Tyrrhenian basin and Apenninic arcs: kinematic relations since late Tortonian times. Mem. Soc. Geol. It. 45, 425–451.

Piccardi, L., 2005. Paleoseismic evidence of legendary earthquakes: the apparition of Archangel Michael at Monte Sant'Angelo (Italy). Tectonophysics 408, 113–128, doi:10.1016/j.tecto.2005.05.041.

Pieri, P., Festa, V., Moretti, M., Tropeano, M., 1997. Quaternary tectonic activity of the Murge area (Apulian foreland–southern Italy). Ann. Geophys. 40 (5), 1395–1404.

Pignatelli, A., Giuntini, A., Console, R., 2008 Matlab software for the analysis of seismic waves recorded by tree-elements arrays. Computers and Geosciences 34, 792–801.

Pontoise, B., Monfret, T., 2004. Shallow seismogenic zone detected from an offshore-onshore temporary seismic network in the Esmeraldas area (Northern Ecuador). Geochem. Geophys. Geosyst., 5 (2), 1-22.

Pondrelli, S., Morelli, A., Ekström, G., Mazza, S., Boschi E., and Dziewonski, A.M., 2002. European-Mediterranean regional centroid-moment tensor:1997-2000. Phys. Earth Planet. Int., 130, 71-101.

Reasenberg, P., and Oppenheimer, D., 1985. FPFIT, FPPLOT and FPPAGE: FORTRAN computer programs for calculating and displaying earthquake fault-plane solutions. U.S. Geol. Surv. Open-File Rep. 85-739.

Reddy, C.D., Prajapati, S.K., 2009. GPS measurements of postseismic deformation due to October 8, 2005 Kashmir earthquake. J. Seismol. 13, 415–420, doi:10.1007/s10950-008-9111-5.

Renner, G., Slejko, D., 1994. Some comments on the seismicity of the Adriatic region. Boll Geof. Teor. App., XXXVI, n. 141-144, pp. 381-398.

Royden, L., Patacca, E., Scandone, P., 1987. Segmentation and configuration of subducted lithosphere in Italy. An important control on thrust-belt and foredeep-basin evolution. Geology 15, 714–717.

Rosenbaum, G., Lister, G.S., 2004. Neogene and Quaternary rollback evolution of the Tyrrhenian Sea, the Apennines and the Sicilian Maghrebids. Tectonics 23, 1518–1535.

Scrocca, D., Carminati, E., Doglioni, C., 2005. Deep structure of southern Apennines, Italy: Thin-skinned or thick-skinned? Tectonics, 24, 1-20.

Scrocca, D., 2006. Thrust front segmentation induced by differential slab retreat in the Apennines (Italy). Terra Nova 18, 154–161

Sbar, M. L., M. Barazangi, J. Dorman, C. H. Scholz, and R. B. Smith, 1972. Tectonics of the Intermountain Seismic Belt, Western United States: Microearthquake seismicity and composite fault plane solutions. Bull. Geol. Soc. Am. 83, 13-28.

Serva, L., 1985. The earthquake of September 8, 1694 in Campania–Lucania. Atlas of Isoseismal Maps of Italian Earthquakes, vol. 2A. CNR-PFG.

Speranza, F., and Chiappini, M., 2002. Thick-skinned tectonics in the external Apennines, Italy: New evidence from magnetic anomaly analysis. J. Geophys. Res., 107 (B11), 2290.

Stein, S., and Wysession, M., 2003. Introduction to Seismology, Earthquakes and Earth Structure. Oxford, Blackwell, 498.

Stoffer, 2006. Geologic history of Southern California. USGS.

Taylor, J.R., 1982. An Introduction to Error Analysis, the Study of Uncertainties in Physical Measurements. University Science Books, Sausalito, CA, 327 pp.

Talwani, P., 1997. On the nature of reservoir-induced seismicity. Pure Appl. Geophys. 150, 473–492.

Tesauro, M., Kaban, M.K., Cloetingh, S.A.P.L., 2008. EuCRUST-07: A new reference model for the European crust. Geophys. Res. Lett., 35 (5).

Tiberti, M.M., Orlando, L., Bucci, D., Bernarbini, M., Parotto, M., 2005. Regional gravity anomaly map and crustal model of the Central-Southern Apennines (Italy). Journal of Geodynamics, 40, 73-91.

Tondi, E., Piccardi, L., Cacon, S., Kontny, B., Cello, G., 2005. Structural and time constraints for dextral shear along the seismogenic Mattinata Fault (Gargano, southern Italy). J. Geodyn. 40, 134–152, doi:10.1016/j.jog.2005.07.003.

Valensise, G., Pantosti, D., Basili, R., 2004. Seismology and tectonic setting of the 2002 Molise (Italy) earthquake. Earthquake Spectra 20, 23–37, doi:10.1193/1.1756136.

Valoroso, L., Improta, L., Chiaraluce, L., Di Stefano, R., Ferranti, L., Govoni, A., Chiarabba, C., 2009. Active faults and induced seismicity in the Val d'Agri area (Southern Apennines, Italy). Geophys. J. Int. 178, 488–502, doi:10.1111/j.1365246X.2009.04166.x.

Venisti, N., Calcagnile, G., Pontevivo, A., Panza, G. F., 2005. Tomographic study of the Adriatic plate. Pure Appl. Geophys., 162, 311– 329.

Ventura, G., Cinti, F.R., Di Luccio, F., Pino, N.A., 2007. Mantle wedge dynamics versus crustal seismicity 1525–2027. doi:10.1029/2006GC001421.

Waldhauser, F. and Ellsworth, W.L., 2000. A double-difference earthquake location algorithm: Method and application to the northern Hayward fault, Bull. Seism. Soc. Am., 90, 1353-1368.

Waldhauser, F., 2001. hypoDD: A computer program to compute double-difference earthquake locations, USGS Open File Rep., 01-113.

Westaway, R., 1993. Fault rupture geometry for the 1980 Irpinia earthquake: a working hypothesis, Annali di Geofisica 36(1), 51-69.

Wyss M., Liang B., Tanigawa, W.R., and Wu, X., 1992. Comparison of orientations of stress and strain tensors based on fault-plane solutions in Kaoiki, Hawaii, J. Geophys. Res., 97, 4769-4790.